DEVELOPMENT OF SOLUTION-PROCESSED METHODS FOR GRAPHENE SYNTHESIS AND DEVICE FABRICATION

A Dissertation
Presented to
The Academic Faculty

by

Hua-Wei Chu

In Partial Fulfillment
of the Requirements for the Degree
Doctor of Philosophy in the
School of Chemical and Biomolecular Engineering

Georgia Institute of Technology
August 2011

DEVELOPMENT OF SOLUTION-PROCESSED METHODS FOR GRAPHENE SYNTHESIS AND DEVICE FABRICATION

Approved by:

Dr. Clifford L. Henderson, Advisor
School of Chemical & Biomolecular Engineering
Georgia Institute of Technology

Dr. Dennis W. Hess
School of Chemical & Biomolecular Engineering
Georgia Institute of Technology

Dr. Carson Meredith
School of Chemical & Biomolecular Engineering
Georgia Institute of Technology

Dr. Samuel Graham
School of Mechanical Engineering
Georgia Institute of Technology

Dr. Laren M. Tolbert
School of Chemistry & Biochemistry
Georgia Institute of Technology

Date Approved: May 09, 2011

To my family
獻給我摯愛的家人

ACKNOWLEDGEMENTS

I would first like to express my sincerest gratitude to my research advisor, Dr. Cliff Henderson, for taking me as his student. He has extended continuous support, encouragement, and constant guidance throughout my entire graduate research at Georgia Tech. I am very grateful for the freedom he provided me in conducting research. He always offered valuable opinions but never constrained the direction of experiments. I also have to specially thank him for his efforts in fighting for my visa status in the last month of my PhD research. Without him, I might not be able to extend my career in the United States.

I am thankful to Dr. Samuel Graham, Dr. Dennis Hess, Dr. Carson Meredith, and Dr. Laren Tolbert for serving on my committee and provided suggestions during this work. Dr. Tolbert met with me on a weekly basis and provided me with unlimited support. Dr. Hess supported me in modifying the ALD system. Dr. Graham kindly authorized me to use his Raman system. And Dr. Meredith mentored me in learning image analysis. I really appreciate their help.

To whole of Dr. Henderson's group has been a pleasure to work with, and the friendships forged will remain with me for life. I would like to thank all of the past and present members of the group for their support. In particular, many thanks to Jose Baltazar for the OFETs fabrication and measurement, Wei-Ming Yeh and Jing Cheng for performing SEM, Dr. Yueming Hua for transferring the TCNL skill, Dr. Cheng-Tsung Lee for helping with the lithographic patterning, and Dr. David Noga for the help in organic synthesis. I would also like to thank Dr. Richard Lawson, Dr. Jassem Abdallah,

and Annapoorani Sundaramoorthi for their help. I am also thankful to my undergraduate assistants, Junghoon Cha and Daniel williams. In addition, members from Dr. Tolbert's group have also extended enormous support during my research. I would also like to express my thanks to Dr. Janusz Kowalik and Juan Vargas for their help in organic synthesis.

I have made many wonderful friends at Georgia Tech and I will forever treasure these friendships. I want to thank my friends: Yanto Yanto, Pei Yoong Koh, Yanhui Yuan, Chien-Chiang Chen, Dun-Yen Kang, and Jing Yen, for their friendship and help.

Finally, I have been very fortune to have the unconditional love and support of my dearest wife, Hui-Wen Lue. She abandoned her career in Taiwan and came to study in the US with me. She has always stood beside me in difficult times. Moreover, she gave me our cutest princess, NiNi. I don't know how many times per night Hui-Wen has to get up to take care of our baby. She just doesn't want to wake me up in order to let me focus on the thesis. I really appreciate her support. Actually my wife and child are the motivation driving me to finish this work. I am also incredibly thankful to my parents and parents-in-law. They have always had great faith in me and constantly encourage me.

TABLE OF CONTENTS

	Page
ACKNOWLEDGEMENTS	iv
LIST OF FIGURES	ix
SUMMARY	xiii
CHAPTER	
1 INTRODUCTION	1
1.1 Introduction to Graphene	1
1.2 Introduction to Graphene Oxide	4
1.3 Thermochemical Nanolithography (TCNL)	6
1.4 Organization of Thesis	10
1.5 References	12
2 EXFOLIATION OF GRAPHENE SHEETS BY AN ELECTRON DONOR SURFACTANT	17
2.1 Introduction	17
2.2 Background	19
2.3 Results and Discussion	20
2.4 Conclusions	34
2.5 References	35
3 SYNTHETIC APPROACHES TO GRAPHENE BY CHEMICAL TRANSFORMATIONS OF POLYANTHRACENE	39
3.1 Introduction	39
3.2 Polymerization of Anthracene by Chemical Oxidation	43
3.3 Thermal Pyrolysis of Chemically Polymerized Polyanthracene	48
3.4 Polymerization of Anthracene by Electrochemical Oxidation	51

3.5 Thermal Pyrolysis of Electrochemically Polymerized Polyanthracene 57

3.6 References 66

4 HIGHLY REACTIVE 3-AMINOPROPYLTRIETHOXYSILANE MONOLAYER DEPOSITED BY VAPOR SILANIZATION AND SELF-ASSEMBLY OF CONTINUOUS GRAPHENE OXIDE FILM 68

4.1 Introduction 69

4.2 Background 70

4.3 Experimental 73

4.4 Results and Discussion 75

4.5 Conclusions 91

4.6 References 93

5 SOLUTION-PROCESSED GRAPHENE DEVICE FABRICATED BY SELF-ASSEMBLY OF GRAPHENE OXIDE ON VAPOR-DEPOSITED AMINOSILANE 97

5.1 Introduction 98

5.2 Background 98

5.3 Experimental 101

5.4 Results and Discussion 104

5.5 Conclusions 123

5.6 References 124

6 SELECTIVE SELF-ASSEMBLY OF GOLD NANOPARTICLES ON MONOLAYER PATTERNS ACTIVATED BY THERMOCHEMICAL NANOLITHOGRAPHY 128

6.1 Introduction 128

6.2 Experimental 130

6.3 Results and Discussion 131

6.4 Conclusions 140

6.5 References 141

7 CONCLUSIONS AND RECOMMENDATIONS 144

7.1 Conclusions 144

7.2 Recommendations for Future Works 146

LIST OF FIGURES

Page

Figure 1-1: Formation of 0D, 1D, and 3D carbon materials from graphene 1

Figure 1-2: the band structure (top) and brillouin zone (bottom) of graphene 2

Figure 1-3: Intramolecular oxidative cyclodehydrogenation of soluble branched polyphenylenes 3

Figure 1-4: Chemical structure of GO 5

Figure 1-5: The process of making chemical modified graphene (CMG) 5

Figure 2-1: Films of ChDTT on HOPG 18

Figure 2-2: The synthesis route of Dicholesteryl-dithienothiophene (ChDTT) 21

Figure 2-3: Absorption spectra of: A) ChDTT in 1,2-DCE, 0.01 mM solution; B) After addition of 2mg expandable carbon to the mother solution; C) After addition of 20 mg expandable carbon. 23

Figure 2-4: Absorption spectra of: A) PmPV in 1,2-DCE, 0.027 mM solution; B) After addition of 2 mg expandable carbon to the mother solution; C) After addition of 20 mg expandable carbon 23

Figure 2-5: (a), (b) TEM image of one edge of as-synthesized ultra-large graphene sheet with size > 20μm. (c), (d) Selective-area electron diffraction (SAED) patterns in (a) 25

Figure 2-6: TEM images of some representative graphene sheets. SAED with larger aperture shows that they are uniform few-layer grapheme. 26

Figure 2-7: (a). Raman spectra for HOPG and ChDTT exfoliated graphene flakes; (b). The deconvolution of 2D band of Raman spectra in (a). 29

Figure 2-8: PmPV and ChDTT under various removal procedures. (a) TGA results. (b)-(f) AFM analyses 32

Figure 2-9: XPS high-resolution C_{1S} peak for expanded graphite 34

Figure 3-1: Oligomerization of pentacene 40

Figure 3-2: Chemical structure of PTCDA 41

Figure 3-3: Schematic illustration of this project 42

Figure 3-4: Polymerization of anthracene by chemical oxidation 43

Figure 3-5: MALDI Spectrum of Polyanthracene 44

Figure 3-6: ^{1}H NMR spectra of: A, Anthracene; B, 9,9'-Bianthracene; C, Polyanthracene. 45

Figure 3-7: UV-Vis absorption and fluorescence spectra for Anthracene; 9,9'-Bianthracene; Polyanthracene. 46

Figure 3-8: Raman spectra for Anthracene; 9,9'-Bianthracene; Polyanthracene. 47

Figure 3-9: Raman spectra of as synthesized polyanthracene and polyanthracene after 1000° C thermal treatment in forming gas. 49

Figure 3-10: Optical microscopic images and Raman spectra on the same iron chloride doped sample after 1000° C thermal treatment. 51

Figure 3-11: Polymerization of anthracene by electrochemical oxidation 52

Figure 3-12: (A) Cyclic Voltammetry of anthracene when ITO electrode is used for the electrooxidation. (B) Absorption spectrum of polyanthracene polymerized on ITO. 54

Figure 3-13: Cyclic Voltammetry of anthracene when gold electrode is used for the electrooxidation. 55

Figure 3-14: (A) Optical microscopic image of electrochemically polymerized polyanthracene. (B) Raman spectrum of electrochemically polymerized polyanthracene. 56

Figure 3-15: AFM images of electrochemically polymerized polyanthracene 57

Figure 3-16: (A) Optical microscopic image of electrochemically polymerized polyanthracene after $FeCl_3$ doping and 1000°C thermal treatment. (B) Raman spectrum of electrochemically polymerized polyanthracene after $FeCl_3$ doping and 1000°C thermal treatment. 59

Figure 3-17: AFM images of electrochemically polymerized polyanthracene after iron chloride doping and 1000°C pyrolysis. 60

Figure 3-18: The comparison of pyrolysis results of (A) chemically synthesized polyanthracene and (B) electro polymerized polyanthracene. 60

Figure 3-19: (A) A survey XPS scan for polyanthracene thin film made by electropolymerization. (B) A survey XPS scan for electropolymerized polyanthracene after iron chloride doping and 1000°C thermal treatment. 62

Figure 3-20: High resolution scan in carbon C1's region of electropolymerized polyanthracene after iron chloride doping and 1000°C thermal treatment. 63

Figure 3-21: Raman spectra of iron chloride doped electropolymerized polyanthracene thin film after pyrolyzing at different temperature. 65

Figure 4-1: High resolution XPS spectra of N_{1s} region for APTES silanized silicon surface 77

Figure 4-2: (a) Deconvoluted free amine ($-NH_2$) ratio in high resolution XPS spectra of N_{1s} region of vapor-silanized substrates; (b) Nitrogen/silicon atomic ratio determined by XPS full range scan for each data point in (a). 79

Figure 4-3: High resolution XPS spectra of N_{1s} region for APTES silanized silicon surface deposited by vapor-silanization 81

Figure 4-4: SEM images of samples in figure 4-3 after immersing in 0.05mg/ml GO solution for 40 hours. 82

Figure 4-5: (a) Free amine ratio of 0.027g/min APTES vapor-silanized surface versus reaction temperature; (b) nitrogen/silicon atomic ratio of 0.027g/min APTES vapor-silanized surface versus reaction temperature 84

Figure 4-6: High resolution XPS spectra of N_{1s} region for APTES silanized silicon surface deposited by vapor-silanization 86

Figure 4-8: (a) Surface coverage rate of GO flakes on APTES silanized silicon surface deposited by vapor-silanization 89

Figure 4-9: (a) SEM image of APTES vapor-silanized surface; (b) AFM topography image of APTES vapor-silanized surface; (c) and (d) SEM images of edges of continuous GO film 91

Figure 5-1: Schematic illustration of the lift-off process for fabricating both few-layer rGO active layer and thick rGO electrodes by the aid of vapor-silanization of APTES. 105

Figure 5-2: High resolution XPS spectra of N_{1s} region for an APTES-silanized silicon surface under different silanization conditions 107

Figure 5-3: (a) Surface coverage rate of GO flakes self-assembled on an APTES vapor-silanized surface; (b) Thickness of GO film self-assembled on an APTES vapor-silanized surface. 109

Figure 5-4: High resolution XPS spectra of (a) C_{1s} and (b) N_{1s} region for the 24-hr self-assembled GO films thermally reduced at a different temperature in forming gas. 111

Figure 5-5: AFM topography image of a 24-hr self-assembled GO film: (a) as deposited, (b) after 1000°C reduction in forming gas. 112

Figure 5-6: (a) Optical microscope image of a corner of the 24-hr self-assembled GO pattern; (b) SEM image of a GO - SiO_2 border in (a). (c) SEM overview of the 30-min self-assembled GO film on pre-patterned gold electrodes and channel; (d) Zoom-in of the channel-gold electrode border in (c) 114

Figure 5-7: (a) Transfer characteristics of the 24-hr self-assembled GO OFET with bottom gate, bottom contact; (b) Transfer characteristics of the 30-min self-assembled GO OFET with bottom gate, bottom contact 117

Figure 5-8: Relationship between film thickness and GO concentration in solution for spin-coated, bare SiO_2, or APTES-treated SiO_2 samples 119

Figure 5-9: AFM topography image of spin-coated 45nm GO film: (a) as deposited, (b) after 1000°C reduction in forming gas 120

Figure 5-10: (a) SEM overview of patterned GO electrode; (b) Optical microscope image of the border between GO electrode and channel; (c) AFM topography image of the border between GO electrode and channel; (d) AFM cross section of line 1 in (c) 121

Figure 5-11: (a)Transfer characteristics of a P3HT OFET using evaporated 50nm gold S/D electrodes. (b) Transfer characteristics of a P3HT OFET employing 35nm thick rGO S/D electrodes. 122

Figure 6-1: (a) Synthesis of THP-MPTES SAM. (b) Surface modification of silicon substrate. (c) Local thermal decomposition of THP protecting group. (d) Selective self-assembly of 10nm AuNPs 131

Figure 6-2: (a) Thermal mass spectrum of hydrolyzed THP-MPTES; (b) Static water contact angle of THP-MPTES modified silicon oxide substrate after hot plate baking. 134

Figure 6-3: Topography and friction images of THP-MPTES SAM modified silicon substrate after TCNL. 137

Figure 6-4: A variety of AuNPs patterns generated by thermal writing. 139

Figure 7-1: Electron injection mass spec (EI MS) of bianthracene. 147

SUMMARY

Various solution-processed methods have been employed in this work. For the synthesis of graphene, a chemical exfoliation method has been used to generate large graphene flakes in the solution phase. In addition, chemical or electro polymerization has been used for synthesizing polyanthracene, which tends to form graphene nanoribbon through cyclodehydrogenation. For the device fabrication, graphene oxide (GO) thin films were deposited from solution phase on the vapor-silanzed aminosilane surface to make semiconducting active layer or conducting electrodes. Gold nanoparticles (AuNPs) were selectively self-assembled from solution phase to pattern nanowires.

A novel macromolecular surfactant dicholesteryldithienothiophene (ChDTT) was synthesized by Dr. Janusz Kowalik in Dr. Tolbert's group. By simple sonication of expandable graphite in solutions containing ChDTT, graphene sheets with sizes exceeding 50 micrometers were observed. The new surfactant is more efficient than poly(m-phenylenevinylene-co-2,5-dioctyloxy-p-phenylenevinylene) (PmPV), and can be cleanly removed by thermal treatment. Using this surfactant, graphene flakes can be extracted directly from highly oriented pyrolytic graphite (HOPG) without additional chemical, mechanical, or thermal treatment, producing larger flakes of higher quality.

In the work of making reduced-GO (rGO) devices, we present a process to pattern and deposit both GO thin film or few-layer GO by a combination of conventional lithography, vapor silanization, GO self-assembly (or spin-coating), and lift-off. We explored an effective method to deposit 3-aminopropyltriethoxysilane (APTES) through a vapor phase and were able to generate a surface with a higher ratio of free amine. The

transfer characteristics of GO film self-assembled on vapor-silanized APTES proved that we can precisely deposit continuous few-layer GO with 1~3 layers. Besides, the under-layer amine corrected the intrinsic p-doping effect of rGO in air. On the other hand, we also showed that the vapor-silanized APTES layer can form strong electrostatic attraction and further increase film thickness to reach higher conductivity. Devices bearing rGO source-drain showed superior performance than gold electrodes.

A flow type vacuum reactor equipped with an evaporator and carrier gas flow system was used to perform the vapor-silanization of 3-Aminopropyltriethoxysilane (APTES). We altered the APTES vapor concentration, reaction time, and reaction temperature to seek the high quality APTES monolayer. It was found that vapor-silanization performed under 150°C can generate an APTES layer with high free amine content and that is uniform in morphology. A continuous GO thin film can be deposited on an APTES layer in 10 minutes by the self-assembly of the GO flakes. Similarly, highly dense AuNPs arrays can also be immobilized on the surface.

Thermochemical nanolithography, which in this case involves use of a heated nanoprobe to pattern a protected reactive self-assembled monolayer (SAM), is used to perform controlled patterning and assembly of gold nanoparticles (AuNPs). When the cantilever heater was operated at an appropriate condition, the SAM was ablated to produce positive tone AuNP features. We show AuNP features ranging from large densely covered squares to single particle wide lines and features. This method can be performed on a wide variety of substrates by simply choosing an appropriate surface reactive group for the SAM layer.

CHAPTER 1

INTRODUCTION

1.1 Introduction to Graphene

Graphene is a flat monolayer of carbon aromatic structures tightly packed into a two-dimensional honeycomb lattice, and it is a single sheet of building unit for all other dimensionalities of graphite structures. It can be wrapped up into 0D fullerenes (C60, C70), rolled into 1D carbon nanotubes, or stacked into 3D graphite. Graphene sheets are one-atom thick, have 2D layers of sp2-bonded carbon, and are predicted to have unusual properties.[1] Figure 1-1 shows the structure of graphene and other graphite structures.

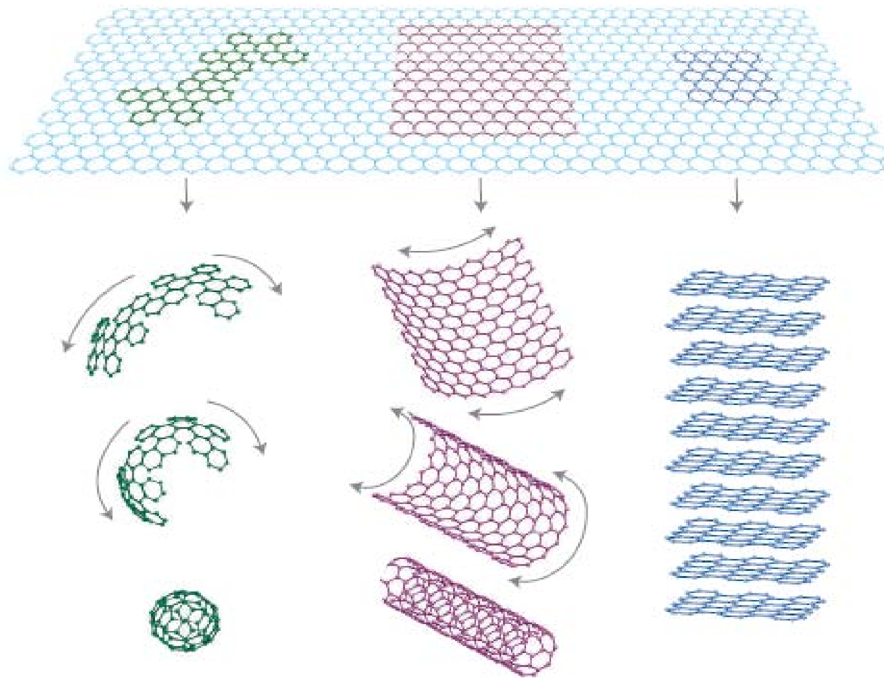

Figure 1-1: Formation of 0D, 1D, and 3D carbon materials from graphene[1]

Figure 1-2 shows the peculiar single-particle band structure of this 2D material.[2] Graphene has two atoms per unit cell, which results in two 'conical' points per Brillouin

zone where band crossing occurs. Near these crossing points, the electron energy is linearly dependent on the wave function. This is quite different from those observed in conventional three-dimensional materials, which have parabolic dispersion relationships. The linear dispersion causes the electrons and holes in graphene to mimic relativistic particles, which have zero effective mass and a velocity that is about 300 times slower than that of light. Because of the symmetry of the band structure, it will also follow the long-range hopping processes, meaning the absence of localization.[3]

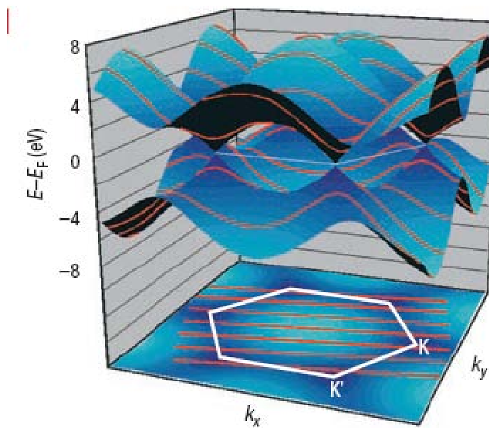

Figure 1-2: the band structure (top) and brillouin zone (bottom) of graphene[2]

In 2004, Andre Geim and Kostya Novoselov's research group, at Manchester University, UK, used a technique called micromechanical cleavage to extract a single sheet (a monolayer of atoms) from three-dimensional graphite.[4] This method is usually called exfoliation. Deposited exfoliated graphene proved to be an extremely important new 2-D electronic material. Another method for graphene formation is epitaxy, which grows graphene from SiC substrates. The application of epitaxial graphene in electronic devices originated at Georgia Tech in 2004, created by a group lead by Walter deHeer.[5] Intensive research revealed that both epitaxial graphene and exfoliated graphene have the same band structure near the Fermi level. The electron properties of these two materials are similar. Another important progress for making graphene is Klaus Mullen's work.

The concept which the Mullen group held was based on the synthesis of polyphenylenes with three dimensional structures. These serve as precursors for cyclodehydrogenation toward flat graphenes[6] (Figure 1-3).

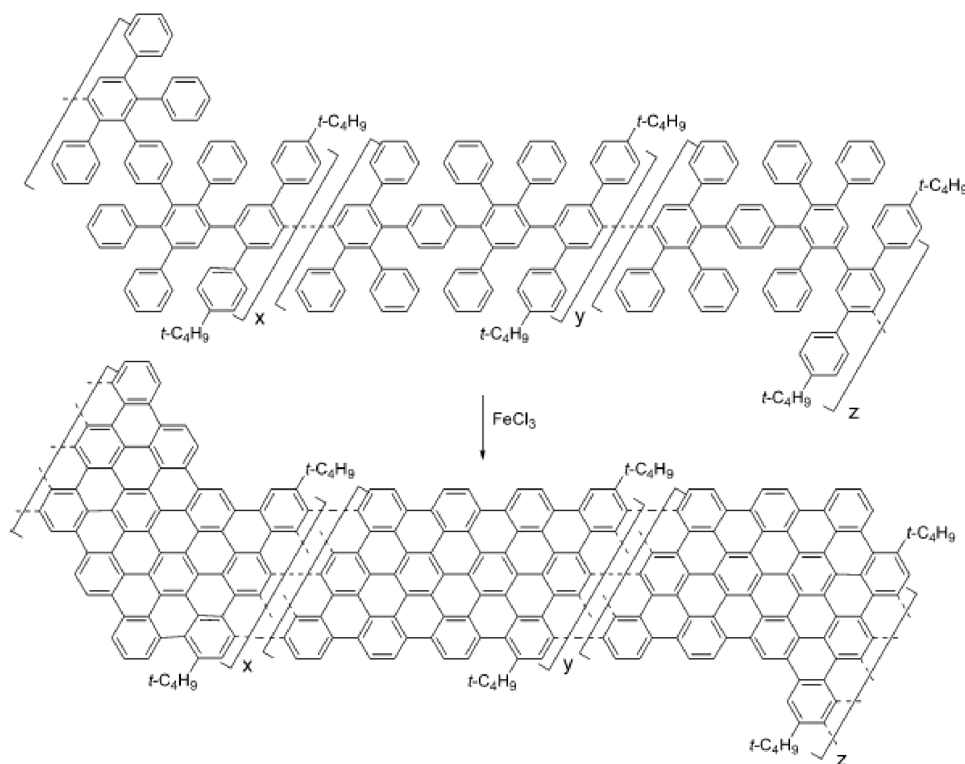

Figure 1-3: Intramolecular oxidative cyclodehydrogenation of soluble branched polyphenylenes[6]

Besides exfoliated and epitaxial methods, graphene oxide (GO) reduction and CVD (chemical vapor deposition) graphene are the other two major methods to make graphene. The advantage of these methods lies in the potential for mass production. Just like in the growth of carbon nanotube, chemical vapor deposition (CVD), because of its potential for mass production was also applied to synthesize graphene.[7] The growth of the graphene monolayer from transition metal catalysts such as Ni, Co, Pt, Ir, and Ru has been intensively studied. Hydrocarbon gas, such as methane, was passed through the

catalyst surface under high temperature and low pressure causing the nucleation and growth of graphene. A solid precursor, such as camphor, has also been used in CVD synthesis of graphene.[8] Because of the six-member ring or five-member ring structure of camphor after decomposition, it has been proposed that graphene is formed according to its surface rearrangement. Recently, three different groups from around the world have reported a similar method involving ambient pressure CVD growth graphene on Ni surface and using polymer or wet etch to transfer graphene film from Ni to silicon oxide substrate.[7, 9, 10] This is a promising result for the industrial application of graphene, but the electron mobility by this method is about two orders lower than exfoliated graphene flakes and the film usually contains uneven layers of graphene. Here, we propose an alternative pathway to synthesize graphene. If the precursors are already in the form of a basic graphene structure and the numbers of C-C bond needed to stitch has been eliminated to a minimum, the energy barrier to form a graphene structure should be much lower.

1.2 Introduction to Graphene Oxide

The idea of making graphene oxide (GO) was inspired by the preparation of graphite oxide, which was first discovered in the nineteenth century. In 1958, Hummers issued an effective method to oxidize graphite using strong acid.[11] The Hummers method became a major pathway to prepare graphite oxide, and, now, graphene oxide. In this method, by oxidation, the single layer graphene sheet in graphite was strongly disrupted and bonded to oxygen by means of hydroxyl groups, epoxide groups, and carbonyl groups.[12] The surface becomes strongly hydrophilic and provides suitable conditions for producing aqueous colloids suspensions. For pristine graphene prepared from mechanical exfoliation or thermal expansion, it is extremely difficult to disperse flakes in any kind of

solvent, so the low yield is still a problem. The solubility and accessibility of GO makes it a more and more popular research topic. Figure 1-4 shows the chemical structure of GO.

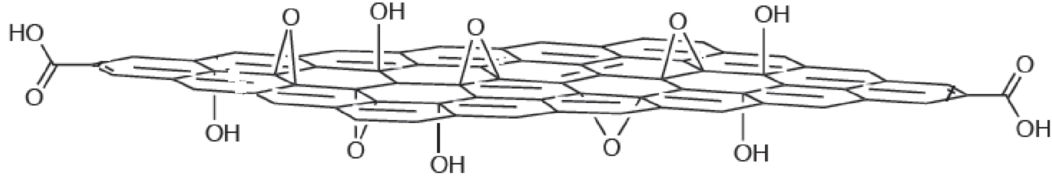

Figure 1-4: Chemical structure of GO[13]

Chemical Modified Graphene (CMG) can be produced by reducing graphene oxide's aqueous suspension.[14] This process includes: (1) synthesizing graphite oxide by the oxidation of graphite, (2) exfoliating the graphene oxide sheet by sonication or intensive stir, and (3) reducing the graphene oxide sheet back to graphene. The resulting graphene sheet is conductive and is stabilized by the surface's negative charge. Figure 1-5 illustrates this process. Usually, the Hummers method is modified to synthesize graphene oxide. A general method, summarized in literature, is reported here to address the starting work of the GO project.[15] First, a small amount of natural graphite is vigorously stirred in a concentrated sulfuric acid solution with $KMnO_4$. It is then washed with 5wt% sulfuric acid and reacted with 30wt% hydrogen peroxide to complete the oxidation. Then, cycles of wash, including centrifugation and resuspending by sonication, is performed. After filtration, brown GO powder can be obtained. Thin films of GO can be deposited by drop-casting or spin coating.

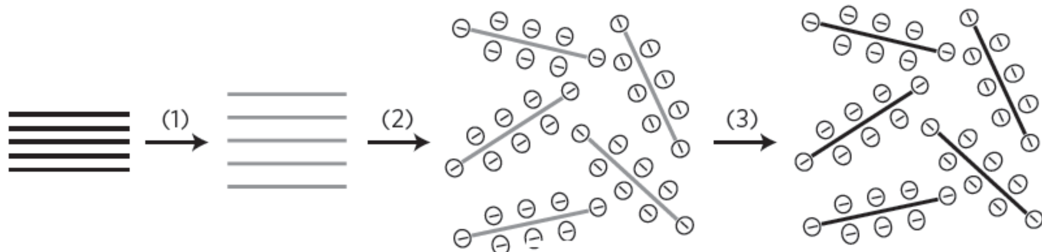

Figure 1-5: The process of making chemical modified graphene (CMG)[14]

Graphene oxide is electrically insulating because of the disruption of the SP2 graphene structure by hydroxyl or epoxide side groups. This problem can be solved by reducing the GO, and it has been intensively studied recently. The reduction method includes chemical reduction using strong reductants such as hydrazine and $NaBH_4$, thermal reduction, and UV photo reaction. In addition, it has been proven that high-temperature treatment can gradually remove the oxygenated functional groups of GO. Through pyrolysis, GO can be reduced to a more thermal-stable form of graphene. Yang and Ruoff et al. used XPS and micro Raman to detect GO's carbon structure after thermal treatment.[12] Carbonyl and hydroxy groups were almost eliminated after 500ºC annealing in flowing argon and hydrogen. Becerril and Chen et al. reported that 30% of the mass was lost with the onset of around 200 ºC in TGA due to the desorption of CO, CO2, and other oxygenated carbon species.[15] It has also been reported that thermal reduction has results that are compatible those of chemical reduction, and the electrical conductivity of GO becomes tunable by low temperature thermal treatment (125-240 ºC).[16]

1.3 Thermochemical Nanolithography (TCNL)

Thermochemical Nanolithography (TCNL) is a recently developed technique that allows for the patterning of material surfaces with nanometer scale precision using a heated cantilever probe (i.e. similar to conventional AFM probes except that they can be heated to temperatures up to 1000 ºC). Thus far, using such a heated nanoprobe it has been shown that: a variety of processes are possible including: (1) sculpting of polymer films and surfaces in three dimensions, (2) selective modification of the surface chemistry of polymer films and SAMs, and (3) that such sculpted and surface modified patterns can be used to guide the further growth (e.g. by ALD) or deposition (e.g. adsorption of proteins from solution) of materials onto these patterns. Prof. William P.

King from the University of Illinois at Urbana-Champaign provides the thermal cantilevers used in this work. The cantilevers are made of doped single crystal silicon and much information about their fabrication, characterization, and application has been reported.[17-22] The temperature of a thermal cantilever can reach 1000ºC[23], and an integrated electrical resistance heater-thermometer makes the temperature-control possible.

Before introducing the development of TCNL, a review of scanning probe lithography is necessary. The scanning probe lithography, which works by using a special atomic force microscope (AFM) cantilever for high resolution patterning, has been developed. It is well known that an AFM holds the capability of reaching atomic level imaging and certainly shows the potential to reach nanoscale resolution. Different approaches related to scanning probe lithography will be discussed later, but no methodology among them shows three dimensional structures with high throughputs. Speed is still the biggest problem for this kind of technique. However, large arrays of heated AFM cantilever probes were developed for data storage applications[24, 25], which provide a basic concept to envision the breakthrough of high speed and high resolution 3-D lithography. Materials and processes were developed to match the capability of local thermally induced physiochemical changes. Theoretically, these can push resolutions approaching the radius of curvature of the AFM tip, which is currently in the range of 5 to 50 nm. Using these kinds of thermal scanning probe techniques to generate nanopatterns should ideally have the following properties: (1) nanometer resolution, (2) fast writing speeds (ideally mm to cm/s), (3) nondestructive, (4) suitable for a wide range of materials, (5) ability to function in different mediums (air, water, vacuum). In order to better understand the contribution and context of this work, a further discussion of alternative probe-based lithography methods is required.

First of all, the mechanical scratching is illustrated because it holds the most basic concept of scanning probe lithography—that is, scratching a surface to obtain a pattern.

By applying a sufficient force on the tip, the thin film surface can be indented or scratched as it scans. AFM tips have been successfully used to scratch a variety of both soft and hard surfaces[26, 27]**.** As can be imagined, the main problem with this method is the resolution and the damage of the tip. Coating the tip with hard materials (e.g. diamond) has successfully increased the lifetime of probe tips, but the scratching method has not received any serious attention as a true manufacturing technique[28]. Second, the field-emission probe is also illustrated due to its wide application. Majumdar and coworkers used a gold-coated AFM tip to perform local electron exposure of a thin PMMA film coated in metallic substrate by applying a bias voltage between the tip and the substrate. The gold-coated AFM tip became an electron source and resulted in chain cleavage of the PMMA. It is similar to the E-beam lithography in some ways. A 35 nm line width could be reached by this method. A variety of other materials have also been successfully patterned using the field emission current from an AFM tip[29, 30]. Frechet and coworkers have also modulated the functional group of the Self Assembly Monolayer (SAM)[31]. However, some disadvantages, such as the restriction in insulating substrates and the need for electron beam sensitivity in the imaging material, have somewhat limited its applications. Sugimura and coworkers used conductive AFM tips to locally electrochemically degrade an organosilane monolayer[32]. A spatial resolution of 20 nm was obtained while scanning speeds as high as 5000 μm/sec were achieved. Dai and coworkers applied single-walled carbon nanotube (SWNT) tipped cantilevers to locally oxidize a Ti metal film[33]. Ultra-narrow oxidized titania lines with 5 nm widths could be formed by using this method.

More recently, Dip Pen Nanolithography (DPN) attracted a lot of attention[34]. In the same manner as a quill pen, the AFM tip was coated with a thin film of a molecular "ink" which is transferred to the substrate surface when the tip is engaged. Monolayer patterns with nano scale can be written onto the substrate surface using this directly additive process. Various materials, including inorganics, organics, biomolecules, and

polymers have been deposited onto a variety of substrates using this method[35, 36]. Feature sizes as small as 10 to 15 nm have been demonstrated[37]. DPN methods have a variety of limitations including: (1) Slow speed due to repeating engagement of tip while writing, (2) only extremely thin layers can be written, and (3) the tip must be reinked. These limitations imply that the throughput is also the major concern of the DPN.

Unlike other scanning probe lithography methods, thermochemical nanolithography (TCNL) modifies samples chemically and mechanically and fits for broader applications. The technique has potential applications in a wide variety of material such as data storage, polymer patterning, atomic layer deposition (ALD), and many more. Mamin and Rugar in IBM Almaden research center are the first group to use heated AFM cantilevers, and they made nanoindentations in a PMMA substrate with it[38]. The cantilever was heated by a pulsed infrared laser to soften PMMA in the vicinity of the hot tip, and polymer was indented while sufficient force was applied. A few tens of nanometer pits were made on the PMMA substrate with their method. However, the method of using the laser to heat the cantilever requires an external laser source, and the spot has to be precisely aligned to the probe tip. Another laser spot is focused on the cantilever, which also needs precise alignment, dedicated for the AFM reflection signal. Two lasers aligned on the same object makes this process very difficult. To solve this problem, a resistive heating element was integrated in the tip and a piezoresistive cantilever was invented[39]. Additionally, the flash heating cantilever was also designed. The heating time could reach less than 1 μs, and the cooling time could be less than 10 μs[21]. IBM's "Millipede" project has applied this technology for data storage and demonstrated the parallel operation of 32x32 arrays of heated cantilevers. Their initial nanomechanical experiments done at the IBM Almaden Research Center also showed that individual tips could support data rates as high as 1 to 2 megabits per second and data storage densities between 400 and 500 Gbit/in^2. For the heat efficiency, it has been reported that most of the temperature increase occurs directly in the substrate-tip contact

area, with only less than 5% of the overall temperature increase occurring in the substrate away from the contact area[40]. Additionally, the hot spot focused by a heated tip can be as small as 2 nm in diameter, and the temperature of the substrate can be heated to over 500 ºC by using doped silicon cantilevers. TCNL has several advantages to other scanning probe lithography methods. The writing speed of the TCNL is limited by heat transfer while DPN is limited by mass transfer. TCNL heat transfer is generally much faster, and higher writing speeds can be achieved, both of which make it more suitable for commercialization. TCNL also has the capability to produce multifunctional patterns using a single tip, while DNP has to switch tips and ink. It also has been demonstrated that TCNL has better resolution (sub15 nm) than field-emission patterning (~45 nm).

1.4 Organization of Thesis

As depicted in the title of this thesis, the work can be divided into two major categories, that is, the graphene synthesis and the device fabrication. Here, we attempted to develop solution-processable methods to simplify the novel techniques in both categories in order to broaden the application fields in either academic research or industry. There are also two topics in each of the categories. For graphene synthesis, the solution-processed mechanical exfoliation (or chemical exfoliation) and the direct chemical synthesis have been studied. For device fabrication, graphene oxide and gold nanoparticles (AuNPs) have both been self-assembled from the solution phase on the aminosilane modified surface to build up either the semiconductor active layer or the conducting electrodes.

Due to the speciality of each project, a profound introduction and background for each topic will be stated separately in each chapter. Chapter one is an overall introduction for the development of graphene, graphene oxide, and TCNL. Graphene is a novel and hot topic in the field of materials research. In order to develop the basic knowledge, e.g.

standard Raman spectrum, XPS spectrum, AFM images, etc., in the group, an efficient method which is suitable for the laboratories to make graphene flakes was developed and illustrated in chapter two. From the fundamental studies in pristine graphene flakes, we gained a lot of basic knowledge in graphene research. In the mean time, a novel method which can exfoliate micron meter level single-layer graphene flakes was issued.

In chapter three, we discuss our attempt to directly synthesize graphene nanoribbons from the solution phase either chemically or electrochemically. Although this work is still in progress, the preliminary results support our theory that a pre-defined polyanthracene structure has a lower energy barrier toward the graphite (or graphene) structure. According to this, the details of polyanthracene synthesis, electro polymerization, oxidant doping, and pyrolysis are reported along with the promising graphitization results for the convenience for future study.

Chapter four and five report a successful case in the development of the graphene device through graphene oxide reduction. Chapter four explains a novel vapor-silanization method for the deposition of high quality aminosilane. By this means, patterned substrates bearing photoresist are able to enter the silanization chamber without damaging the pattern. Moreover, the result shows that a vapor-silanized aminosilane surface has higher reactivity than one silanized in the conventional liquid phase. Therefore, a continuous GO ultra-thin film can be deposited and patterned. Base on these promising results, GO devices were fabricated in forms of ultra-thin (three atomic layers) semiconducting active layers and thick conducting electrodes and is reported in chapter five. With the aid of the vapor-silanized aminosilane monolayer, discussed in chapter three, GO flakes are able to either be self-assembled or spin-coated on the oxide dielectric layer to form ultra-thin continuous GO layers or ultra-thick film, respectively. The transfer characteristics of our graphene field-effect transistors (FETs) are also presented in chapter five.

Chapter six involves using a novel technique, TCNL, to pattern and self-assemble AuNPs from the solution phase. The selective self-assembled AuNPs have been applied for conducting nanowires in the electronic devices. The introduction and technological background for TCNL is addressed in chapter one, while the details for the thermal deprotection of the end-capped silane monolayer will be introduced in chapter six.

1.5 References

1. Geim, A. K.; Novoselov, K. S., The rise of graphene. *Nature Materials* **2007,** *6* (3), 183-191.

2. Avouris, P.; Chen, Z. H.; Perebeinos, V., Carbon-based electronics. *Nature Nanotechnology* **2007,** *2* (10), 605-615.

3. Katsnelson, M. I., Graphene: carbon in two dimensions. *Materials Today* **2006,** *10* (1-2), 20-27.

4. Novoselov, K. S.; Geim, A. K.; Morozov, S. V.; Jiang, D.; Zhang, Y.; Dubonos, S. V.; Grigorieva, I. V.; Firsov, A. A., Electric field effect in atomically thin carbon films. *Science* **2004,** *306* (5296), 666-669.

5. Berger, C.; Song, Z. M.; Li, T. B.; Li, X. B.; Ogbazghi, A. Y.; Feng, R.; Dai, Z. T.; Marchenkov, A. N.; Conrad, E. H.; First, P. N.; de Heer, W. A., Ultrathin epitaxial graphite: 2D electron gas properties and a route toward graphene-based nanoelectronics. *Journal of Physical Chemistry B* **2004,** *108* (52), 19912-19916.

6. Wu, J. S.; Pisula, W.; Mullen, K., Graphenes as potential material for electronics. *Chem Rev* **2007,** *107* (3), 718-747.

7. Reina, A.; Jia, X. T.; Ho, J.; Nezich, D.; Son, H. B.; Bulovic, V.; Dresselhaus, M. S.; Kong, J., Large Area, Few-Layer Graphene Films on Arbitrary Substrates by Chemical Vapor Deposition. *Nano Lett* **2009,** *9* (1), 30-35.

8. Somani, P. R.; Somani, S. P.; Umeno, M., Planer nano-graphenes from camphor by CVD. *Chemical Physics Letters* **2006,** *430* (1-3), 56-59.

9. Kim, K. S.; Zhao, Y.; Jang, H.; Lee, S. Y.; Kim, J. M.; Kim, K. S.; Ahn, J. H.; Kim, P.; Choi, J. Y.; Hong, B. H., Large-scale pattern growth of graphene films for stretchable transparent electrodes. *Nature* **2009,** *457* (7230), 706-710.

10. Yu, Q. K.; Lian, J.; Siriponglert, S.; Li, H.; Chen, Y. P.; Pei, S. S., Graphene segregated on Ni surfaces and transferred to insulators. *Applied Physics Letters* **2008,** *93* (11), -.

11. Hummers, W. S.; Offeman, R. E., Preparation of Graphitic Oxide. *J Am Chem Soc* **1958,** *80* (6), 1339-1339.

12. Yang, D.; Velamakanni, A.; Bozoklu, G.; Park, S.; Stoller, M.; Piner, R. D.; Stankovich, S.; Jung, I.; Field, D. A.; Ventrice, C. A.; Ruoff, R. S., Chemical analysis of graphene oxide films after heat and chemical treatments by X-ray photoelectron and Micro-Raman spectroscopy. *Carbon* **2009,** *47* (1), 145-152.

13. Park, S.; Ruoff, R. S., Chemical methods for the production of graphenes. *Nature Nanotechnology* **2009,** *4* (4), 217-224.

14. Li, D.; Muller, M. B.; Gilje, S.; Kaner, R. B.; Wallace, G. G., Processable aqueous dispersions of graphene nanosheets. *Nature Nanotechnology* **2008,** *3* (2), 101-105.

15. Becerril, H. A.; Mao, J.; Liu, Z.; Stoltenberg, R. M.; Bao, Z.; Chen, Y., Evaluation of solution-processed reduced graphene oxide films as transparent conductors. *Acs Nano* **2008,** *2* (3), 463-470.

16. Jung, I.; Dikin, D. A.; Piner, R. D.; Ruoff, R. S., Tunable Electrical Conductivity of Individual Graphene Oxide Sheets Reduced at "Low" Temperatures. *Nano Lett* **2008,** *8* (12), 4283-4287.

17. Vettiger, P.; Cross, G.; Despont, M.; Drechsler, U.; Durig, U.; Gotsmann, B.; Haberle, W.; Lantz, M. A.; Rothuizen, H. E.; Stutz, R.; Binnig, G. K., The "millipede" - Nanotechnology entering data storage. *Ieee T Nanotechnol* **2002,** *1* (1), 39-55.

18. Nelson, B. A.; King, W. P.; Laracuente, A. R.; Sheehan, P. E.; Whitman, L. J., Direct deposition of continuous metal nanostructures by thermal dip-pen nanolithography. *Applied Physics Letters* **2006,** *88* (3), -.

19. King, W. P.; Saxena, S.; Nelson, B. A.; Weeks, B. L.; Pitchimani, R., Nanoscale thermal analysis of an energetic material. *Nano Lett* **2006,** *6* (9), 2145-2149.

20. Binnig, G.; Despont, M.; Drechsler, U.; Haberle, W.; Lutwyche, M.; Vettiger, P.; Mamin, H. J.; Chui, B. W.; Kenny, T. W., Ultrahigh-density atomic force microscopy data storage with erase capability. *Applied Physics Letters* **1999,** *74* (9), 1329-1331.

21. Chui, B. W.; Stowe, T. D.; Ju, Y. S.; Goodson, K. E.; Kenny, T. W.; Mamin, H. J.; Terris, B. D.; Ried, R. P.; Rugar, D., Low-stiffness silicon cantilevers with integrated heaters and piezoresistive sensors for high-density AFM thermomechanical data storage. *J Microelectromech S* **1998,** *7* (1), 69-78.

22. King, W. P.; Kenny, T. W.; Goodson, K. E.; Cross, G.; Despont, M.; Durig, U.; Rothuizen, H.; Binnig, G. K.; Vettiger, P., Atomic force microscope cantilevers for combined thermomechanical data writing and reading. *Applied Physics Letters* **2001,** *78* (9), 1300-1302.

23. Sunden, E. O.; Wright, T. L.; Lee, J.; King, W. P.; Graham, S., Room-temperature chemical vapor deposition and mass detection on a heated atomic force microscope cantilever. *Applied Physics Letters* **2006,** *88* (3), -.

24. Markiewicz, P.; Goh, M. C., Atomic-Force Microscope Tip Deconvolution Using Calibration Arrays. *Review of Scientific Instruments* **1995,** *66* (5), 3186-3190.

25. Vettiger, P.; Despont, M.; Drechsler, U.; Durig, U.; Haberle, W.; Lutwyche, M. I.; Rothuizen, H. E.; Stutz, R.; Widmer, R.; Binnig, G. K., The "Millipede" - More than one thousand tips for future AFM data storage. *Ibm J Res Dev* **2000,** *44* (3), 323-340.

26. Magno, R.; Bennett, B. R., Nanostructure patterns written in III-V semiconductors by an atomic force microscope. *Applied Physics Letters* **1997,** *70* (14), 1855-1857.

27. Sugihara, H.; Takahara, A.; Kajiyama, T., Mechanical nanofabrication of lignoceric acid monolayer with atomic force microscopy. *Journal of Vacuum Science & Technology B* **2001,** *19* (2), 593-595.

28. Fonseca, H. D.; Mauricio, M. H. P.; Ponciano, C. R.; Prioli, R., Metal layer mask patterning by force microscopy lithography. *Materials Science and Engineering B-Solid State Materials for Advanced Technology* **2004,** *112* (2-3), 194-199.

29. Wilder, K.; Quate, C. F.; Adderton, D.; Bernstein, R.; Elings, V., Noncontact nanolithography using the atomic force microscope. *Applied Physics Letters* **1998,** *73* (17), 2527-2529.

30. Davidsson, P.; Lindell, A.; Makela, T.; Paalanen, M.; Pekola, J., Nano-lithography by electron exposure using an Atomic Force Microscope. *Microelectron Eng* **1999,** *45* (1), 1-8.

31. Fresco, Z. M.; Suez, I.; Backer, S. A.; Frechet, J. M. J., AFM-induced amine deprotection: Triggering localized bond cleavage by application of tip/substrate voltage bias for the surface self-assembly of nanosized dendritic objects. *J Am Chem Soc* **2004,** *126* (27), 8374-8375.

32. Sugimura, H.; Nakagiri, N., AFM lithography in constant current mode. *Nanotechnology* **1997,** *8*, A15-A18.

33. Gotoh, Y.; Matsumoto, K.; Maeda, T.; Cooper, E. B.; Manalis, S. R.; Fang, H.; Minne, S. C.; Hunt, T.; Dai, H.; Harris, J.; Quate, C. F., Experimental and theoretical results of room-temperature single-electron transistor formed by the atomic force microscope nano-oxidation process. *Journal of Vacuum Science & Technology a-Vacuum Surfaces and Films* **2000,** *18* (4), 1321-1325.

34. Piner, R. D.; Zhu, J.; Xu, F.; Hong, S. H.; Mirkin, C. A., "Dip-pen" nanolithography. *Science* **1999,** *283* (5402), 661-663.

35. Su, M.; Dravid, V. P., Colored ink dip-pen nanolithography. *Applied Physics Letters* **2002,** *80* (23), 4434-4436.

36. Demers, L. M.; Ginger, D. S.; Park, S. J.; Li, Z.; Chung, S. W.; Mirkin, C. A., Direct patterning of modified oligonucleotides on metals and insulators by dip-pen nanolithography. *Science* **2002,** *296* (5574), 1836-1838.

37. Mirkin, C. A.; Hong, S. H.; Demers, L., Dip-pen nanolithography: Controlling surface architecture on the sub-100 nanometer length scale. *Chemphyschem* **2001,** *2* (1), 37-39.

38. Mamin, H. J.; Rugar, D., Thermomechanical Writing with an Atomic Force Microscope Tip. *Applied Physics Letters* **1992,** *61* (8), 1003-1005.

39. Mamin, H. J., Thermal writing using a heated atomic force microscope tip. *Applied Physics Letters* **1996,** *69* (3), 433-435.

40. King, W. P.; Goodson, K. E., Thermomechanical formation of nanoscale polymer indents with a heated silicon tip. *Journal of Heat Transfer-Transactions of the Asme* **2007,** *129* (11), 1600-1604.

CHAPTER 2

EXFOLIATION OF GRAPHENE SHEETS BY AN ELECTRON DONOR SURFACTANT

A novel macromolecular surfactant dicholesteryldithienothiophene (ChDTT) was synthesized by Dr. Janusz Kowalik in Dr. Tolbert's group and optimized for use in graphene exfoliation and dispersion. By simple sonication of expandable graphite in solutions containing ChDTT, graphene sheets with sizes exceeding 50 micrometers were observed and characterized by transmission electron microscopy (TEM), atomic force microscopy (AFM), Raman, and X-ray photoelectron (XPS) spectroscopies. The new surfactant is more efficient than poly(m-phenylenevinylene-co-2,5-dioctyloxy-p-phenylenevinylene) (PmPV), avoids polymeric materials, and can be cleanly removed by thermal treatment. Using this surfactant, graphene flakes can be extracted directly from highly oriented pyrolytic graphite (HOPG) without additional chemical, mechanical, or thermal treatment, producing larger flakes of higher quality.

2.1 Introduction

Production of single layer graphene, whose isolation was originally considered unrealistic[1], has attracted extensive recent scientific and technological interest. Graphene is a monolayer of sp^2-bonded carbon atoms tightly packed into a two-dimensional honeycomb lattice characterized by the benzene repeat unit and is the basic building block unit for many carbon allotropes with other dimensionality, e.g. carbon nanotubes (CNTs), fullerenes, and graphite. Depending upon confinement, graphene has a number of fascinating properties including ultra high electron mobility[2], ballistic transport over 0.4 μm^2, anomalous quantum Hall effects[3], and semiconducting properties[4]. It should be

noted that these physical properties are not confined to single layer graphene. Zhang etc. reported that the bandgap of mechanical exfoliated bilayer graphene is opened and continuously tunable by independently varying the top and bottom gate voltage in a dual-gate field-effect transistor[5], while single layer graphene has an intrinsically zero bandgap. A similar phenomenon has also been observed in epitaxial bilayer graphene by changing carrier concentration (doping) on one side[6]. With an additional graphene layer, bilayer graphene exhibits an unconventional quantum Hall effect[7]. For trilayer graphene, applying a perpendicular electric field results in band overlap and makes it a semimetal[8]. So in a generalized definition, "multi-layer graphene" (MLG) can be defined as a graphite containing fewer than ten layers[1]. Beyond that limit, the difference in band overlap between MLG and bulk graphite is less than 10% [9].

When attempting to obtain AFM images of a self-organizing surfactant on HOPG, Dr. Tolbert and his colleagues found very thin "transparent" films of a material with the appearance of graphene (see Figure 2-1). This inspired our studies in the following chemical exfoliation method.

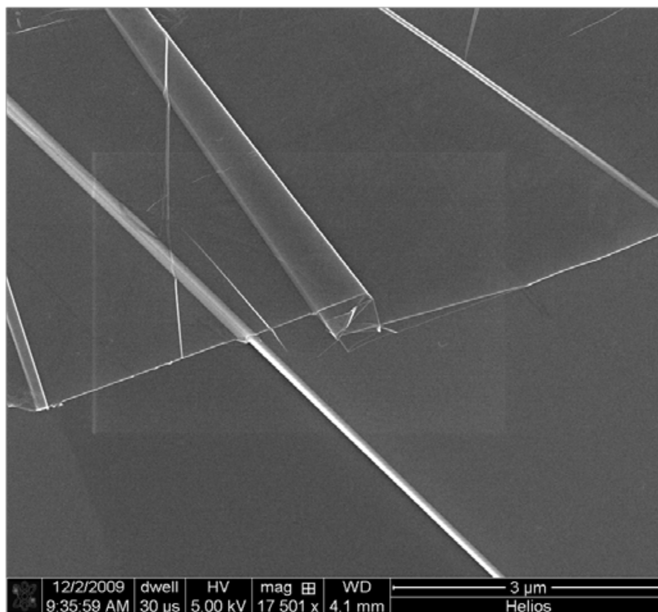

Figure 2-1: Films of ChDTT on HOPG

2.2 Background

Although at least 4 effective methods have been reported for preparation of graphene in the past few years, mechanical exfoliation is still the best method for research quantities of single layer graphene. Large scale graphene production can be divided into two categories: epitaxial growth by chemical methods, such as chemical vapor deposition (CVD)[10, 11] or SiC annealing[12]; and chemical exfoliation from graphite in the liquid phase[13-15]. Compared to CVD or SiC methods, which suffer from non-uniformity and layer control issues, liquid phase exfoliation offers large volume processing. The first issued liquid phase process[16, 17] is the dispersion and reduction of graphene oxide (GO). Considering the poor conductivity resulting from the interruption of the graphene sp^2 structure, several liquid phase methods involving direct exfoliation of graphene from graphite materials have been developed. By matching the surface energy between solvent and graphene, single layer graphene flakes were successfully exfoliated into different solvents such as N-methylpyrrolidone (NMP) and hexafluorobenzene (C_6F_6)[13, 18, 19]. Ionized surfactants[14, 20, 21] and macromolecules[4, 22] have also been used to exfoliate pristine or chemically functionalized[15, 23]graphene flakes by means of surface charge repulsion or steric destabilization. Liquid phase methods are suitable for various processes, including chemical modification, impregnation, mixing, casting, and spin-coating. A solution phase differentiation method which can separate graphene with controlled thickness has also been recently reported[20]. Combined with various deposition techniques, e.g. dielectrophoresis[24] or Langmuir-Blodgett[23] films, liquid phase exfoliation enables the fabrication of graphene arrays with monodispersed thickness.

In common to all these techniques is the very small size (~100 nm) of the flakes, even with thicker MLG. For solvent assisted exfoliation, the exfoliation capability is also low.[25] To avoid these problems, macromolecules, notably polymers[26-28] and biomolecules[29-31] (such as DNA and peptides), have been intensively employed to isolate CNT. The π-conjugated polymer backbone or DNA non-covalently attaches to the

nanotube surface through $\pi-\pi$ stacking, which preserves the electrical and optical properties of the CNT. Conversely, charge transfer between surfactant and CNT improves the exfoliation capability. Graphene has recently been exfoliated using the same polymer used in a CNT system, poly(m-phenylenevinylene-co-2,5-dioctyloxy-p-phenylenevinylene) (PmPV)[4]. Unlike for CNT, the solubilization of graphene by biomolecules not yet been successful.[25]

2.3 Results and Discussion

Our new macromolecular surfactant, dicholesteryldithienothiophene (ChDTT) consists of a central π-conjugated core, i.e. DTT, which can adsorb graphene surface through charge-transfer interaction, and cholesteryl side chains. Such groups, which are widely distributed components of surfactants in nature, were incorporated into DTT to provide both solubility and nonbonding interactions. Recently, Janowska et al. has reported that large size graphene flakes (average about 10 μm) can be synthesized in water or ammonia by a series of sonication and microwave treatments[21]. However, graphene oxidation (in water) or nitrogen doping (in ammonia) still cannot be avoided. Using their procedure as a model, we investigated whether the material in Figure 2-1 was indeed graphene and if it could be used to make, first, graphene flakes and, then, uniform sheets. For comparison purposes, another popular macromolecular surfactant, PmPV, has also been synthesized. Transmission electron microscopy (TEM) and atomic force microscopy (AFM) analysis, revealed the presence of large size, multi-layer graphene sheets with a high level of exfoliation in ChDTT-containing solution. Raman spectroscopy confirmed that the ultra-large graphene sheet (50 μm) was as thin as 5 layers. X-ray photoelectron (XPS) spectroscopy also indicated that ChDTT could be totally removed by thermal treatment, leaving defect free and very slightly oxidized graphene flakes, which is not possible in the PmPV system. In addition, the success of

exfoliating large MLG directly from highly oriented pyrolytic graphite (HOPG) further demonstrates the extraordinary exfoliation ability of ChDTT. Complete details of the synthesis and properties of this unusual cholesteric discotic liquid crystal will be reported elsewhere.

The graphite intercalation compound (GIC) was first expanded by thermal shock. The procedure is described as follows: First, commercially available “expandable graphite” (NYACOL NYAGRAPH 351), was quickly heated to 1000°C for 1 min under forming gas. The resulting black expanded graphite powder was dispersed in a 1,2-dichloroethane (DCE) solution of ChDTT or PmPV (0.1mg/mL). The solution was ultrasonicated for 30 min and centrifuged under 14K RPM for 10 min. The clear supernatant, containing flakes of single or multi-layer graphene, was collected for further analysis. Characterization methods included Raman spectroscopy (Renaishaw 2000, 488nm), X-ray photoelectron spectroscopy (XPS, Thermo-K Alpha), atomic force microscopy (AFM, Agilent picoplus system), transmission electron microscopy (TEM, JEOL 100CX II, 100kV), scanning electron microscopy (SEM, Zeiss Gemini Ultra-60), thermogravity analysis (TGA, Texas Instrument Q500), and UV-Vis spectrometer.

Figure 2-2: The synthesis route of Dicholesteryl-dithienothiophene (ChDTT)

PmPV is known to disperse CNT and graphene by $\pi - \pi$ stacking between π-conjugated backbone and the aromatic surface. To prove our idea that the DTT core plays the same role in our newly designed ChDTT system, UV-Vis spectroscopy was used to monitor the absorption change for both ChDTT and PmPV after the surfactant-graphite interaction. A 2 mg portion of thermal expanded graphite was added to 0.01mM ChDTT/DCE solution. After stirring for 90 minutes, the mixture was filtered through a 0.2 μm PTFE filter to remove unreacted graphite. Unlike ultrasonication, mild stirring did not exfoliate expanded graphite. Figure 2-3 displays the UV-Vis spectra of a ChDTT/DCE solution before and after graphite immersion. It shows an absorption decrease, indicating a decrease in ChDTT concentration according to the Beer's law. Under higher concentrations and reaction times (20 mg expanded graphite and 16 hour stir), the absorption peaks between 300 to 400 nm are gone (line c in Figure 2-3), implying that ChDTT molecules were adsorbed on the expanded graphite surface and removed from solution. Similar absorption changes in the PmPV/DCE system are described in the supplementary material. These results suggest that the dispersion mechanism of ChDTT is similar to that of PmPV, involving charge transfer between surfactant and graphene. During ultrasonication, expanded graphite exfoliated to thinner pieces.

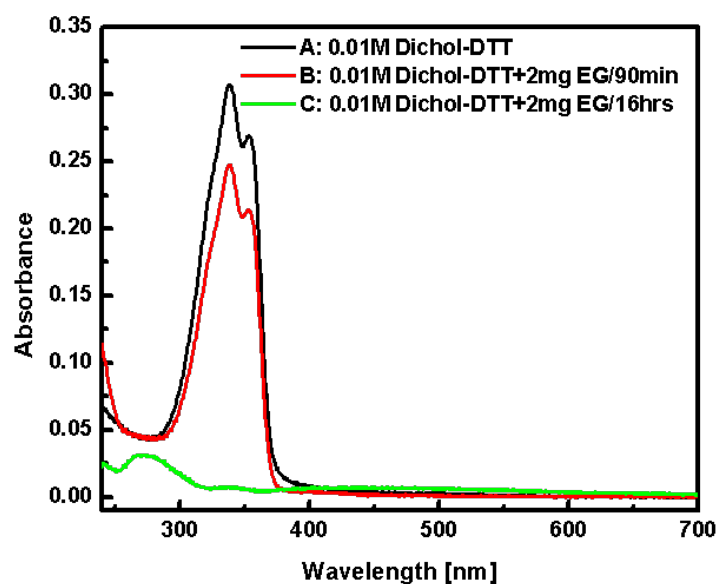

Figure 2-3: Absorption spectra of: A) ChDTT in 1,2-DCE, 0.01 mM solution; B) After addition of 2mg expandable carbon to the mother solution and stirring for 90 min at rt; C) After addition of 20 mg expandable carbon and stirring for 16 h at rt. The spectra were normalized at the baseline.

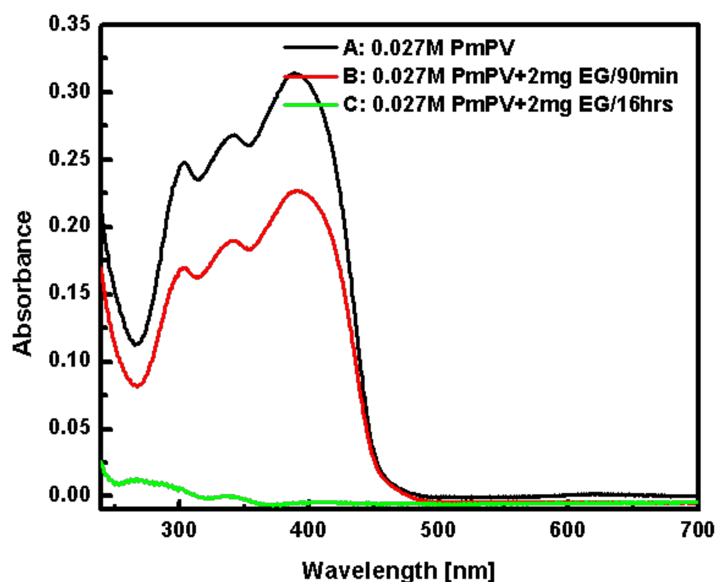

Figure 2-4: Absorption spectra of: A) Poly(m-henylenevinylene-co-2,5-dioctyloxy-p-phenylenevinylene) (PmPV) in 1,2-DCE, 0.027 mM solution; B) After addition of 2 mg expandable carbon to the mother solution and stirring for 90 min at rt; C) After addition of 20 mg expandable carbon and stirring for 16 h at rt.

Transmission electron microscopy (TEM) was used to directly investigate the state of graphene flakes remaining dispersed in the solution. One drop of sonicated and centrifuged ChDTT/EG supernatant was applied on a lacy-carbon TEM grid, dried, and analyzed without further treatment. In addition to flakes of several□µm, ultra-large graphene sheets (over 20 µm) were frequently found. Figure 2-5 (a) shows a combination of these two types of graphene flakes: one edge of an ultra-large graphene sheet with several small embedded pieces. It is well known that the surface tension of graphene flake preparations is not high enough to support a high aspect ratio (20µm across vs. few atomic layers thick) [21]. Folded edges and crumples are always observed in these large flakes. In addition, significant particle formation suggests ChDTT residues, which were not remove. To characterize the thickness and uniformity of ultra-large flakes, small aperture selective-area electron diffraction (SAED) was probed at different area of this sample. Figure 2-5 (c) and 2-5 (d) show SAED patterns from two specific spots in Figure 2-5 (a) and labeled with Miller-Bravais (hkil) indices. They both clearly demonstrate a single set of hexagonal patterns without superimposed shifting diffraction, indicating no stacked MLG layers with twisting angles at these spots. In Figure 2-5 (c), higher intensity {1100} peaks (the first hexagonal ring) relative to {2110} (the second hexagonal ring) represent the fingerprint of single-layer graphene. While focusing on other areas, Figure 2d shows stronger {2110} peaks, demonstrating multilayer with Bernal AB stacking. We note that no border is observed in this type of ultra-large MLG, which suggests that this is a single continuous MLG sheet. It is reported that the ultra-large MLG sheet was always made up of smaller individual graphene flakes with an obvious boundary[21]. We believe this is the first graphene sheet of this size exfoliated in single piece.

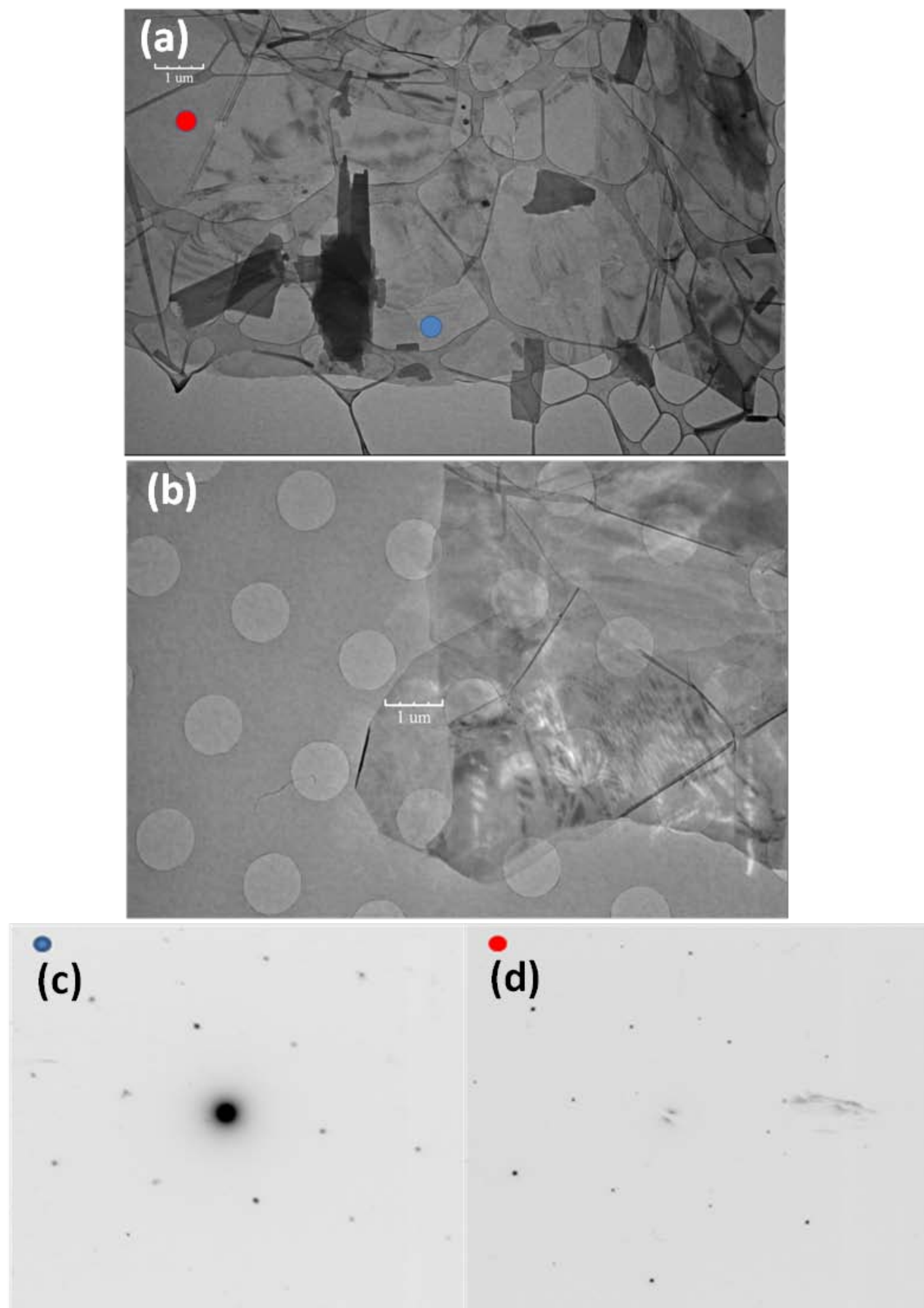

Figure 2-5: (a), (b) TEM image of one edge of as-synthesized ultra-large graphene sheet with size > 20μm. The graphene sheet is folded with several small size graphene sheets embedded in it. (c), (d) Selective-area electron diffraction (SAED) patterns in (a) show that it contains different number of layers (from single layer to few layers) at different part.

Selected TEM images of regular flakes are also shown in Figure 2-6. Comparing to typical exfoliation methods, which generate graphene flakes around several hundred nanometers, this type of few micrometer flakes have already been much bigger in lateral size. Figure 2-6 (d) is a large aperture SAED pattern taken from the flake shown in (c), indicating MLG with uniform number of layers through the whole sheet.

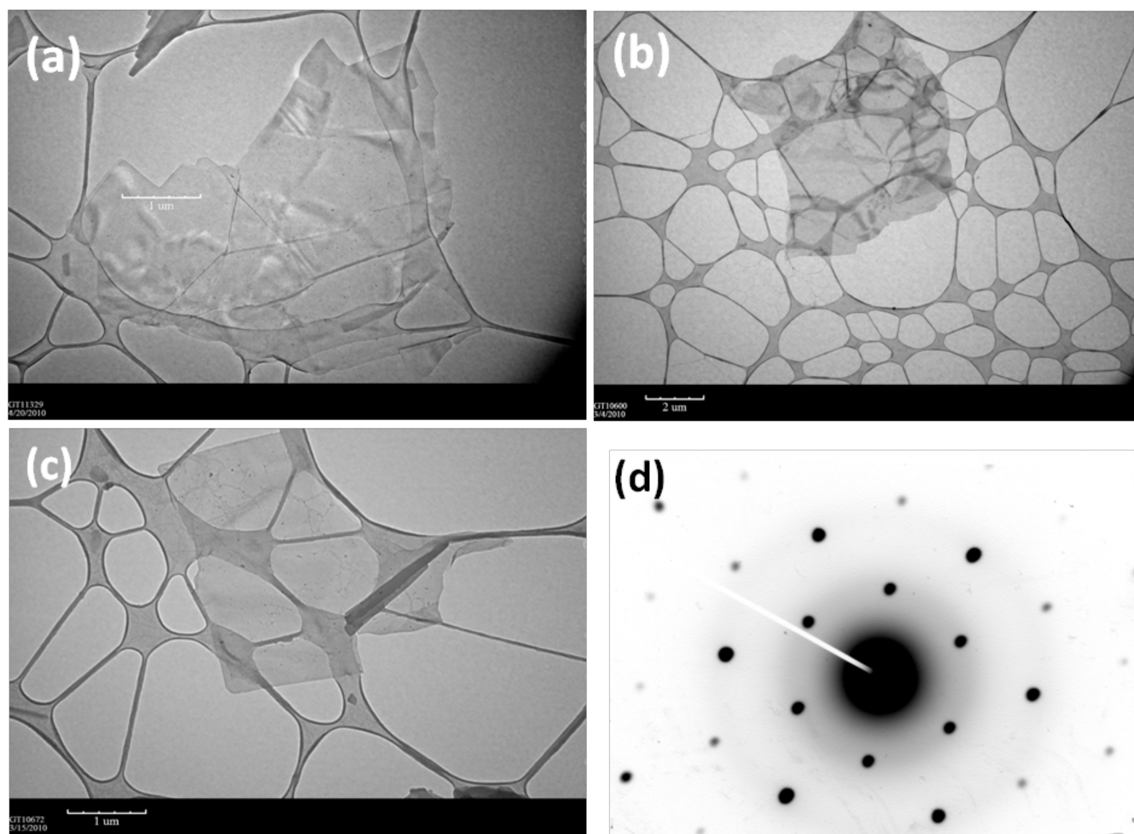

Figure 2-6: TEM images of some representative graphene sheets with average size (several micron meters). SAED with larger aperture shows that they are uniform few-layer grapheme.

In order to further characterize the number of layers in our MLG, micro-Raman spectrometry was used to probe single graphene flakes made by ChDTT exfoliation. Graphene flakes were deposited on a silicon wafer with 300nm thermal oxide by drop casting. The sample was then heated to 400℃ in air to remove the surfactant. The significant contrast between SiO_2 background and graphene flakes makes individual thin sheets visible under the 50X optical microscope, and a well aligned 2 μm laser beam with

488nm wavelength was able to focus on a specific spot. Graphitic carbon materials display three fingerprints in Raman spectra: the G (Graphite) band at ~ 1580cm^{-1}, the 2D band (or G' band) at ~2700cm^{-1}, and the disordered D (defect) band at ~1350cm^{-1}. The evolution of the Raman spectra from graphite to MLG to single-layer graphene under different laser wavelengths has been intensively studied[32]. For visible Raman spectra (488nm and 514mnm), both the intensity ratio of the 2D band to G band (I_G/I_{2D}) and the shape of 2D band are layer sensitive[33-35]. With a 488nm laser and 300 nm SiO_2, the I_G/I_{2D} ratio has specific value of 2.1, 1.49, 1.14, 0.74, and 0.24 for 5, 4, 3, 2, and 1 layer graphene, respectively[33]. Moreover, the 2D band is a single Lorentzian peak for single layer graphene, while the same peak for double layer graphene deconvolves into 4 Lorentzian peaks, which can be explained by the double-resonant model for graphene[32]. With an increase of layers, at least 6 Lorentzians to fit tri-layer graphene and 3 Lorentzians for MLG over 4 layers must be used[36]. Further increases in layers leads to a significant increase of the relative intensity of the highest energy peak until it reaches the limit of bulk graphite. For graphite itself, the 2D band is assigned to 2 convolved peaks with approximately 1/4 and 1/2 the height of the G peak, respectively. To characterize the precise thickness of our ultra-large graphene flakes, sheets of ~7µm, 20 µm, and 50 µm diameter were probed by micro-Raman spectroscopy along with HOPG for comparison. Figure 2-7 (a) shows the wide range Raman spectra (1000 cm^{-1} ~ 3000 cm^{-1}) of these flakes. From the intensity ratio (I_G/I_{2D}), we can estimate: (1) the 50 µm flake (I_G/I_{2D}=2.18) is approximately 5 layers, (2) the 20 µm flake (I_G/I_{2D}=1.5) is approximately 4 layers, and (3) the 7µm flake (I_G/I_{2D}=1.16). The 2D band deconvolution shown in Figure 2-7 (b) can provide further information about the layer number. For 50 µm and 20 µm flakes, the 2D band shows a typical MLG shape (intensity at higher wave number is slightly stronger) and can be fit with 3 Lorentzian peaks. Again, the intensity of the highest energy peak for the 50 µm flake is stronger than for the 20 µm flake and much weaker than that HOPG. Combined with the I_G/I_{2D} ratio, this demonstrates that they are 5-layer and 4-layer

graphene flakes. For the 7 μm flake, the special 2D band shape can only be fit with at least 6 Lorentzians. Together with the I_G/I_{2D} ratio, this also coincides with the features of 3 layer graphene. It should be noted that no defect band (~1350 cm^{-1}) can be found in either of these flakes, implying that no structure disorder was introduced during our processes.

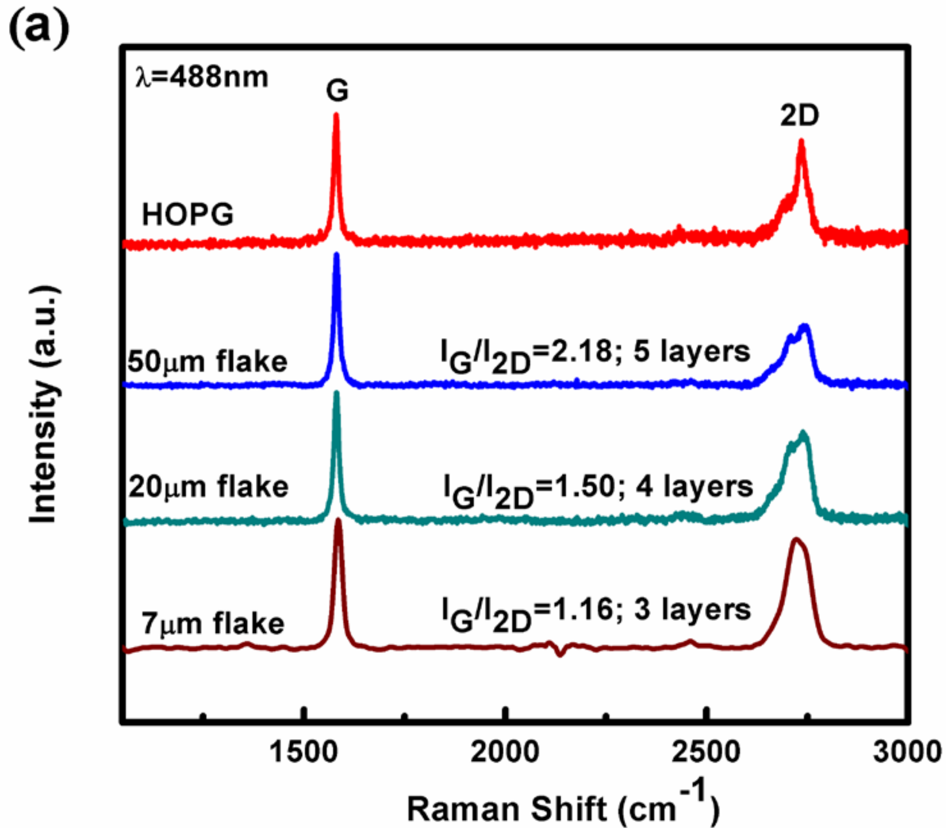

Figure 2-7: (a). Raman spectra for HOPG and ChDTT exfoliated graphene flakes with approximately 50μm, 20μm, and 7μm in size. Graphene flakes were deposited on a silicon wafer with 300nm oxide by drop casting. The wavelength of the Raman laser is 488nm and the laser spot is 2 μm in diameter. The intensity ratios of G band and 2D band (I_G/I_{2D}) of 50μm, 20μm, and 7μm flakes are 2.18, 1.5, and 1.16 individually. They match the reported value in literature of 2.1, 1.49, and 1.14 for 5 layer, 4 layer, and 3 layer graphene individually.

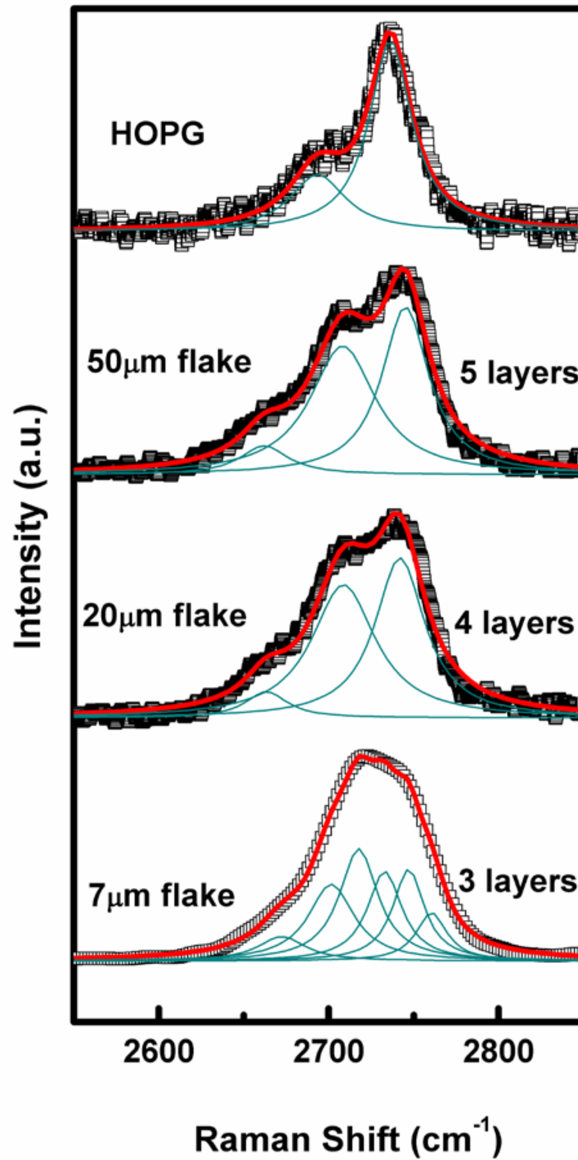

Figure 2-7: **(b)**. The deconvolution of 2D band of Raman spectra in (a). Black squares are experimental measurement. Red solid lines are fitting results. For bulk graphite (HOPG), 2D band can be deconvoluted into 2 Lorentzian peaks, and the peak with higher wave number is much stronger than the other. For 50μm and 20μm flakes, 2D bands are well fitted by 3 Lorentzians convolution, indicating MLG with 5 or 4 layers. For 7μm flake, the 2D band has to be fitted with at least 6 Lorentzians. It also matches the criteria of tri-layer graphene.

Although it is suggested that macromolecular surfactants, such as PmPV and DNA, interact with CNT and graphene through $\pi - \pi$ stacking, thoroughly removing surfactant is still essential due to the sensitivity of electronic properties to surface condition. The challenge relates not only to the surfactant removal, but also the preservation of sp^2 carbon structure. For this reason, Li.et al. has attempted to remove PmPV using a two-step decomposition. First, a PmPV/graphene cast SiO_2 sample was heated to 400°C in air to combust most of the polymer. To avoid the oxidation of graphene, a second-stage combustion with higher temperature (600˚C) was performed under ultra-high vacuum. To realize the high-temperature decomposition behaviors of our ChDTT, thermal gravimetric analysis (TGA) was performed in both air and inert condition (argon) along with PmPV for comparison. Figure 2-8 (a) shows the TGA results for both materials under both environments. For the first stage, ChDTT has about 35% remaining mass at 400°C, whereas PmPV retains 58%. Although ChDTT seems to have less residue, atomic force microscopy (AFM) images taken after equal thermal treatment still showed significant quantities of remaing. (Fig. 2-8 (c)) Before further thermal treatment, samples were immersed in 6M nitric acid for 1 hour to chemically decompose the surfactants. Nitric acid is known to effectively oxidize graphite to graphite oxide, which makes a reasonable assumption that graphene flakes should have equal effect. The AFM showed a clean surface for ChDTT/graphene (Fig. 2-8 (e)), but not for PmVP/graphene (Fig. 2-8 (d)).

X-ray photoelectron spectroscopy (XPS) was then used to examine the carbon bonding state of nitric acid treated graphene (Fig. 2-9 (b)). Typically the graphene carbon 1s (C_{1s}) peak in the XPS spectrum is dominated by C-C bond scattering located at 284.5eV. In addition, 3 minor C_{1s} components are assigned to C-O, C=O, and O=C-OH, with 1.5eV, 2.5eV, and 4eV shifts on the higher energy side[37]. Not surprisingly, the C_{1s} XPS spectra of nitric acid treated samples show strong oxidation states in all C-O, C=O, and COOH bonding regimes. Thus the 2D carbon plane was extensively oxygenated, and

the flakes tended toward graphene oxide. An alternative method is the second-stage thermal treatment, involving high temperature heating under inert gas. The TGA curve of PmPV (in Ar) reveals remaining residue up to 1000°C (Fig. 2-8 (a)). The AFM image also supports the conclusion that PmPV cannot be removed under these circumstances (Fig. 2-8 (f)). Conversely, ChDTT was totally removed before 700°C. The AFM also shows a clean surface after 800°C rapid thermal processor (RTP) treatment. Again, XPS was performed to examine the carbon 1s state (Fig. 2-9(c)). After deconvolution, it revealed only minor oxidation compared to nitric acid treatment. The C_{1s} XPS spectrum of the starting material, expanded graphite, is also shown in Figure 2-9 (a). The difference between starting material and product flakes implies that our process, including ChDTT exfoliation and thermal treatment, did not result in extensive oxidation. The insets of Figure 2-9 (c) also show the high-resolution scans at N_{1s} and S_{2p} binding energies, the two elements other than carbon in ChDTT). No such elements were seen, futher supporting the AFM results.

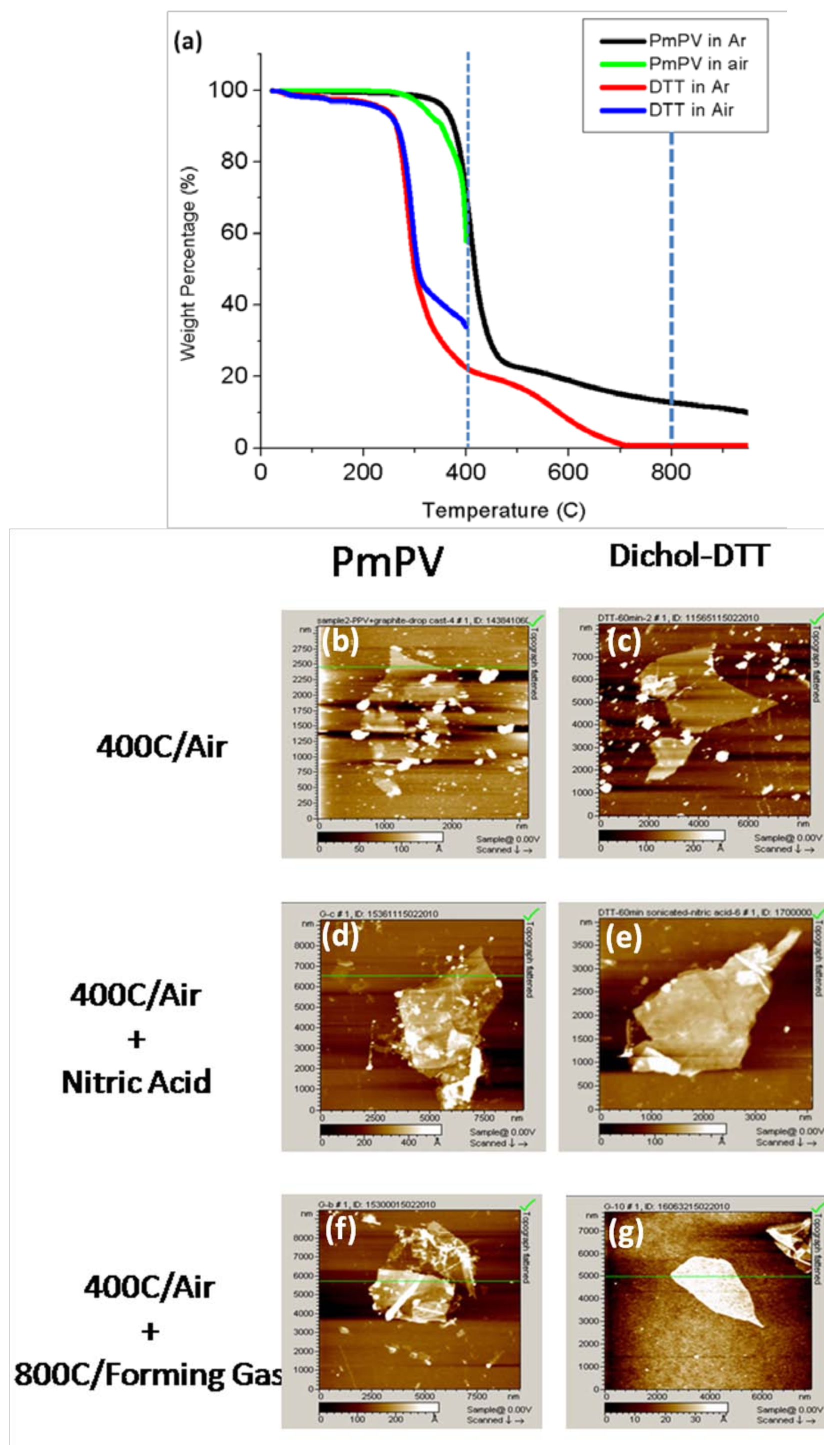

Figure 2-8: PmPV and ChDTT under various removal procedures. (a) TGA results show that both materials can not be decomposed by barely heated to 400° C in air. Further thermal treatment at 800° C under argon can totally decompose ChDTT, but PmPV still remained around 15 wt %. (b)-(f) AFM analyses also show that ChDTT residues can be cleaned up by either thermal treatment or nitric acid treatment. But there are still lots of residues for PmPV exfoliated graphene sheets after either method.

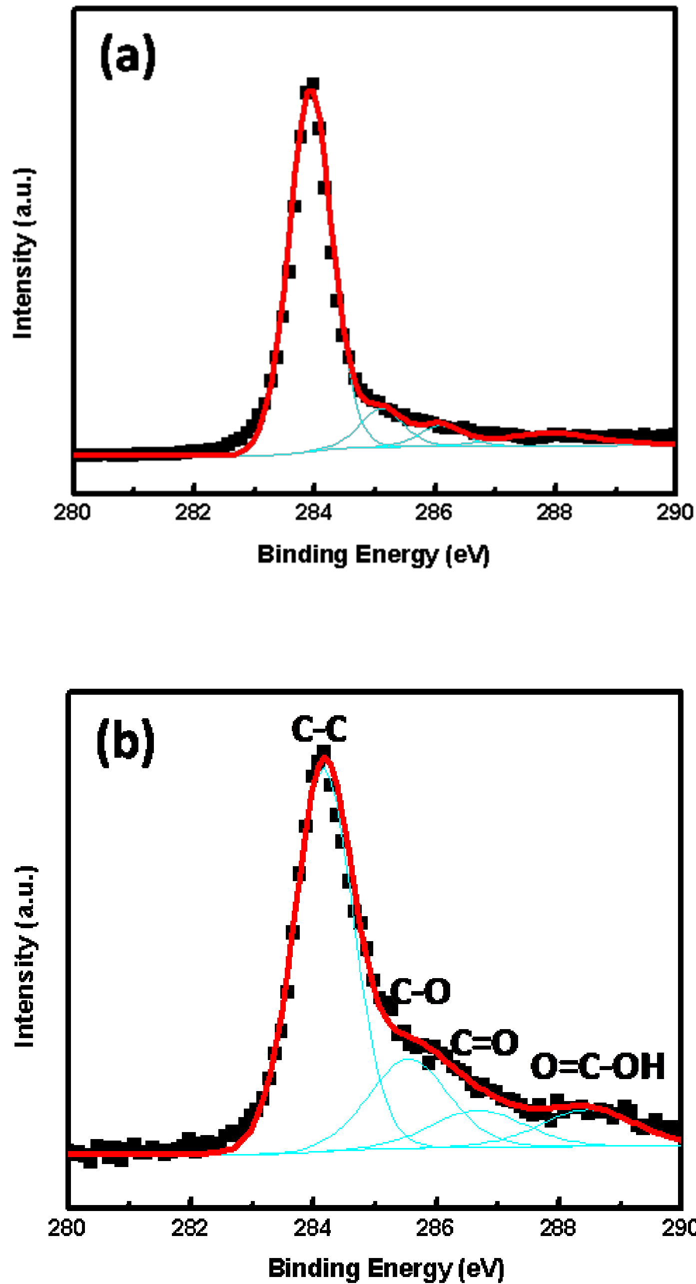

Figure 2-9: XPS high-resolution C_{1S} peak for expanded graphite (a), after 6M nitric acid treatment for 1 hr (b), and after 800° C thermal treatment in forming gas

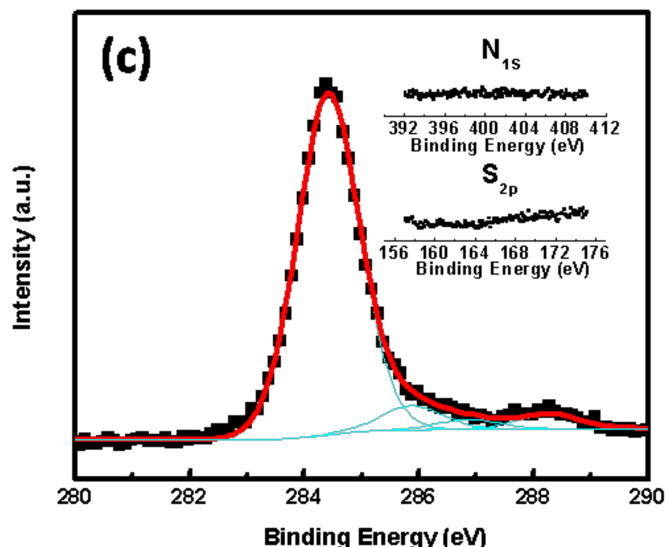

Figure 2-9: XPS high-resolution C_{1S} peak for expanded graphite (c). The Shirley background has been applied. All spectra are fitted with C-C peak at 284.4 eV, C-O peak at 285.9eV, C=O peak at 286.9 eV, and COOH at 288.4 eV. It clearly shows that the thermal treatment can avoid the graphene oxidation problem. Inset spectrum in (c) is the N_{1s} and S_{2p} peak. It also proves that no ChDTT remains.

2.4 Conclusions

The use of non-polymeric surfactants such as ChDTT offers a convenient route to large-area pieces graphene which may be further manipulated mechanically or through lithographic techniques. An important issue, obviously, is mechanical handling. The use of ultrasonication provides a means to create suspensions which can be coated onto surfaces. However, methods to directly move large pieces of graphene onto other surfaces without such mechanical disruption are obviously desirable. Such techniques are under investigation.

2.5 References

1. Geim, A. K.; Novoselov, K. S., The rise of graphene. *Nature Materials* **2007,** *6* (3), 183-191.

2. Novoselov, K. S.; Geim, A. K.; Morozov, S. V.; Jiang, D.; Zhang, Y.; Dubonos, S. V.; Grigorieva, I. V.; Firsov, A. A., Electric field effect in atomically thin carbon films. *Science* **2004,** *306* (5296), 666-669.

3. Zhang, Y. B.; Tan, Y. W.; Stormer, H. L.; Kim, P., Experimental observation of the quantum Hall effect and Berry's phase in graphene. *Nature* **2005,** *438* (7065), 201-204.

4. Li, X. L.; Wang, X. R.; Zhang, L.; Lee, S. W.; Dai, H. J., Chemically derived, ultrasmooth graphene nanoribbon semiconductors. *Science* **2008,** *319* (5867), 1229-1232.

5. Zhang, Y. B.; Tang, T. T.; Girit, C.; Hao, Z.; Martin, M. C.; Zettl, A.; Crommie, M. F.; Shen, Y. R.; Wang, F., Direct observation of a widely tunable bandgap in bilayer graphene. *Nature* **2009,** *459* (7248), 820-823.

6. Ohta, T.; Bostwick, A.; Seyller, T.; Horn, K.; Rotenberg, E., Controlling the electronic structure of bilayer graphene. *Science* **2006,** *313* (5789), 951-954.

7. Novoselov, K. S.; McCann, E.; Morozov, S. V.; Fal'ko, V. I.; Katsnelson, M. I.; Zeitler, U.; Jiang, D.; Schedin, F.; Geim, A. K., Unconventional quantum Hall effect and Berry's phase of 2 pi in bilayer graphene. *Nature Physics* **2006,** *2* (3), 177-180.

8. Craciun, M. F.; Russo, S.; Yamamoto, M.; Oostinga, J. B.; Morpurgo, A. F.; Thrucha, S., Trilayer graphene is a semimetal with a gate-tunable band overlap. *Nature Nanotechnology* **2009,** *4* (6), 383-388.

9. Partoens, B.; Peeters, F. M., From graphene to graphite: Electronic structure around the K point. *Physical Review B* **2006,** *74* (7), -.

10. Kim, K. S.; Zhao, Y.; Jang, H.; Lee, S. Y.; Kim, J. M.; Kim, K. S.; Ahn, J. H.; Kim, P.; Choi, J. Y.; Hong, B. H., Large-scale pattern growth of graphene films for stretchable transparent electrodes. *Nature* **2009,** *457* (7230), 706-710.

11. Reina, A.; Jia, X. T.; Ho, J.; Nezich, D.; Son, H. B.; Bulovic, V.; Dresselhaus, M. S.; Kong, J., Large Area, Few-Layer Graphene Films on Arbitrary Substrates by Chemical Vapor Deposition. *Nano Letters* **2009,** *9* (1), 30-35.

12. Berger, C.; Song, Z. M.; Li, X. B.; Wu, X. S.; Brown, N.; Naud, C.; Mayou, D.; Li, T. B.; Hass, J.; Marchenkov, A. N.; Conrad, E. H.; First, P. N.; de Heer, W. A., Electronic confinement and coherence in patterned epitaxial graphene. *Science* **2006,** *312* (5777), 1191-1196.

13. Hernandez, Y.; Nicolosi, V.; Lotya, M.; Blighe, F. M.; Sun, Z. Y.; De, S.; McGovern, I. T.; Holland, B.; Byrne, M.; Gun'ko, Y. K.; Boland, J. J.; Niraj, P.; Duesberg, G.; Krishnamurthy, S.; Goodhue, R.; Hutchison, J.; Scardaci, V.; Ferrari, A. C.; Coleman, J. N., High-yield production of graphene by liquid-phase exfoliation of graphite. *Nature Nanotechnology* **2008,** *3* (9), 563-568.

14. Lotya, M.; Hernandez, Y.; King, P. J.; Smith, R. J.; Nicolosi, V.; Karlsson, L. S.; Blighe, F. M.; De, S.; Wang, Z. M.; McGovern, I. T.; Duesberg, G. S.; Coleman, J. N., Liquid Phase Production of Graphene by Exfoliation of Graphite in Surfactant/Water Solutions. *Journal of the American Chemical Society* **2009,** *131* (10), 3611-3620.

15. Sun, Z. Z.; Kohama, S.; Zhang, Z. X.; Lomeda, J. R.; Tour, J. M., Soluble graphene through edge-selective functionalization. *Nano Research* **2010,** *3* (2), 117-125.

16. Dikin, D. A.; Stankovich, S.; Zimney, E. J.; Piner, R. D.; Dommett, G. H. B.; Evmenenko, G.; Nguyen, S. T.; Ruoff, R. S., Preparation and characterization of graphene oxide paper. *Nature* **2007,** *448* (7152), 457-460.

17. Li, D.; Muller, M. B.; Gilje, S.; Kaner, R. B.; Wallace, G. G., Processable aqueous dispersions of graphene nanosheets. *Nature Nanotechnology* **2008,** *3* (2), 101-105.

18. Blake, P.; Brimicombe, P. D.; Nair, R. R.; Booth, T. J.; Jiang, D.; Schedin, F.; Ponomarenko, L. A.; Morozov, S. V.; Gleeson, H. F.; Hill, E. W.; Geim, A. K.; Novoselov, K. S., Graphene-based liquid crystal device. *Nano Letters* **2008,** *8* (6), 1704-1708.

19. Bourlinos, A. B.; Georgakilas, V.; Zboril, R.; Steriotis, T. A.; Stubos, A. K., Liquid-Phase Exfoliation of Graphite Towards Solubilized Graphenes. *Small* **2009,** *5* (16), 1841-1845.

20. Green, A. A.; Hersam, M. C., Solution Phase Production of Graphene with Controlled Thickness via Density Differentiation. *Nano Letters* **2009,** *9* (12), 4031-4036.

21. Janowska, I.; Chizari, K.; Ersen, O.; Zafeiratos, S.; Soubane, D.; Da Costa, V.; Speisser, V.; Boeglin, C.; Houlle, M.; Begin, D.; Plee, D.; Ledoux, M. J.; Pham-Huu, C., Microwave synthesis of large few-layer graphene sheets in aqueous solution of ammonia. *Nano Research* **2010,** *3* (2), 126-137.

22. Bourlinos, A. B.; Georgakilas, V.; Zboril, R.; Steriotis, T. A.; Stubos, A. K.; Trapalis, C., Aqueous-phase exfoliation of graphite in the presence of polyvinylpyrrolidone for the production of water-soluble graphenes. *Solid State Communications* **2009,** *149* (47-48), 2172-2176.

23. Liu, X. F.; Zhu, M.; Chen, S. H.; Yuan, M. J.; Guo, Y. B.; Song, Y. L.; Liu, H. B.; Li, Y. L., Organic-Inorganic Nanohybrids via Directly Grafting Gold Nanoparticles onto Conjugated Copolymers through the Diels-Alder Reaction. *Langmuir* **2008,** *24* (20), 11967-11974.

24. Vijayaraghavan, A.; Sciascia, C.; Dehm, S.; Lombardo, A.; Bonetti, A.; Ferrari, A. C.; Krupke, R., Dielectrophoretic Assembly of High-Density Arrays of Individual Graphene Devices for Rapid Screening. *Acs Nano* **2009,** *3* (7), 1729-1734.

25. Coleman, J. N., Liquid-Phase Exfoliation of Nanotubes and Graphene. *Advanced Functional Materials* **2009,** *19* (23), 3680-3695.

26. Dalton, A. B.; Stephan, C.; Coleman, J. N.; McCarthy, B.; Ajayan, P. M.; Lefrant, S.; Bernier, P.; Blau, W. J.; Byrne, H. J., Selective interaction of a semiconjugated organic polymer with single-wall nanotubes. *Journal of Physical Chemistry B* **2000,** *104* (43), 10012-10016.

27. Murphy, R.; Coleman, J. N.; Cadek, M.; McCarthy, B.; Bent, M.; Drury, A.; Barklie, R. C.; Blau, W. J., High-yield, nondestructive purification and quantification method for multiwalled carbon nanotubes. *Journal of Physical Chemistry B* **2002,** *106* (12), 3087-3091.

28. Cadek, M.; Coleman, J. N.; Ryan, K. P.; Nicolosi, V.; Bister, G.; Fonseca, A.; Nagy, J. B.; Szostak, K.; Beguin, F.; Blau, W. J., Reinforcement of polymers with carbon nanotubes: The role of nanotube surface area. *Nano Letters* **2004,** *4* (2), 353-356.

29. Zheng, M.; Jagota, A.; Strano, M. S.; Santos, A. P.; Barone, P.; Chou, S. G.; Diner, B. A.; Dresselhaus, M. S.; McLean, R. S.; Onoa, G. B.; Samsonidze, G. G.; Semke, E. D.; Usrey, M.; Walls, D. J., Structure-based carbon nanotube sorting by sequence-dependent DNA assembly. *Science* **2003,** *302* (5650), 1545-1548.

30. Nakashima, N.; Okuzono, S.; Murakami, H.; Nakai, T.; Yoshikawa, K., DNA dissolves single-walled carbon nanotubes in water. *Chemistry Letters* **2003,** *32* (5), 456-457.

31. Gigliotti, B.; Sakizzie, B.; Bethune, D. S.; Shelby, R. M.; Cha, J. N., Sequence-independent helical wrapping of singles-walled carbon nanotubes by long genomic DNA. *Nano Letters* **2006,** *6* (2), 159-164.

32. Ferrari, A. C.; Meyer, J. C.; Scardaci, V.; Casiraghi, C.; Lazzeri, M.; Mauri, F.; Piscanec, S.; Jiang, D.; Novoselov, K. S.; Roth, S.; Geim, A. K., Raman spectrum of graphene and graphene layers. *Physical Review Letters* **2006,** *97* (18), -.

33. Calizo, I.; Bejenari, I.; Rahman, M.; Liu, G.; Balandin, A. A., Ultraviolet Raman microscopy of single and multilayer graphene. *Journal of Applied Physics* **2009,** *106* (4), -.

34. Calizo, I.; Balandin, A. A.; Bao, W.; Miao, F.; Lau, C. N., Temperature dependence of the Raman spectra of graphene and graphene multilayers. *Nano Letters* **2007,** *7* (9), 2645-2649.

35. Haluska, M.; Obergfell, D.; Meyer, J. C.; Scalia, G.; Ulbricht, G.; Krauss, B.; Chae, D. H.; Lohmann, T.; Lebert, M.; Kaempgen, M.; Hulman, M.; Smet, J.; Roth, S.; von Klitzing, K., Investigation of the shift of Raman modes of graphene flakes. *Physica Status Solidi B-Basic Solid State Physics* **2007,** *244* (11), 4143-4146.

36. Malard, L. M.; Pimenta, M. A.; Dresselhaus, G.; Dresselhaus, M. S., Raman spectroscopy in graphene. *Physics Reports-Review Section of Physics Letters* **2009,** *473* (5-6), 51-87.

37. Yang, D.; Velamakanni, A.; Bozoklu, G.; Park, S.; Stoller, M.; Piner, R. D.; Stankovich, S.; Jung, I.; Field, D. A.; Ventrice, C. A.; Ruoff, R. S., Chemical analysis of graphene oxide films after heat and chemical treatments by X-ray photoelectron and Micro-Raman spectroscopy. *Carbon* **2009,** *47* (1), 145-152.

CHAPTER 3

SYNTHETIC APPROACHES TO GRAPHENE BY CHEMICAL TRANSFORMATIONS OF POLYANTHRACENE

3.1 Introduction

The major challenge of graphene technology is that its native two-dimensional form is semimetallic, and for practical applications in transistor devices, a band gap has to be introduced by modifying its topology to be one-dimensional, i.e. the quantum confinement effect. It has been proven by both calculation and experiment that only a graphene nanoribbon around 10 nm in width can generate a semiconducting property. In other words, an extra effort which involves "cutting" the sheet is not avoidable among existing methods for producing graphene. Although graphene nanoribbons have been made using e-beam lithography,[1, 2] sonochemistry,[3] or through the unzipping of carbon nanotubes,[4-7] there is still no reliable method to produce a ribbon smaller than 10 nm with chemical precision. To fabricate an object with a molecular level dimension, the best way is to use a method which can manipulate molecules: chemical synthesis.

The best known work on chemically synthesizing graphene is from Klaus Mullen and associates. They have introduced a precursor route for which polyphenylene precursors are made by i) repetitive Diels-Alder cycloaddition, ii) cyclotrimerization of acetylenes, or iii) aryl-aryl coupling, and are then subjected to intramolecular cyclodehydrogenation which further aromatizes the structures.[8] A typical case for this is hexaphenylbenzene which transforms smoothly into hexabenzocoronene. Based on this route, many disc type macromolecules have been synthesized. Linear and branched alkyl chains were usually attached to enhance the solubility and meltability. Moreover, because

there is phase separation between the rigid aromatic cores and the flexible alkyl chains, such species form discotic mesophases with columnar superstructures.

For linear and planer structures, Roberson et al. have studied hydrogen transfer during the sublimation of pentacene.[9] A horizontal physical vapor phase reactor has been used to grow crystals for a variety of poly aromatic hydrocarbons under atmospheric conditions,[10] including thiophene, anthraphene, and pentacene. They discovered that pentacene can be oligomerized to polycondensed graphitic structures under the proper temperature gradient. This inspired the investigation of organic semiconductor graphitization by high temperature reactions in this project. From the energy point of view, the graphitic structures should represent a deep energy valley. The energy level of these organic semiconductor precursors should sit close to the valley and can readily drop to the minimum to form the specific structures.

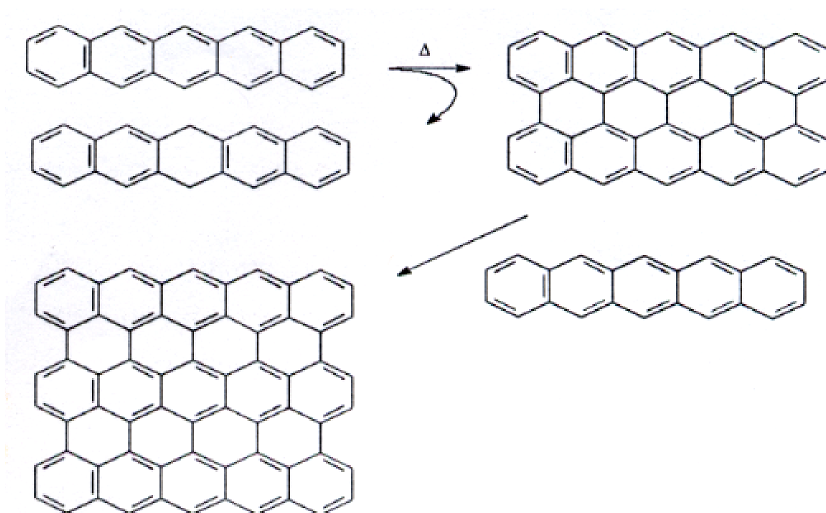

Figure 3-1: Oligomerization of pentacene

Recently, Mullen's group synthesized a planer graphene nanoribbon from anthracene.[11] They first deposited an anthracene precursor onto an Au(111) surface. Through a first thermal activation step at 200°C, the precursor species diffused across the surface and underwent radical addition reactions to form a linear polymer chain. In a

second thermal activation step at 400°C, a surface-assisted cyclodehydrogenation consolidated the polyanthracene and formed a grapheme nanoribbon. The basic concept of Mullen's works is that the pre-ordered mesophase could effectively reduce the pyrolysis temperature of graphitization[12] or consolidation. To make 2-D graphene nanoribbons through thermal treatment, a "lying-down" well-ordered single layer is the necessary condition. Unfortunately, an amorphous SiO_2 surface cannot provide an ordered template for the placement of aromatic groups.[13] Much research has been done on the monolayer orientation of organic small molecule semiconductors. Consider 3,4,9,10-perylene-tetracarboxylic-dianhydride (PTCDA), for example. On an inert or well-ordered substrate, such as hydrogenated silicon, HOPG, and single crystalline metal, PTCDA will form a "lying-down" herringbone array because of the strong hydrogen bonding.[14] While on an amorphous surface, such as SiO_2, ITO, and polycrystalline gold, all those molecules, including PTCDA and pentacene, will form a "standing-up" structure because of the weak interfacial Van der Waal forces.[15] While SAMs are introduced as the connector of the molecules and substrate, PTCDA shows an exclusive lying-down structure which cannot be found in pentacene.[16] Figure 3-2 shows the chemical structure of PTCDA. This illustrates the importance of surface orientation while performing consolidation, and anthracene might be a better precursor than pentacene due to its proven "lying-down" property.

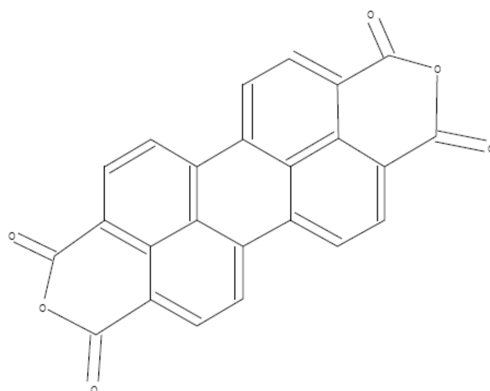

Figure 3-2: Chemical structure of PTCDA

The goal of this project is to produce graphene nanoribbons. First, the anthracene polymer has to be synthesized. Second, the methods to preorganize polyanthracene on substrate surfaces have to be developed. Here, we tried to chemically synthesize polyanthracene first and then used electrochemical polymerization to improve the surface organization. The last step is to perform thermal consolidation and to analyze the structure and properties of the resulting thin film. Basic thermal pyrolysis was performed on polyanthracene prior to any further investigation, followed by iron chloride doping. Raman spectroscopy was applied to observe the polyanthracene's thermal behavior. Bulk experiments dealing with thicker polyanthracene films, followed by electro-polymerized thin film, were performed. XPS, AFM, and Raman spectroscopy were used to characterize the resulting films. Figure 3-3 is the schematic illustration of this project.

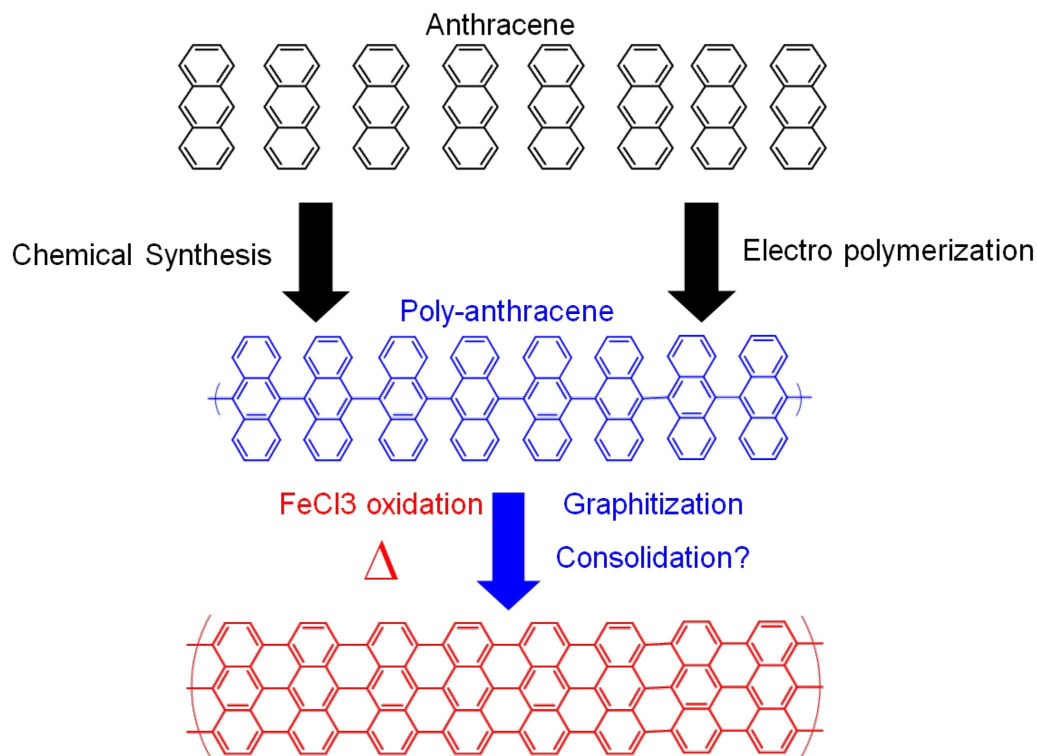

Figure 3-3: Schematic illustration of this project

3.2 Polymerization of Anthracene by Chemical Oxidation

It has been proven that cyclodehydrogenation occurs and polyanthracene is zipped up to form a graphene nanoribbon with the assistance of the gold surface.[11] The role of gold is not clear and the process, involving ultra high vacuum (UHV) evaporation, is costly and complicated. If anthracene can be polymerized in advance by simple chemical methods, the process of making graphene nanoribbons could be hugely improved. Actually, our idea of making graphene nanoribbons from polyanthracene arose before the publication of Mullen's anthracene evaporation work. We have tried to polymerize anthracene chemically, deposit it on the surface, study the pyrolysis results, and perform the iron chloride doping. First, polyanthracene was synthesized by Dr. Janusz Kowalik in Dr. Tolbert's lab. Details of the synthesis procedure will be published elsewhere. Briefly, anthracene was polymerized using iron chloride as an oxidant in nitrobenzene for four days. Figure 3-4 shows its reaction route.

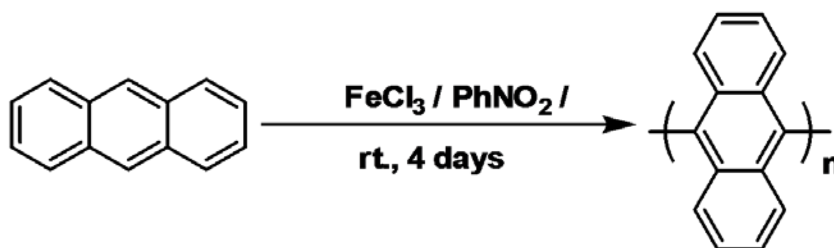

Figure 3-4: Polymerization of anthracene by chemical oxidation

Figure 3-5 is the MALDI spectrum of the polyanthracene product. The molecule weight of a single ahthracene unit in the polymer is 176. From the MALDI mass spec, it is clear that the fragments from two units ("2-imer"; 352) to nine units ("9-mer"; 1584) periodically show up at an exact frequency of 176. This indicates that anthracene was successfully polymerized to a chain with at least 9 units. One thing that should be noted is that the synthesized polyanthrcene is highly nonsoluble. A spectrum was taken from

the soluble fraction and a significant amount remained solid. The maximum nine repeating units here are not necessary reflecting the longest chain.

Besides the MALDI mass spec, a proton NMR was also employed to confirm the anthracene polymerization. The ^{1}H NMR spectra of the commercially available anthracene and 9,9'-Bianthracene were also taken for comparison with the polymerized product (figure 3-6). From anthracene to bianthracene, the presence of an additional quintet peak at around 7.1 ppm indicates the loss of symmetry and the dehydrogenation of the 9,9 position. From bianthracene to our product, the loss of the singlet proton (~8.75ppm in bianthracene, position 9) and the obvious shift in the quintet peak (position 1,8 of bianthracene) indicates that the bianthracenes link to each other at the 10,10 position, proving the polymerization.

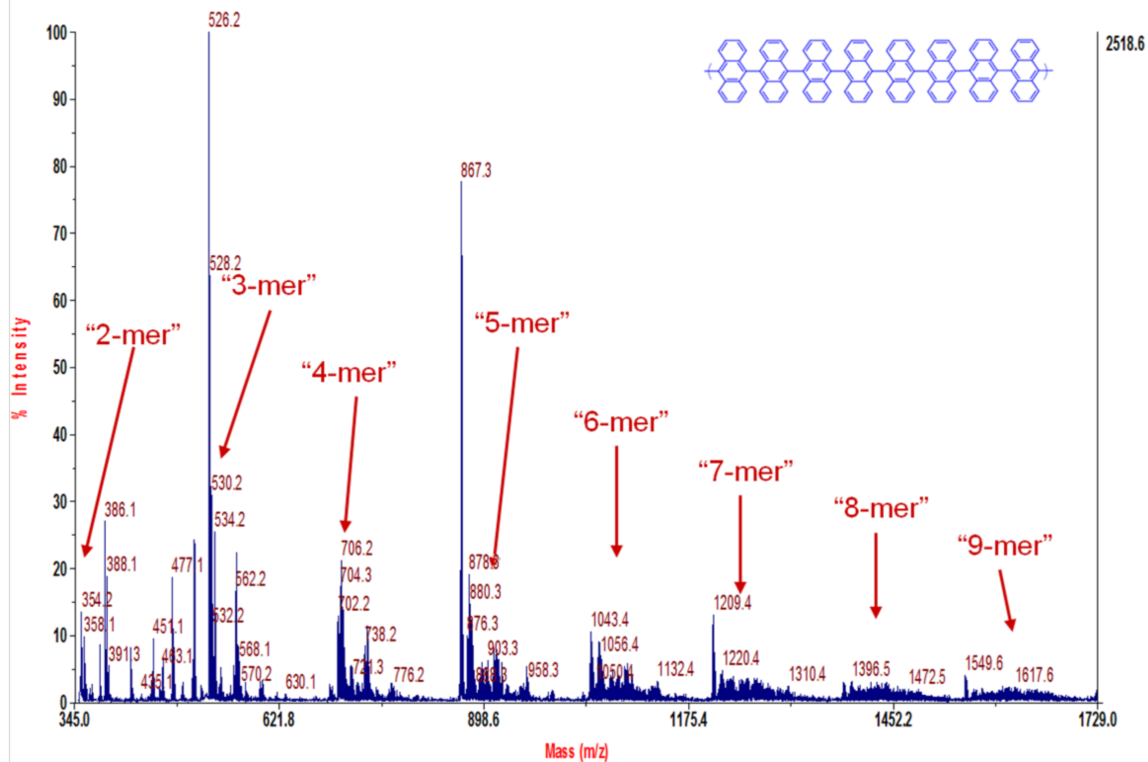

Figure 3-5: MALDI Spectrum of Polyanthracene

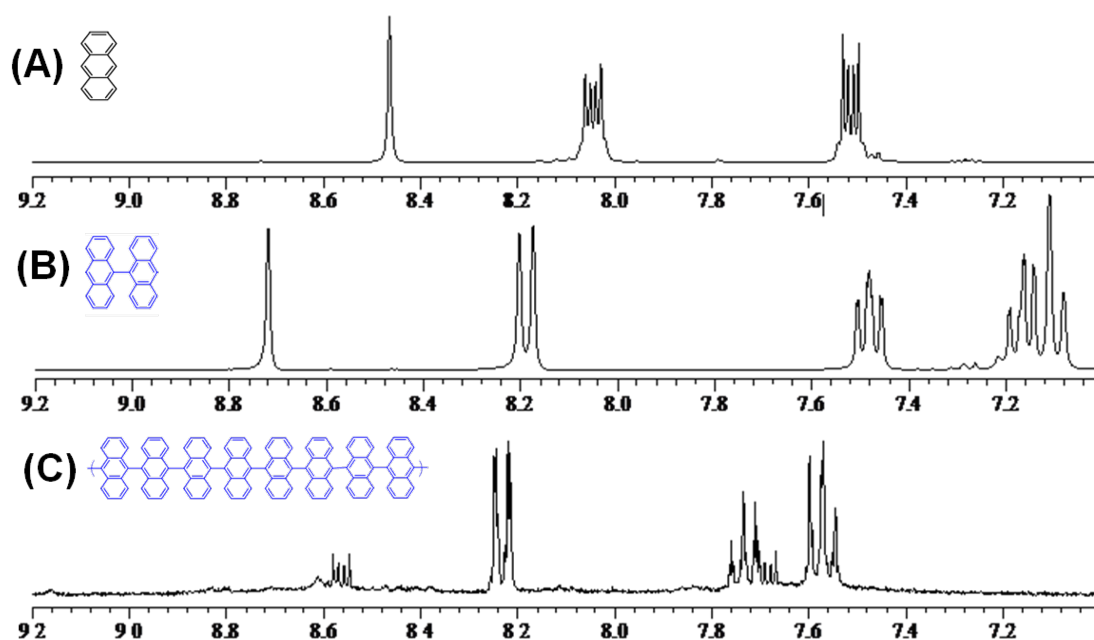

Figure 3-6: ^{1}H NMR spectra of: A, Anthracene; B, 9,9'-Bianthracene; C, Polyanthracene. Solvent: 1,1,2,2-Tetrachloroethane-d2. For C: spectrum taken for the soluble fraction. Significant amount remained solid.

Anthracene, bianthracene, and polyanthracene were then dissolved in THF and tested by a UV-Vis spectrum for comparison. Figure 3-7 shows the absorption and fluorescence spectra for the three of them. The trend of the shift from monomer, to dimer, to polymer can be clearly verified in both absorption and fluorescence. The emergence of three absorption peaks at higher than 300 nm is the feature of polyaromatic compounds. The redshift from anthracene to bianthracene matches with the theory that additional bonding on an aromatic ring will cause the absorption to shift to a higher wavelength. Therefore, the further shift of our product proves the polymerization.

Raman spectroscopy is also employed to verify the difference in Anthracene, bianthracene, and polyanthracene, and for the reference for comparing future graphitization as well. The laser wavelength for Raman is 488 nm. Again, from anthracene to bianthracene, the emergence of a C-C stretch between 1300 and 1400 cm^{-1} in addition to C-H, C=C is present, and an aromatic ring indicates the formation of

carbon-carbon bonding between anthracene. In polyanthracene, due to the random orientation of the polymer long chain, the details of C-C, C-H, C=C, and the aromatic rings are all embedded in a big amorphous carbon peak between 1300 and 1600 cm^{-1}.

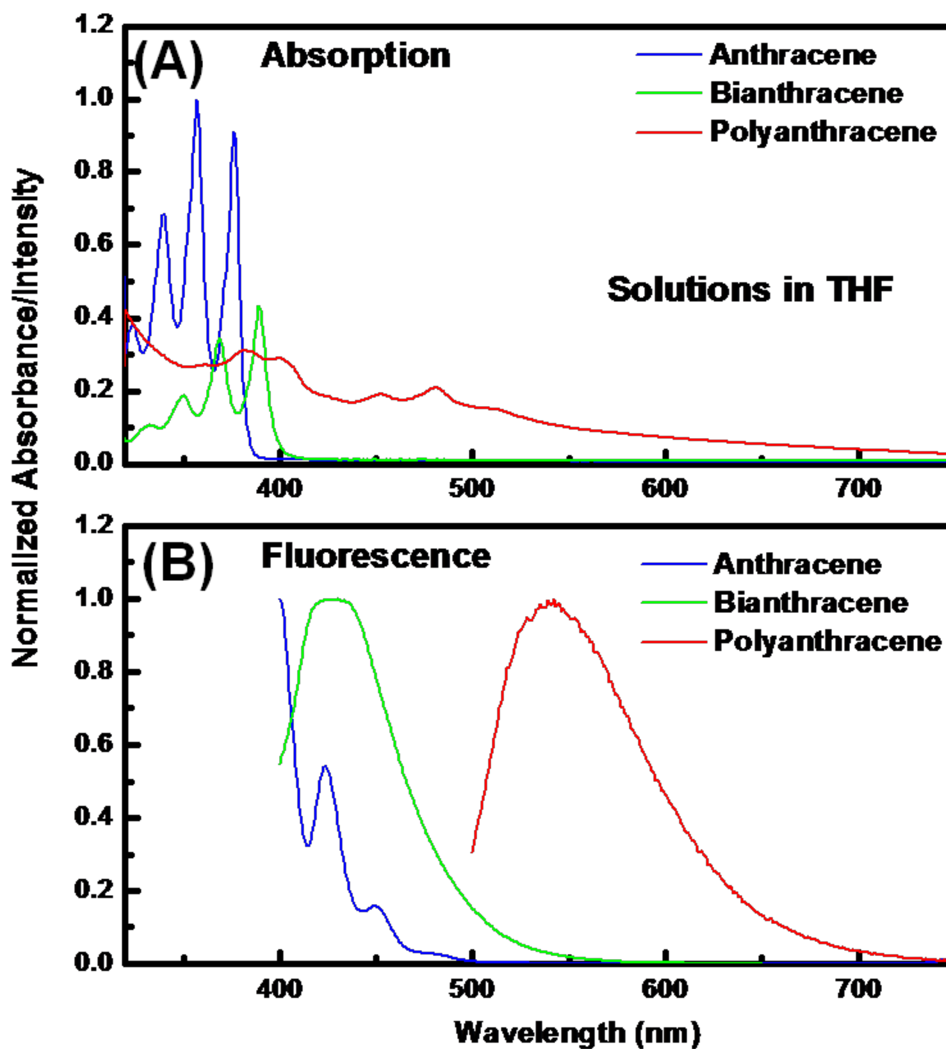

Figure 3-7: UV-Vis absorption and fluorescence spectra for Anthracene; 9,9'-Bianthracene; Polyanthracene.

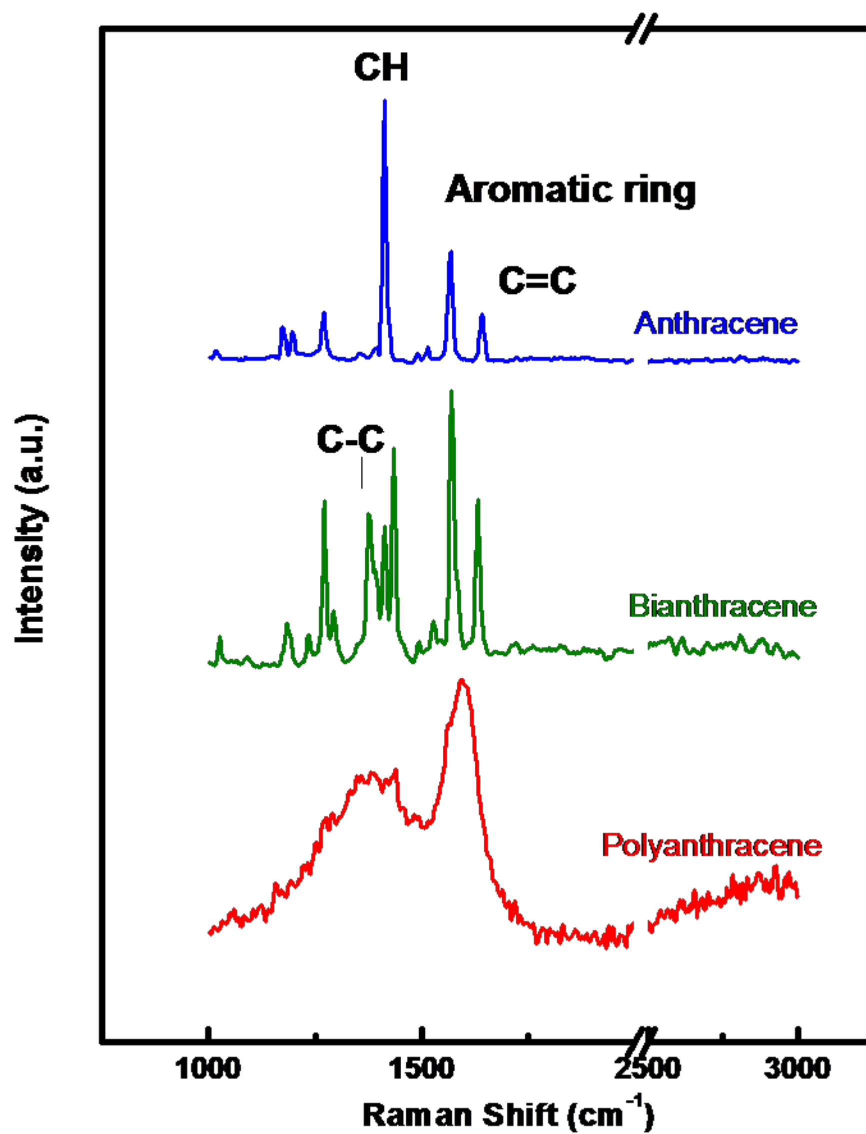

Figure 3-8: Raman spectra for Anthracene; 9,9'-Bianthracene; Polyanthracene.

3.3 Thermal Pyrolysis of Chemically Polymerized Polyanthracene

Once the polyanthracene has been successfully synthesized, the next step is to test if cyclodehydrogenation occurred under the normal thermal treatment. To do so, an excess amount of polyanthracene was first dissolved in THF and filtrated to make a saturated polyanthracene solution. The saturated concentration was way lower than 0.01 wt % due to the extremely low solubility of polyanthracene. Then, the polyanthracene-THF solution was applied on a silicon substrate by drop casting with heated substrate in order to instantly evaporate the solvent and thin out the film. Due to the low concentration, spin-coated polyanthracene only forms isolated islands instead of continuous film. The sample was then heated in a furnace under forming gas (4% hydrogen in argon) with a ramping rate of 50° C to 1000° C/min for 10 minutes. The fast ramping rate allows us to avoid potential oxidation problems in atmosphere. The sample is then cooled to room temperature inside the furnace with forming gas flowing. Figure 3-9 shows the Raman spectrum of the pyrolytic polyanthracene. It is obvious that the polymer still stays in an amorphous state even after 1000° C thermal treatment. There is no difference in Raman treatment compared to the reported pyrolysis result of anthracene-based cokes or saccharose-based chars.[17] This means that pure polyanthracene was heated as a carbon source. No consolidation or graphitization happened with the polyanthracene under this temperature. For pure polyanthracene, it can also be reasonably predicted that the 2-D band in the Raman (graphitization) will start to appear after a 2000 ° C thermal treatment due to the regular carbon graphitization process. However, it is still interesting that, in Mullen’s work, cyclodehydrogenation occurred at a low temperature (as low as 400° C) because of the gold surface assistance, implying that the consolidation of polyanthracene has to be assisted by some means.

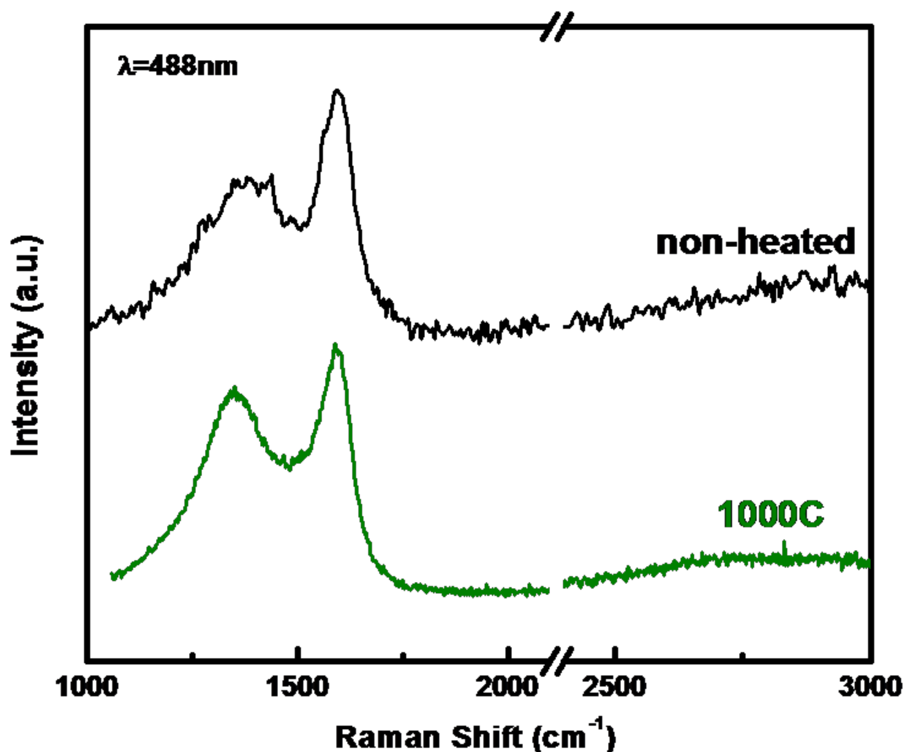

Figure 3-9: Raman spectra of as synthesized polyanthracene and polyanthracene after 1000° C thermal treatment in forming gas.

A route called oxidation dehydrogenation was tried as a way to consolidate the polyanthracene. After drop-casting, the polyanthracene film was immersed in an iron chloride-methanol solution for five seconds before processing it in the thermal treatment. Iron chloride is treated as an oxidant here to fully oxidize the carbon between the anthracene monomer units. The quick doping time here is done because the iron chloride is a strong oxidant and is done to avoid the re-dissolution of the casted polyanthracene film. Actually several solvents have been tested to improve the re-dissolution problem. It was found that methanol has the mildest dissolution of polyanthracene. However, a slight loss in the polyanthracene film still cannot be totally avoided. The iron chloride doped polyanthracene sample was then heated following the same procedure. Figure 3-10 shows

the optical microscopic images and the Raman spectra of the same sample. Amazingly, a strong 2D band emerges on some parts of the sample. In carbon materials, the appearance of a 2D band indicates a more ordered graphitic structure. In the mean time, the D band and G band become sharper due to the reduction of the amorphous carbon broad peak between 1300 and 1600 cm^{-1}. The same Raman result will only occur for carbon materials heated to over 2000° C . It seems that the preorganization of the anthracene and iron chloride oxidation hugely reduces the energy barrier for graphitization, but there are still some problems. First, the morphology of the resulting film is extremely bad; the film is cracked and is composed of several different layers and structures. This might be an intrinsic problem with using drop-casted film. Compared to spin-coating, drop-casted films always show a rough, thick, and non-uniform surface. Second, as shown in figure 3-10, the Raman result and surface morphology are both different. Some parts of the Raman sample show a graphitized structure with a large 2D band. However, some areas show a weaker 2D band while some areas are totally amorphous. Apparently, this is because of uneven doping or the re-dissolution of the polyanthracene. While performing iron chloride immersion, we did observe that some parts of the film were washed away by the iron chloride solution and those areas showed obvious different morphology and color after thermal treatment. Therefore, methods for sustaining the doping process and improving the film morphology have to be studied.

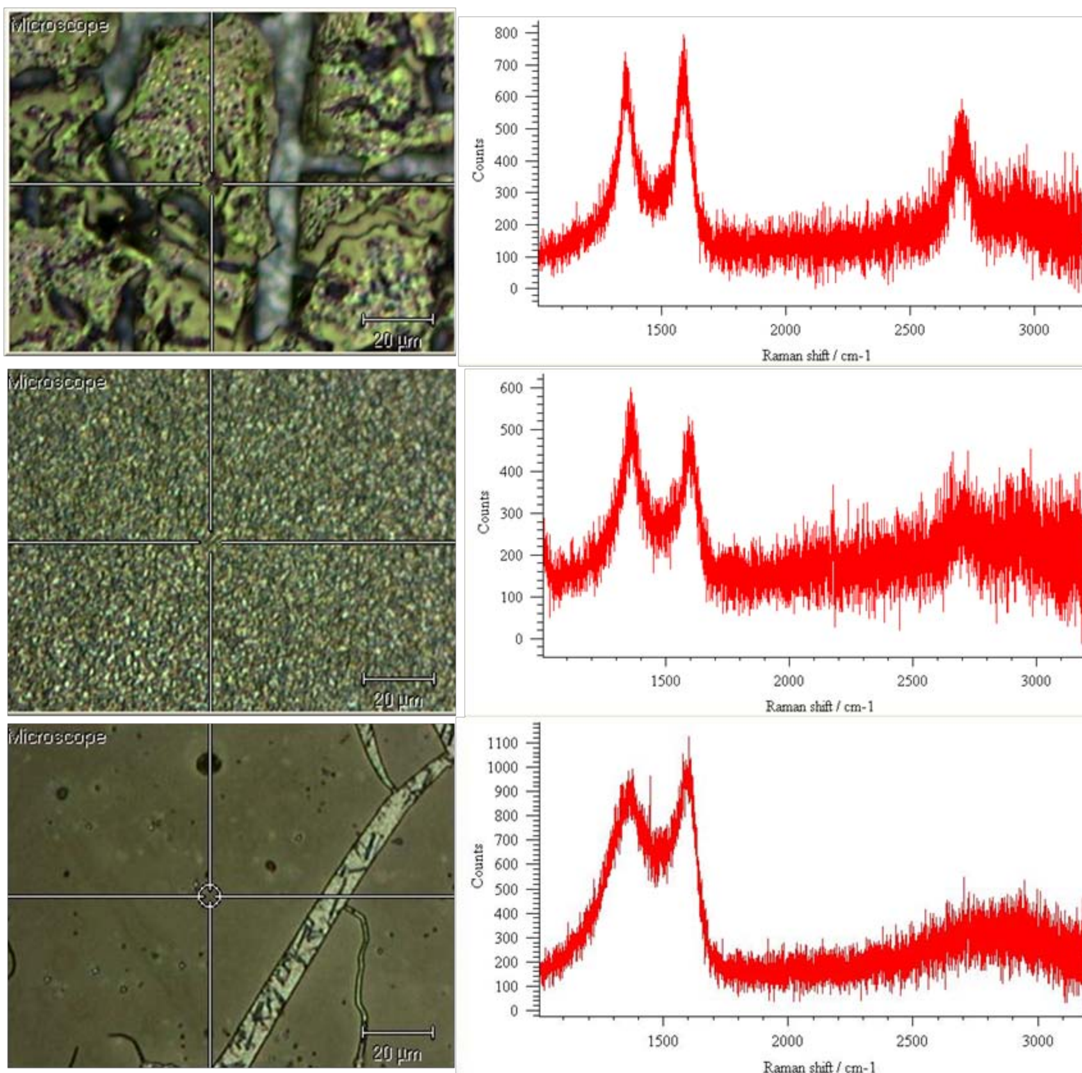

Figure 3-10: Optical microscopic images and Raman spectra on the same iron chloride doped sample after 1000° C thermal treatment. The cross target in the microscope is also the target for the Raman Laser.

3.4 Polymerization of Anthracene by Electrochemical Oxidation

Apparently, from the previous section, there are two basic problems in chemically synthesized polyanthracene even though the result is promising. First, limited by its intrinsic solubility problem, the solution deposited polyanthracene film cannot generate uniform morphology. Second, conversely, the drop-casted rough thick film cannot afford the immersion process of iron chloride doping. To solve these problems, a method which

can generate uniform, thin, and robust polyanthracene has to be applied. The electrooxidation method is a good candidate for the polymerization of anthracene because it has the capability to in-situ generate polymer thin film with controllable thickness. Most important of all, the polymerization of anthracene is also an oxidation process. Figure 3-11 is the reaction route for the electro polymerization of polyanthracene. The basic reaction is identical to that of the chemical oxidation. The only difference is that the oxidation process is changed from pure chemical oxidation to electro oxidation.

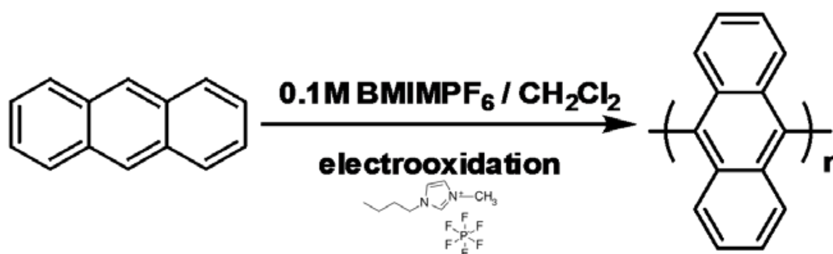

Figure 3-11: Polymerization of anthracene by electrochemical oxidation

A three-electrode cell was used to conduct the experiment, and the bias is provided by a potentiostat. In order to characterize the product, a transparent ITO electrode was first used for the absorption test. Dichloromethane was used as the solvent for anthracene. The electrolyte used was 1-Butyl-3-methylimidazolium hexafluorophosphate (BMIM PF6), and the reference cell is composed of silver/silver iodide with 0.1M tetrabutylammonium iodide (TBAI) in the dichloromethane. Figure 3-12(A) is the Cyclic Voltammetry of the anthracene when the ITO electrode is used for the electrooxidation. The change of loop with scans can be clearly seen and the polymer film is shown in the oxidized state. Figure 3-12(B) is the absorption spectrum of the polyanthracene polymerized on ITO. This also proves the growth of polymer. For the convenience of the following thermal treatment and Raman spectroscopy characterization, a 300 nm gold layer was evaporated with 30 nm chromium on the slicon wafer to be treated in the same way as the electrode. Figure 3-13 is the Cyclic Voltammetry of the

anthracene when the gold electrode is used for the electrooxidation. The growth of the polymer film can also be observed. The gold/chromium/silicon substrates were used in all of the following thermal treatment experiments in this report.

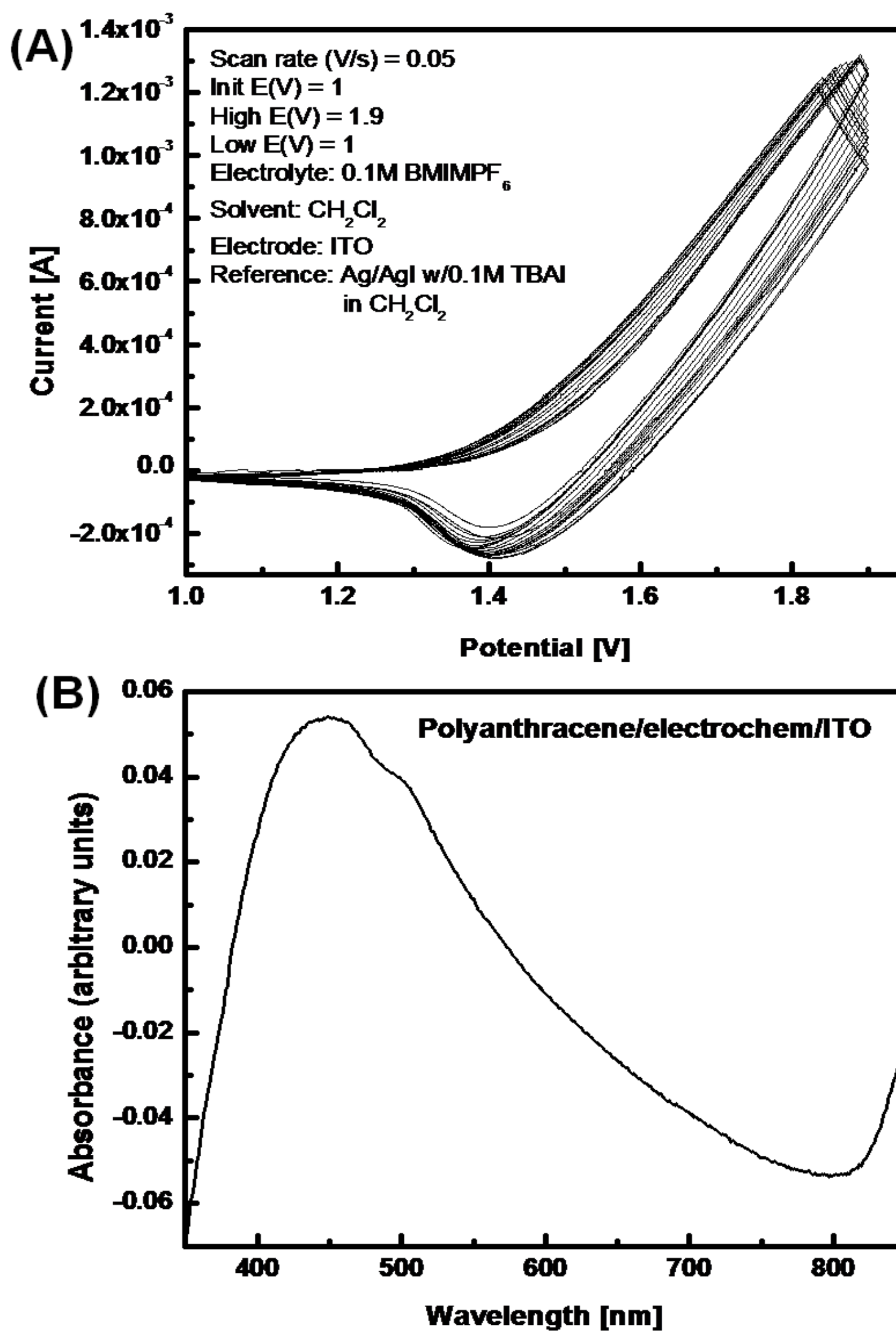

Figure 3-12: (A) Cyclic Voltammetry of anthracene when ITO electrode is used for the electrooxidation. (B) Absorption spectrum of polyanthracene polymerized on ITO.

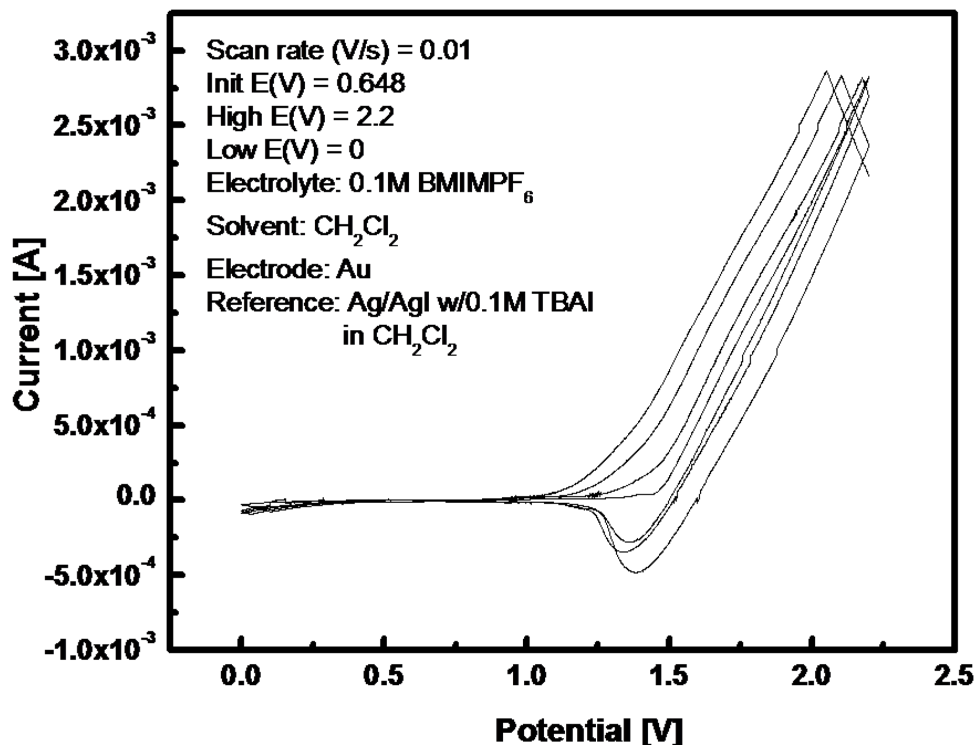

Figure 3-13: Cyclic Voltammetry of anthracene when gold electrode is used for the electrooxidation.

Figure 3-14(A) is the optical microscopic image of electrochemically polymerized polyanthracene. Obviously, the morphology of the film is much better than the drop-casting of chemically synthesized polyanthracene. Figure 3-14(B) is the Raman spectrum of the electrochemically polymerized polyanthracene; it also follows the basic structure of chemically synthesized anthracene. Typically, an amorphous carbon spectrum dominates the whole range. It should be noted that the substrate used here is gold, which might cause a minor difference in the chemically synthesized polyanthracene scanned on the silicon. To further explore the morphology of electro polymerized anthracene thin film, AFM is employed on the polyanthrcene/Au surface. From figure 3-15 it is clear that the film is continuous with minor bumps randomly distributed on the surface.

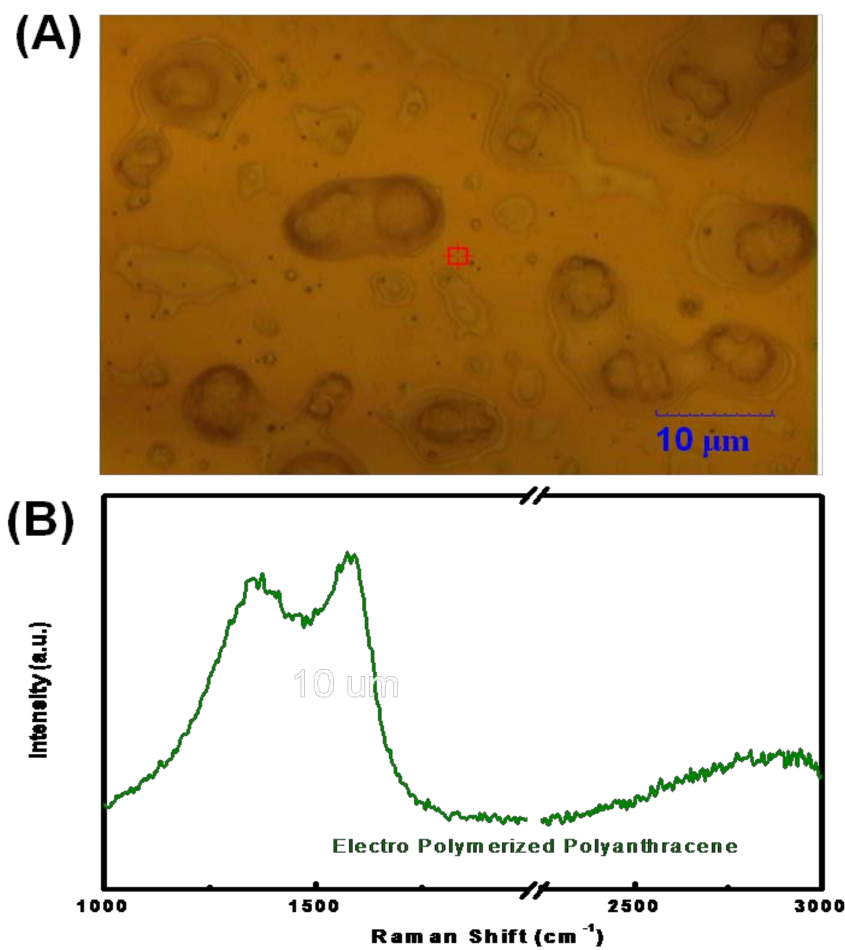

Figure 3-14: (A) Optical microscopic image of electrochemically polymerized polyanthracene. (B) Raman spectrum of electrochemically polymerized polyanthracene.

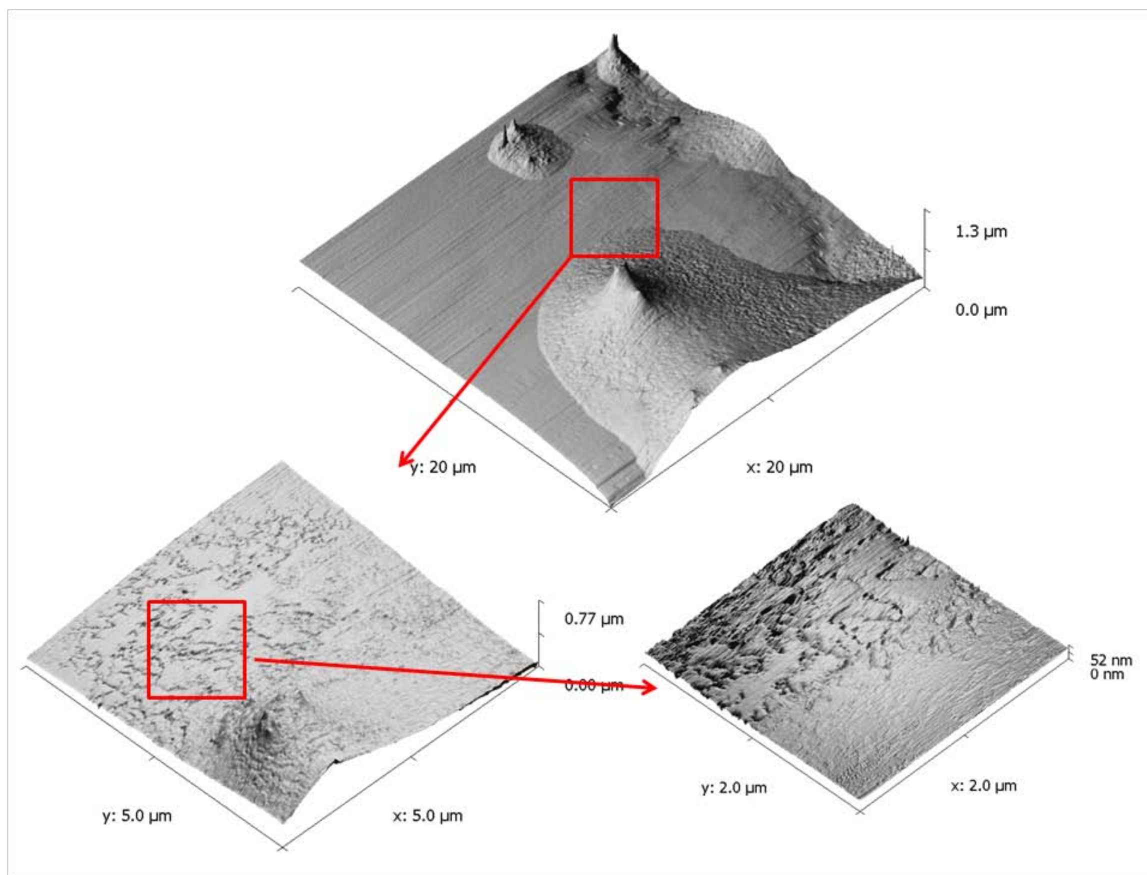

Figure 3-15: AFM images of electrochemically polymerized polyanthracene.

3.5 Thermal Pyrolysis of Electrochemically Polymerized Polyanthracene

The same iron chloride doping and thermal treatment process given above was performed to seek for a graphitization (or consolidation) effect equal to chemically synthesized polyanthracene. Figure 3-16 shows the the optical microscopic image and the Raman spectroscopy of the resulting surface. The major purpose for employing electrochemical polymerization is to generate more uniform and robust films. From the AFM of the as-synthesized film, it is sure that the film is continuous and flat. The only problem remaining was if the adhesion between the polymer film and the gold surface is strong enough to withstand the iron chloride immersion. It was found that the film is very tough in this mean and did keep intact even with a solvent wash. This is desired for the process because the doping is now guaranteed to be completed without damaging the film.

Furthermore, the excess iron or chloride ions can be washed away by the methanol rinse. After a 1000°C thermal treatment, the film was still intact and continuous.

The next question is if the polymer made through electrooxidation still follows the same pattern as a chemically synthesized one. After all, the graphitization was only a local phenomenon restricted in a small area. For the electropolymerized file, the Raman spectrum shows an even higher 2D band, indicating a higher degree of graphitization. Moreover, the same Raman spectrum appears everywhere on the film without any exception. This is a very promising result for the improvement of film quality by electropolymerization; however, from the AFM images in figure 3-17, lots of bumpy structures were randomly distributed on the film. High magnification scans showed that the whole surface is composed of small grain domains. The "bumps" area is a highly accumulated hill of small domains. The reason for the accumulation of small grains is not yet clear, but it is believed that those grains contain an ordered graphite structure and are the key for the emergence of the 2D band. If the size of the grains could be enlarged, i.e. reduce the numbers of the grain boundary, the Raman spectrum will tend to be more graphite like. Figure 3-18 is the comparison of the pyrolysis results of the chemically synthesized and the electro polymerized polyanthracene.

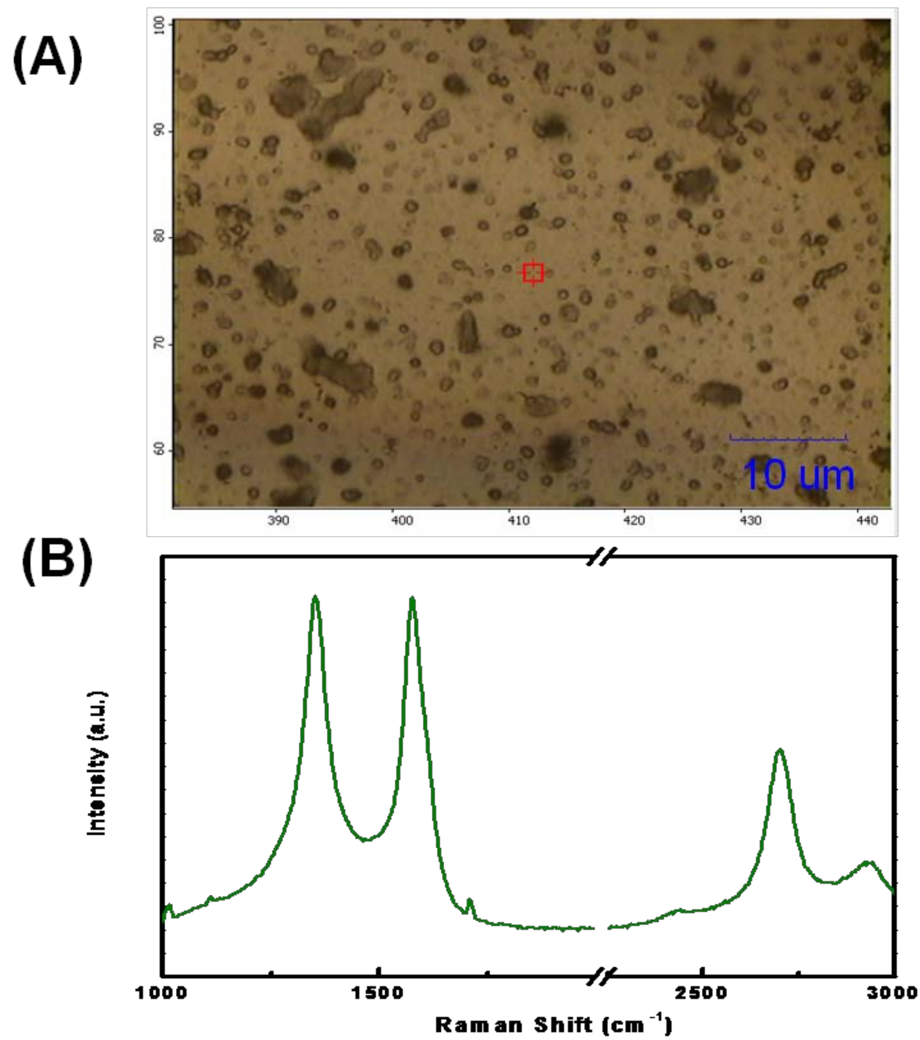

Figure 3-16: (A) Optical microscopic image of electrochemically polymerized polyanthracene after $FeCl_3$ doping and 1000°C thermal treatment. (B) Raman spectrum of electrochemically polymerized polyanthracene after $FeCl_3$ doping and 1000°C thermal treatment.

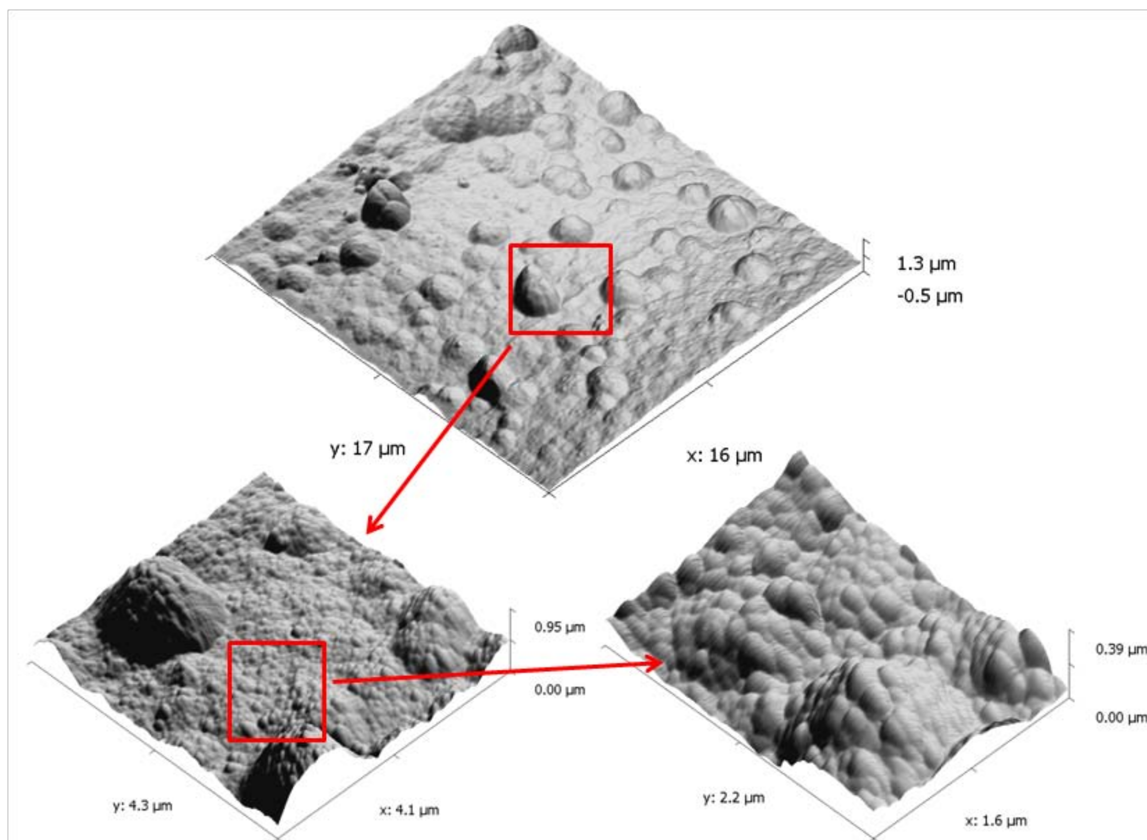

Figure 3-17: AFM images of electrochemically polymerized polyanthracene after iron chloride doping and 1000°C pyrolysis.

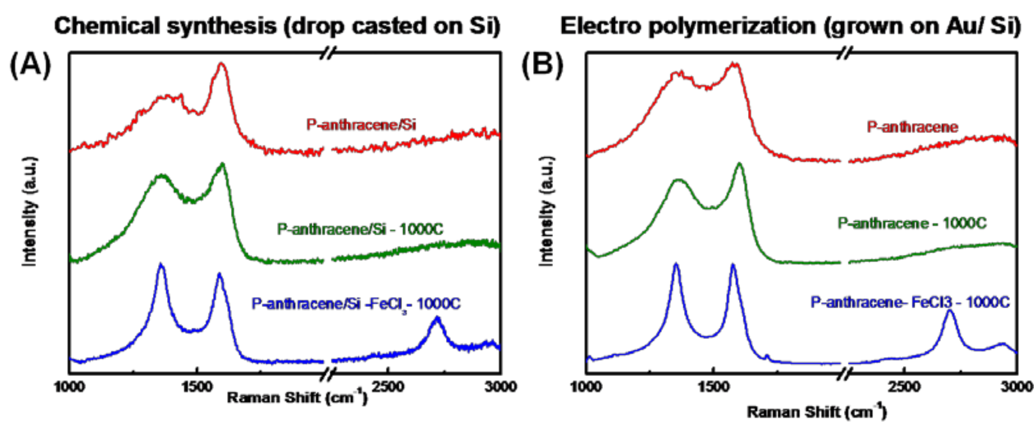

Figure 3-18: The comparison of pyrolysis results of (A) chemically synthesized polyanthracene and (B) electro polymerized polyanthracene.

To characterize the composition of electropolymerized polyanthracene, XPS was performed to probe both the as-synthesized polymer film and the thin film after pyrolysis. Figure 3-18 show the comparison between the two. In addition to carbon, silicon, and oxygen (SiO_2 substrate), the as-synthesized polyanthracene film contains fluorine, nitrogen, and phosphorous. They belong to the electrolyte BMIMPF6 remains. For the sample after iron chloride doping and thermal treatment, all impurities are gone and the result reveals that the film majorly consists of carbon. The appearance of oxygen is always a hint for oxidation in carbon, besides the surface's native oxide. High resolution scans of the carbon C1's region can provide further information on the detail bonding state of carbon. In figure 3-19, the deconvolution of C1's peak shows a minor C-O bond (286eV) and C=O bond (287.5eV), in addition to the SP3 and SP2 carbon-carbon structure at 284.5eV. Actually, these two peaks didn't appear on the as-synthesized electropolymerized film, indicating a slight oxidation during thermal treatment.

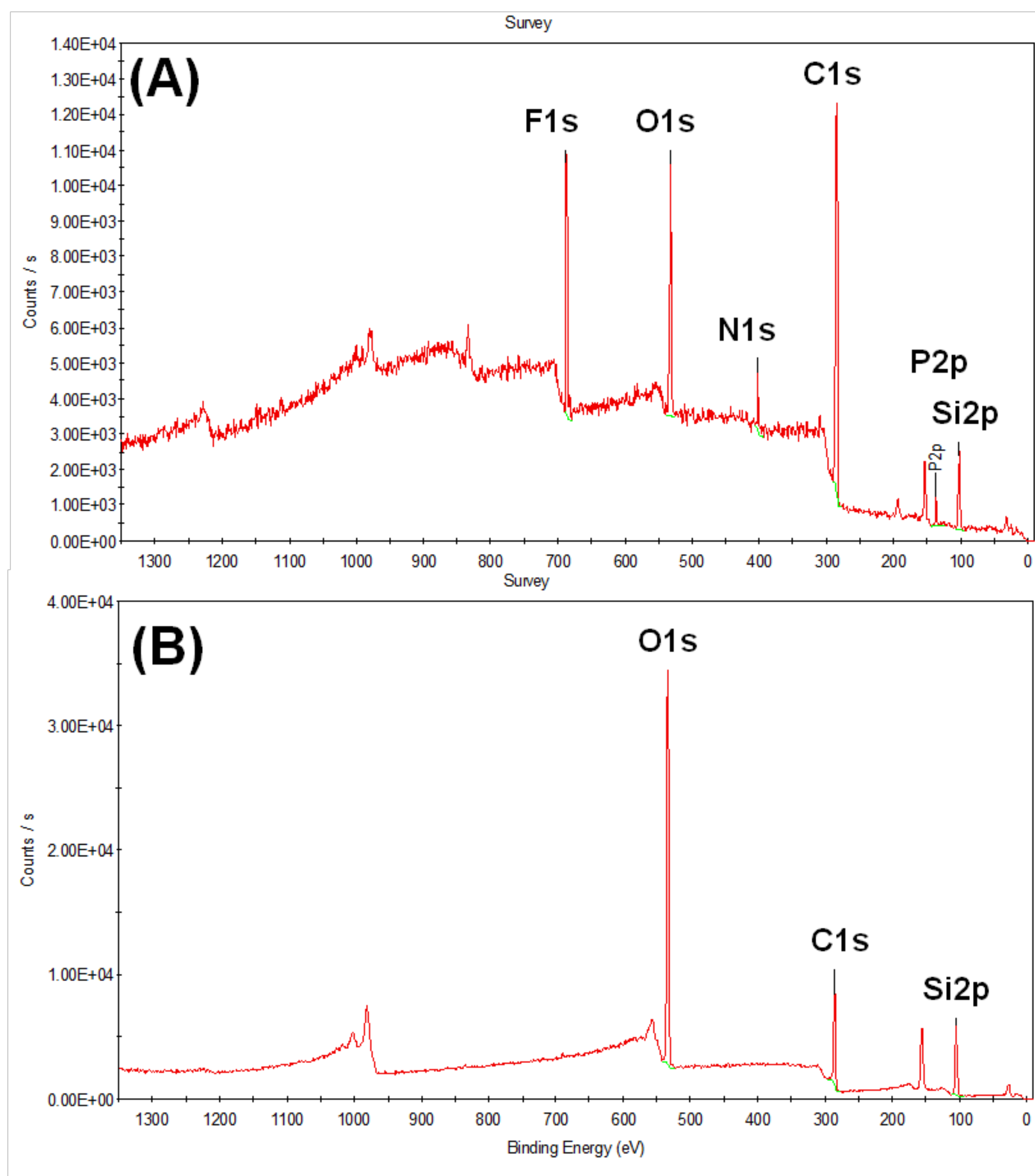

Figure 3-19: (A) A survey XPS scan for polyanthracene thin film made by electropolymerization. (B) A survey XPS scan for electropolymerized polyanthracene after iron chloride doping and 1000°C thermal treatment.

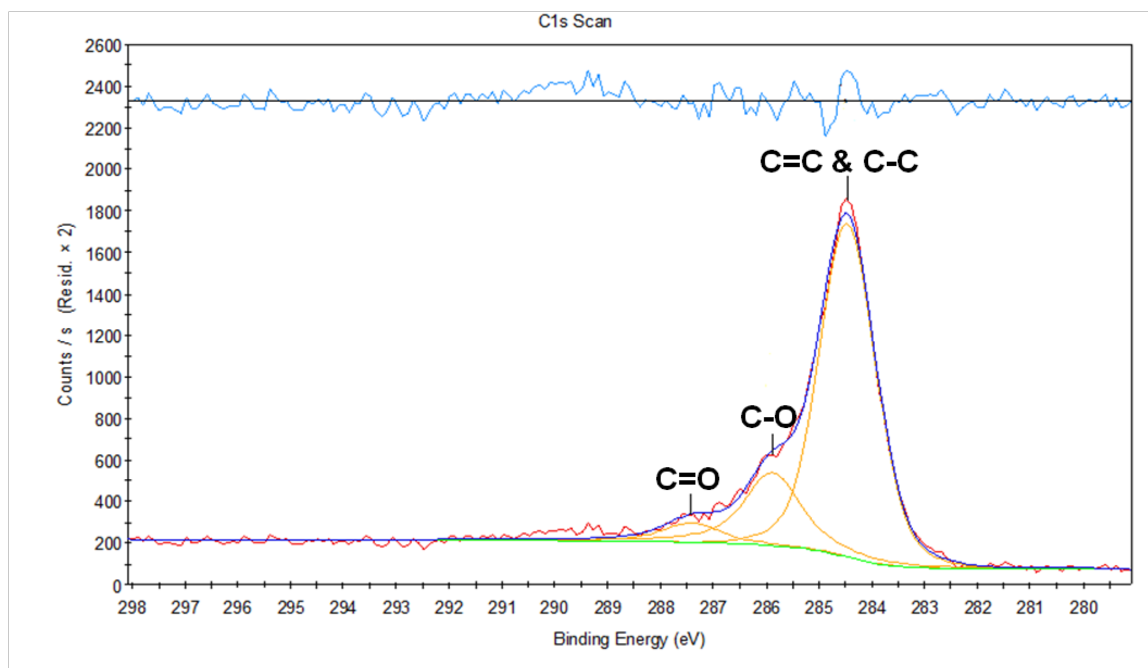

Figure 3-20: High resolution scan in carbon C1's region of electropolymerized polyanthracene after iron chloride doping and 1000°C thermal treatment.

Now the morphology and adhesion of the polyanthracene thin film has been hugely improved by the electropolymerization method. The resulting polymer also proved to graphitize at a lower temperature with the aid of iron chloride doping. However, graphitization involves a remarkable reorientation of the carbon materials, and the result should come from the low degree "melting" and "re-crystallization" of the polymer. In addition, the energy requirement is so high as a pyrolysis that a temperature of 2000° C is usually needed. Although we successfully decrease the energy barrier and lower the graphitization temperature to 1000° C with the pre-structure of polyanthracene, it is still out of our aim to perform a low temperature consolidation. As in the before mentioned work by Mullen's group, the consolidation of polyanthracene can be achieved at 400° C with the assistance of a gold surface, so it is reasonable to speculate that a similar cyclodehydrogenation route should occur at a lower temperature in our polyanthracene/Au/Si surface. Figure 3-20 show the Raman spectra of the iron chloride

doped electropolymerized polyanthracene thin film after pyrolyzing at different temperatures. Theoretically, as mentioned in Mullen's report,[26] besides the D and G peaks, several other peaks appear due to the finite width and low symmetry of the ribbons, including two peaks at 1220 and 1260 cm^{-1} which as assigned as defect bands. Our result shows that only graphitization occurs at 1000° C. While heated at 400° C, no significant change can be observed, compared to as-synthesized thin film. Actually, the only difference in our approach compared with Mullen's work is the use of the surface deposition method. In Mullen's work, a bianthracene precursor is evaporated on an Au(111) surface under UHV, followed by two steps of polymerization and consolidation. Therefore, even the polymer is forced into "lying-down" on the gold surface before the 400° C cyclodehydrogenation step. They also claimed that this "surface-assisted" step is a necessary condition for the consolidation. So it's a reasonable speculation for our approach that the film morphology grown on the electrode is still not in good control at this moment. Although it has been improved compared to solution deposition, the film thickness and polymer orientation still cannot satisfy the high demand of polyanthracene consolidation. Even though the same reaction happened at the polymer-gold interface, the random oriented polymer on top of it will block the Raman signal. Therefore, a thinner polymer film with some surface level growth is now in progress. Details will be addressed in the following chapter on recommendations for future work.

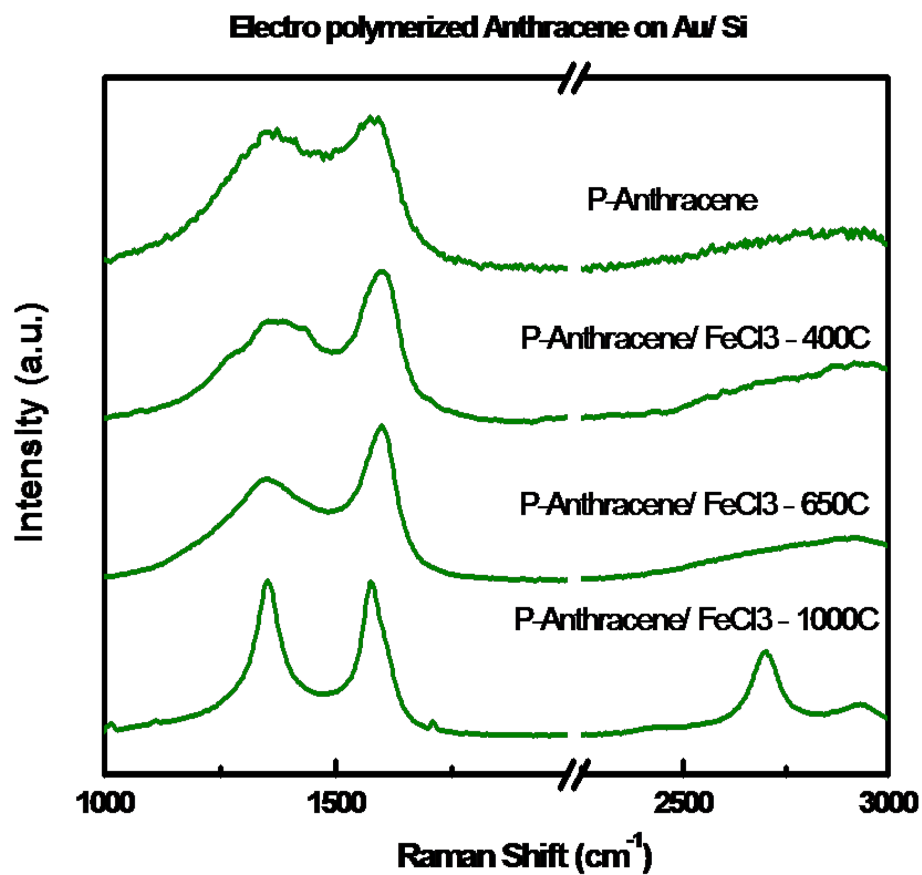

Figure 3-21: Raman spectra of iron chloride doped electropolymerized polyanthracene thin film after pyrolyzing at different temperature.

3.6 REFERENCES

1. Chen, Z. H.; Lin, Y. M.; Rooks, M. J.; Avouris, P., Graphene nano-ribbon electronics. *Physica E-Low-Dimensional Systems & Nanostructures* **2007,** *40* (2), 228-232.

2. Han, M. Y.; Ozyilmaz, B.; Zhang, Y. B.; Kim, P., Energy band-gap engineering of graphene nanoribbons. *Physical Review Letters* **2007,** *98* (20), -.

3. Li, X. L.; Wang, X. R.; Zhang, L.; Lee, S. W.; Dai, H. J., Chemically derived, ultrasmooth graphene nanoribbon semiconductors. *Science* **2008,** *319* (5867), 1229-1232.

4. Jiao, L. Y.; Zhang, L.; Wang, X. R.; Diankov, G.; Dai, H. J., Narrow graphene nanoribbons from carbon nanotubes. *Nature* **2009,** *458* (7240), 877-880.

5. Kosynkin, D. V.; Higginbotham, A. L.; Sinitskii, A.; Lomeda, J. R.; Dimiev, A.; Price, B. K.; Tour, J. M., Longitudinal unzipping of carbon nanotubes to form graphene nanoribbons. *Nature* **2009,** *458* (7240), 872-U5.

6. Elias, A. L.; Botello-Mendez, A. R.; Meneses-Rodriguez, D.; Gonzalez, V. J.; Ramirez-Gonzalez, D.; Ci, L.; Munoz-Sandoval, E.; Ajayan, P. M.; Terrones, H.; Terrones, M., Longitudinal Cutting of Pure and Doped Carbon Nanotubes to Form Graphitic Nanoribbons Using Metal Clusters as Nanoscalpels. *Nano Letters* **2010,** *10* (2), 366-372.

7. Jiao, L. Y.; Wang, X. R.; Diankov, G.; Wang, H. L.; Dai, H. J., Facile synthesis of high-quality graphene nanoribbons (vol 5, pg 321, 2010). *Nature Nanotechnology* **2011,** *6* (2), 132-132.

8. Wu, J. S.; Pisula, W.; Mullen, K., Graphenes as potential material for electronics. *Chemical Reviews* **2007,** *107* (3), 718-747.

9. Roberson, L. B.; Kowalik, J.; Tolbert, L. M.; Kloc, C.; Zeis, R.; Chi, X. L.; Fleming, R.; Wilkins, C., Pentacene disproportionation during sublimation for field-effect transistors. *J Am Chem Soc* **2005,** *127* (9), 3069-3075.

10. Laudise, R. A.; Kloc, C.; Simpkins, P. G.; Siegrist, T., Physical vapor growth of organic semiconductors. *Journal of Crystal Growth* **1998,** *187* (3-4), 449-454.

11. Cai, J. M.; Ruffieux, P.; Jaafar, R.; Bieri, M.; Braun, T.; Blankenburg, S.; Muoth, M.; Seitsonen, A. P.; Saleh, M.; Feng, X. L.; Mullen, K.; Fasel, R., Atomically precise bottom-up fabrication of graphene nanoribbons. *Nature* **2010,** *466* (7305), 470-473.

12. Gherghel, L.; Kubel, C.; Lieser, G.; Rader, H. J.; Mullen, K., Pyrolysis in the mesophase: A chemist's approach toward preparing carbon nano- and microparticles. *J Am Chem Soc* **2002,** *124* (44), 13130-13138.

13. Kolodziej, J. J.; Goryl, M.; Konior, J.; Krok, F.; Szymonski, M., PTCDA molecules on an InSb(001) surface studied with atomic force microscopy. *Nanotechnology* **2007,** *18* (13), -.

14. Vaurette, F.; Nys, J. P.; Grandidier, B.; Priester, C.; Stievenard, D., Growth mechanism of organic nanocrystals on passivated semiconductor surfaces. *Physical Review B* **2007,** *75* (23), -.

15. Chen, W.; Huang, H.; Chen, S.; Gao, X. Y.; Wee, A. T. S., Low-temperature scanning tunneling microscopy and near-edge X-ray absorption fine structure investigations of molecular orientation of copper(II) phthalocyanine thin films at organic heterojunction interfaces. *J Phys Chem C* **2008,** *112* (13), 5036-5042.

16. Chen, W.; Huang, H.; Chen, S.; Chen, L.; Zhang, H. L.; Gao, X. Y.; Wee, A. T. S., Molecular orientation of 3,4,9,10-perylene-tetracarboxylic-dianhydride thin films at organic heterojunction interfaces. *Applied Physics Letters* **2007,** *91* (11), -.

17. Bernard, S.; Beyssac, O.; Benzerara, K.; Findling, N.; Tzvetkov, G.; Brown, G. E., XANES, Raman and XRD study of anthracene-based cokes and saccharose-based chars submitted to high-temperature pyrolysis. *Carbon* **2010,** *48* (9), 2506-2516.

CHAPTER 4

HIGHLY REACTIVE 3-AMINOPROPYLTRIETHOXYSILANE MONOLAYER DEPOSITED BY VAPOR SILANIZATION AND SELF-ASSEMBLY OF CONTINUOUS GRAPHENE OXIDE FILM

Gas-phase silanization has multiple advantages, such as having a controllable temperature and low molecular concentration and being solvent-free. However, the exact reaction condition and product performance are still not clear. A flow type vacuum reactor equipped with an evaporator and carrier gas flow system was built to perform the vapor-silanization of 3-Aminopropyltriethoxysilane (APTES). Surface analytical techniques such as X-ray photoemission spectroscopy (XPS), atomic force microscopy (AFM), and spectroscopic ellipsometry have been employed to characterize the resulting films. We altered the APTES vapor concentration, reaction time, and reaction temperature to seek the high quality APTES monolayer. Similar to liquid-phase silanization, the increasing of APTES vapor concentration will dramatically reduce the free amine content and result in an extremely rough film. At a low reaction temperature (110°C), the free amine content of the resulting APTES film has no way to compete with liquid-silanization. It was found that vapor-silanization performed under 150°C can generate an APTES layer with high free amine content (93.74%) and that is uniform in morphology. We also examine the performance of vapor-silanized APTES layers through the immobilization of GO and AuNPs. In an optimized condition, a continuous GO thin film can be deposited on an APTES layer in 10 minutes by the self-assembly of the GO flakes. Similarly, highly dense AuNPs arrays can also be immobilized on the surface. Moreover, a patterned GO thin film was generated by the vapor-silanization of APTES, the self-assembly of GO flakes, and the lift-off.

4.1 Introduction

Alkylsilanes terminated with various functional groups have been widely used to react with hydroxylated surfaces, such as silicon with native oxide, porous silica, glass, and metal oxides, in order to modify its physical or chemical properties. For example, a silicon surface modified with fluorinated silane could have a highly increased hydrophobicity, and thio-terminated silane could be treated as the linker between gold and silicon. Based on the multiple functions of the amino group, a aminosilane modified silicon surface carries a variety of capabilities including: the immobilization of protein,[1] DNA,[2] and biomolecules;[3-5] the fabrication of the metal ion sensor;[6] promotion of adhesion;[7] and electrostatic assembly of inorganic nanoparticles[8, 9] or, most recently, graphene oxide.[10] The performance of such self-assembled aminosilanes has to be examined by two factors, i.e., the chemical state of the surface amino group and the physical morphology of the deposited molecular films. It is well known that amine is easily protonated or hydrogen bonded; therefore, it's crucial to have a high content of primary-amine moieties exposed on the surface to serve as activated sites that will react with the target compound or generate surface charge. In some applications, such as in the immobilization of graphene oxide and DNA, a rough surface or aggregation could dominate the atomic force microscopy image and increase the difficulty of observation. While used in the field of microelectromechanical systems (MEMS), aggregations may interfere with the operation of the device, so homogeneity in surface morphology is also highly desired.

Conventionally, the silanization of self-assembly monolayers (SAMs) is performed in the liquid phase. The self-assembly of 3-Aminopropyltriethoxysilane (APTES) is even more complicated, often resulting in multilayer deposition and irregular surface morphology.[11] In the early stage of the development of the silanization process, the physical morphology (monolayer, multilayer, and aggregation) of the aminosilane film attracts more attention. Many reports, which discussed the effects of the solvent,

concentration, and water content, etc., have been issued. For the selection of the solvent, different types of solvent might result in a change in the density of the deposited film.[12] Then, it was found that water plays an important role in all non-aqueous based silanization processes.[13, 14] Water is indeed needed to hydrolyze alkoxyl groups, but too much water will lead to the rapid polymerization of aminosilane before it has the chance to react with the surface hydroxyl group. These polymerized products result in a multilayer network and hugely decrease reactivity and reproducibility. Furthermore, the sensitivity of water is enhanced for amino silanes because the amino group self-catalyzes the formation of siloxane.[15] The amine functionalities also compete with the alkoxy moieties on surface hydroxyl sites. Monolayers of APTES are oriented with free amine groups away from the surface and with hydrogen-bonded and protonate amines faced to the surface where they bind with the silicon oxide.[16] Therefore, the number of protonated amines and hydrolyzed ethoxy groups is related to the amount of water at the interface. It was also found that post-silanization curing can effectively increase the quality of APTES films. A mild curing at around 100 to 150° C can increase the number of siloxane bonds.[17] Actually APTES only bonds with one or two siloxane bonds at the surface after silanization. With the additional curing, the silanes condense very rapidly to siloxanes, and it helps to fully bond the three docking legs to the surface.[18, 19] Vandenberg et al. studied the kinetics of APTES liquid silanization and depicted that APTES first adsorbs to the silicon noncovalently. Mild curing results in the covalent bonding of the first one or two monolayers at the surface. The remaining physical adsorbed or partially polymerized APTES can be easily washed away.[16]

4.2 Background

The elimination of both polymerization and amine hydrogen-bonding requires a means of excluding trace quantities of water. Even under a strict control of water content

in solvent (using dry solvent) and reagent purity, an unavoidable thin water film adsorbed on the surface at room temperature can still ruin the reaction. In many cases, lack of control over these issues in the liquid phase reaction produces APTES films with irregularities in their morphologies and poor reactivity. It's particularly a drawback when APTES layers are employed to micron or nano-sized technological applications. In addition, the solution-phase approach is neither industrially viable nor environmentally friendly due to the significant amount of solvent that is generated. Therefore, the low reproducibility and the high cost associated with liquid silanization limit its application, especially in the research level.

An alternative method to overcome this problem is to deposit APTES in gas phase. The use of gas-phase reaction allows for higher reaction temperatures than could be tolerated in liquid-phase reactions. Two benefits can be gained by the high temperature. First, as one can expect, a higher temperature can effectively reduce the amount of water that is adsorbed on the surface. Second, a higher temperature has been proved to promote siloxane bonding.[17] Compared to liquid-phase deposition, there have been relatively few reports of the gas-phase silanization of APTES. The effects of reaction temperature and APTES vapor concentration have not yet been systematically studied. Haller et al. first demonstrated the use of a vapor of 5wt% solution of APTES in toluene to vapor-silanize silicon wafers.[20] Substrates were placed face down and the solution was heated and refluxed in the same chamber. A result of a well-defined APTES layer was obtained, and reactions of the amino groups allowed the bonding of a variety of organic molecules to the surface. Similar approaches have been used with a minor modification. Hozumi et al.[21] and Song et al.[22] sealed substrates and aminosilane-toluene solution in the same chamber and heated them together in a 100° C oven. Asenath et al. used pure liquid silane as a precursor, sealed it in a vessel along with substrates and heated it to 70° C.[23] Although these types of single chamber evaporation have the advantage of easy operation, the precursor vapor concentration is unsteady and not controllable. In addition, the

reaction temperature is forced to be equal to the evaporation temperature. As a matter of fact, the free amine ratio of these studies is either low or unclear. Fiorilli et al. performed vapor-phase silanization at low pressure and 80° C.[24] Their procedure reduced, but did not eliminate, surface aggregation; a large portion of hydrogen-bonded amine could still be found. Zhang et al. used a chemical vapor deposition (CVD) system to perform the vapor silanization.[25] A precise volume of silane was vaporized in temperature-controlled flasks and introduced in batches through heated pipes to the main vacuum chamber at 150 ° C. The results showed monolayer thickness with low surface roughness. Ek et al. applied an atomic layer deposition (ALD) type reaction at 150° C, i.e., alternatively introduced silane vapor and water vapor.[26] The result showed an improved nitrogen atom density, but again, the potential hydrogen-bonding effect resulting from additional water is not discussed. In summary, a wide range of reaction temperatures, from room temperature to 150° C, and unsteady vapor concentrations have been applied in the vapor-phase silanization of APTES. Although good results could be obtained in surface morphology and silane conformation, the chemical reactivity resulting from the high free amine ratio has yet to be studied.

The first aim of this study was to verify the effect of vapor concentration, growth time, and reaction temperature in the vapor-phase silanization of APTES. To reach this goal, a flow type vacuum reactor equipped with a saturator/carrier gas flow system was used to precisely control the APTES vapor concentration and the independent substrate and saturator temperature. Under the conditions of a fixed carrier gas flow rate and saturator temperature, the APTES vapor concentration was controlled by tuning the outlet flow rate of the saturator. The performance of the deposited APTES monolayers was decided by surface morphology and reactivity. Atomic force microscopy (AFM) was used to probe the surface topography, while ellipsometry was used to confirm the film thickness. In addition, the nitrogen/silicon ratio obtained from X-ray photoemission

spectroscopy (XPS) can provide direct quantified data for the APTES surface coverage rate. For surface reactivity, the free amine ratio, determined by high resolution N_{1s} scans through XPS, was treated as an indicator for surface charge potential. Instead of measuring nitrogen atom density, the deconvolution of the nitrogen N_{1s} binding energy can further clarify the state of amine, e.g., primary amine, hydrogen bonded amine, protonated amine, etc. When immersed in aqueous solution, only free primary amine (-NH_2), which still contain a lone pair, affords to bond to the additional hydrogen in the water, forming $–NH_3+$. The surface potential, resulting from the positively charged –NH_3+ moiety, decided the capability of charge transfer between the APTES layer and the attracted subject. Therefore, the reactivity of the APTES modified surface should be determined by the ratio of free amines. The second aim is to graft highly dense gold nanoparticles (AuNPs) and continuous graphene oxide (GO) film from AuNPs and GO flakes colloid, respectively, onto super attractive APTES monolayers deposited by the optimized vapor-phase silanization process. We want to prove that fully covered, or even stacked, GO thin film could be self-assembled on high quality APTES monolayers.

4.3 Experimental

Materials. 3-Aminopropyltriethoxysilane (APTES; 99% Aldrich) and dry toluene (anhydrous; 99.8%; Aldrich) were purchased from Aldrich without any further purification. Gold nanoparticles (AuNPs) were purchased from Ted Pella (10nm Unconjugated Gold Sols). Graphite oxide was synthesized from natural graphite through the modified Hummers method as originally presented by Kovtyukhova and colleagues.[27, 28] GO solutions with different concentrations were prepared by dispersing synthesized GO powder in DI water, followed by a two-step sonication. In this experiment, we prepared the GO solution for 0.05mg/ml. First, a mild bath sonication was introduced for 10 minutes to roughly disperse the GO powder (Branson model 5510). At this step, the

GO suspension can be clearly seen and the particle size cannot be further reduced. Therefore, a second-stage dispersion was performed by horn sonication for 1 minute (750W, sonics & materials VCX750), which effectively breaks the GO flakes into small pieces. The solution is now well dispersed and suspension particles are no longer visible. Because GO powder is highly acidic, to stabilize GO flakes, the pH of the prepared GO solution was adjusted to around 8 using 1% ammonia. Then, the solution was centrifuged at 14,000 RPM for 10 minutes to remove big aggregation.

Vapor-silanization system The Vapor-silanization system consists of a 6 way 2.75 inch conflate cross as a reactor chamber that is connected to a vacuum pump, vapor delivery system, pressure gauge, and sample stage. The vapor delivery system is composed of a glass reservoir (saturator) connected by a metering valve to a stainless steel pipeline that allows silane vapor to merge with carrier gas before entering the reactor chamber. Both the delivery frame and the reactor are wrapped by heating tapes to avoid the condensation of silane vapor. A cartridge heater (Omega, CSH series) and a K-type thermocouple (Omega) are built in with a sample stage to heat the substrate and monitor its temperature. A liquid nitrogen trap is installed at the downstream of the reactor to protect the vacuum pump.

Substrate preparation and vapor-silanization of APTES Highly doped n-type (100) silicon wafers bearing 300 nm thermally grown oxide were used as substrates. A 10-min oxygen plasma treatment (Harrick PDC-32G plasma cleaner/sterilizer with air as the source gas and a base pressure of 0.4 torr) was used to fully hydroxylate the surface. To obtain the best APTES quality, vapor silanization was performed using the following procedure: Briefly, the sample was put into the reaction chamber and heated to the desired temperature. The evaporator (saturator) system was first isolated and heated to 110˚C to vaporize the APTES. In the mean time, a 80 sccm nitrogen carrier gas flow was introduced into the chamber and the chamber pressure was fixed at 1 torr with flowing nitrogen by controlling the pumping valve. The metering valve of the evaporator was

then opened to a different flow rate for the desired period of time (the meter valve was calibrated in advance). After the reaction, the sample was rinsed with a copious amount of DI water and blown dry.

Characterization of APTES film (AFM, XPS, and Ellipsometry) The topography of the APTES surface was investigated using tapping-mode AFM (Agilent 5500, picoplus system). The probes used for this study had a spring constant of 40N/m and a tip curvature less than 10 nm. The composition of nitrogen bonding in APTES was probed by X-ray photoelectron spectroscopy (XPS, Thermo-K Alpha). Al K α X-ray radiation was used as the X-ray excitation source and the beam size was set to 400μm. The power was set to 150W and the voltage to 20eV for high resolution scanning. The fitted peaks of the XPS spectra were determined by a combination of Gaussion and Lorentzian distributions. The thickness of the APTES films was measured by an M-2000 Variable Angle Spectroscopic Ellipsometer (VASE, J.A. Woollam). Ellipsometry data was collected over a wavelength range from 400 to 1000 nm at angles of 65°, 70°, and 75° (with respect to the substrate plane as normal). Data was analyzed and fit to determine the film thickness and the refractive index by employing a Cauchy model for the films and using stacked layers, including APTES, SiO_2, and Si. To precisely extract the APTES thickness, the thickness of SiO_2 was measured prior to the vapor-silanization. The scanning electron microscope (SEM) used was the Zeiss ULTRA 60.

Deposition of GO film and AuNPs For the self-assembly of GO and AuNPs, samples after vapor-silanization were immersed in a 0.05mg/ml GO solution or commercial AuNPs solution for the desired period of time, followed by a DI water rinse.

4.4 Results and Discussion

In the wide spectrum of silane application, it is well known that the silanization rate could be controlled by the surface docking group. For example, trichloro-silane

typically has the fastest reaction rate, followed by methoxy-silane, then ethoxy-silane. Changing different types of docking groups creates a compromise between the silanization rate and film quality. A higher silanization rate means a higher hydrolysis rate, and surface morphology tends to develop three-dimensionally instead of as a homogeneous monolayer structure; this same theory applies to aminosilane. In addition to concerns about the morphology, surface reactivity is also affected by the hydrolysis rate because the amine moiety also forms hydrogen-bonding with the hydrolyzed hydroxyl group. Therefore, the control of silanization for 3-aminopropyltrimethoxysilane (APTMS) is more crucial than for APTES,[25] not to mention for in gas-phase silanization.[22] Conversely, the liquid-phase silanization of APTES has a much wider tolerance for reaction conditions, ranging from 1%/10 min to 0.07% (3mM)/5 hrs.[25, 29, 30] A highly reactive APTES surface (with a high free amine ratio) could be easily obtained within that range, while the resulting surface morphology is still not easy to control. Figure 4-1 shows the high resolution XPS spectrum of the N_{1s} region for a APTES silanized silicon surface deposited by liquid-phase silanization and its AFM topography. The solvent chosen here is dry toluene, and a diluted concentration with a reduced reaction time (3mM / 3 hrs) is chosen to enhance the monolayer's deposition. A scan for bare silicon is also shown for comparison. The N_{1s} peak can be deconvoluted into two peaks: 398.7 eV for a free amine and 400.7 eV for a hydrogen-bonded amine. It is clear that liquid-silanization under this condition generates a surface with a high free amine ratio (84.25%). However, due to the unavoidable trace amount of water adsorbed on the surface, the AFM image shows an unevenly grown 3-D structure.

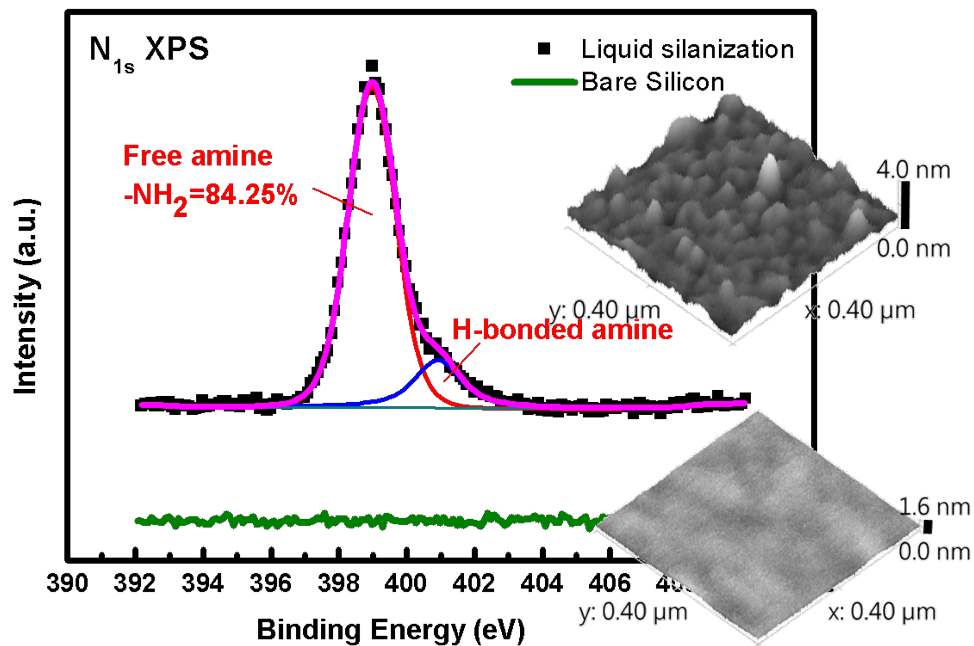

Figure 4-1: High resolution XPS spectra of N_{1s} region for APTES silanized silicon surface deposited by liquid-phase silanization (dry toluene; 3mM/3hrs) and a control scan on bare silicon substrate. Insets are the tapping mode AFM topography images for both samples.

Similar to ALD, gas-phase reaction could further reduce the precursor concentration while elevating the reaction temperature being limited to boiling point in a solvent mediated reaction. Such a reaction, with a low concentration and a high silanization rate, makes the deposition to be diffusion-controlled, which benefits monolayer formation. Therefore, the effect of the silane vapor concentration and its interaction with growth time was tested first to catch the preliminary conditions. The reaction temperature was initially set to be equal to the evaporator temperature (110°C) simply to avoid the condensation of the APTES vapor. Three different APTES vapor flow rates were controlled by the metering valve of the evaporator under an equal carrier gas flow rate of 80 sccm and a fixed chamber pressure of 1 torr (by tuning the vacuum valve). The exact APTES vapor flow rates were extracted by weighing the liquid APTES

in the evaporator before and after the reaction. Figure 4-2 (a) contains the growth curves of the free amine ratio deconvoluted from the XPS N_{1s} spectra of the three different APTES vapor flow rates, equaling to three concentrations. It clearly shows that the free amine ratio drops dramatically when a higher APTES vapor concentration is applied. This matches with the expectation that higher silane concentration enhances polymerization and hydrogen-bonding with adjacent molecules. It should be noted that even with a lower concentration under 110°C, the free amine ratio still cannot compete with the liquid-phase reaction. The explanation for this is that more physical adsorption happens, instead of covalent bonding, under this relatively low temperature. Figure 4-2 (b) shows the nitrogen-silicon ratio determined by the XPS full range scan for the same spot of each sample. In addition to the lower free amine ratio, samples that were vapor-silanized with a high APTES vapor flow rate also bear thick multilayer. The N/Si ratio can go as high as 0.38 for a 90-minute reaction under a 0.057g/min APTES vapor flow rate. But, for samples with a 0.009g/min APTES vapor flow rate, the growth of the APTES layer is extremely slow. The ellipsometry always shows a thickness less than 0.5 nm, indicating uncovered surfaces.

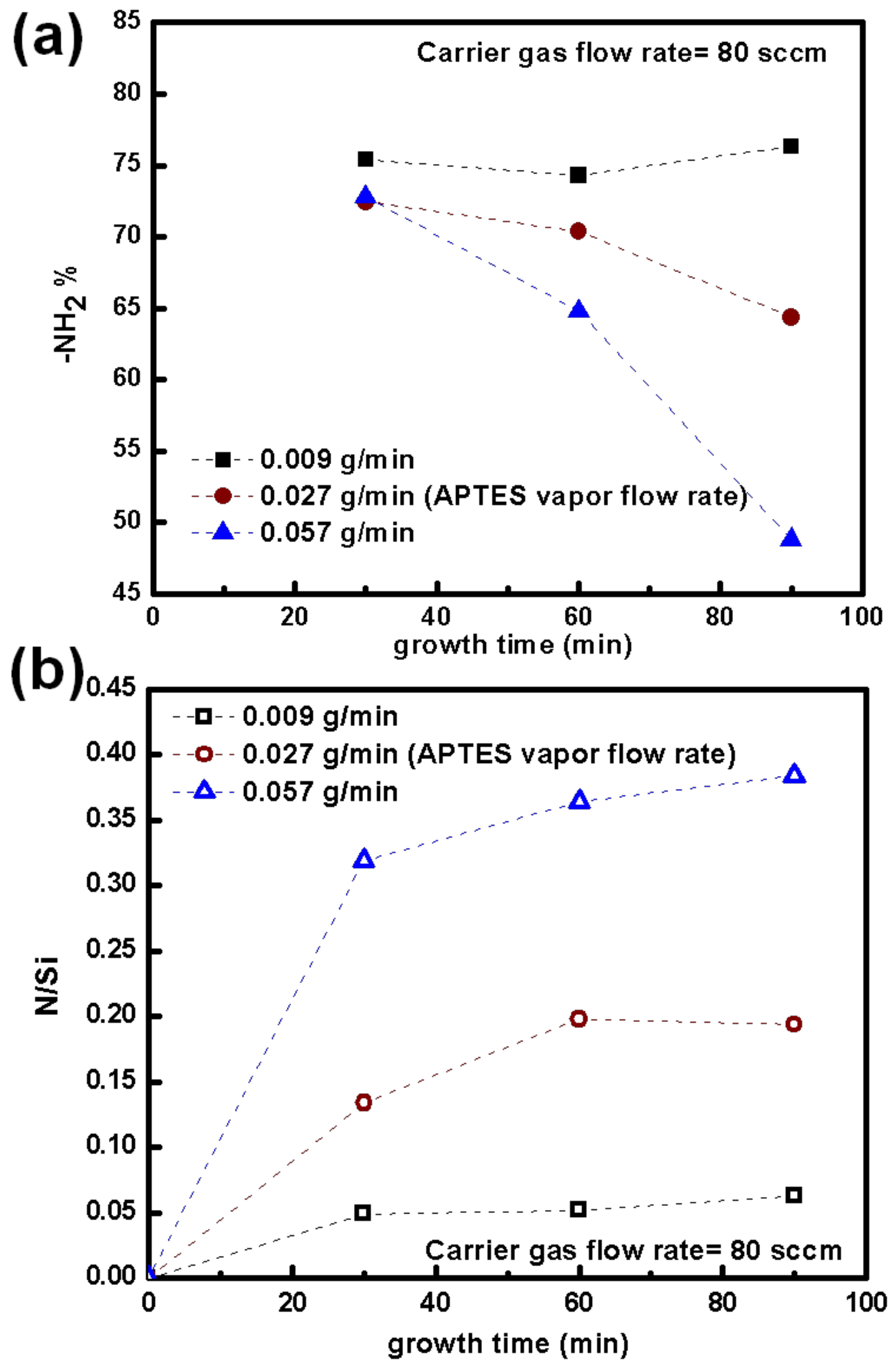

Figure 4-2: (a) Deconvoluted free amine ($-NH_2$) ratio in high resolution XPS spectra of N_{1s} region of vapor-silanized substrates using 0.009, 0.027, and 0.057 g/min APTES vapor flow rates with 30, 60, and 90 min reaction times for each of the flow rate settings; (b) Nitrogen/silicon atomic ratio determined by XPS full range scan for each data point in (a).

To further verify the effect of the APTES vapor concentration, deconvoluted XPS N_{1s} spectra and AFM topography images of 90-minute growth samples of three APTES vapor concentrations are shown in figure 4-3. The intensity of the XPS N_{1s} spectra is normalized to that of Si_{2p} to visually compare and present both the deconvolution results and the nitrogen-silicon ratio. Here it is clear that hydrogen-bonded amine levels increase with APTES vapor concentration. In the mean time, for a low APTES concentration, the signal intensity is still extremely weak even after 90 minutes of growth, indicating that the surface is not fully covered. In other words, an APTES layer which is able to fully cover the surface under this reaction temperature (110°C) has no way to generate a free amine ratio comparable to that of liquid-silanization. The surface morphology, revealed by the AFM images, apparently forms polymerized multilayer aggregates when a higher APTES concentration is used. The visual z-scales of all the AFM images in this report are well aligned, and the value in the z-axis indicates the maximum height in the image. The huge aggregation with a low free amine content is also an evidence that the polymerization of the aminosilane seriously consumes the free amine sites.

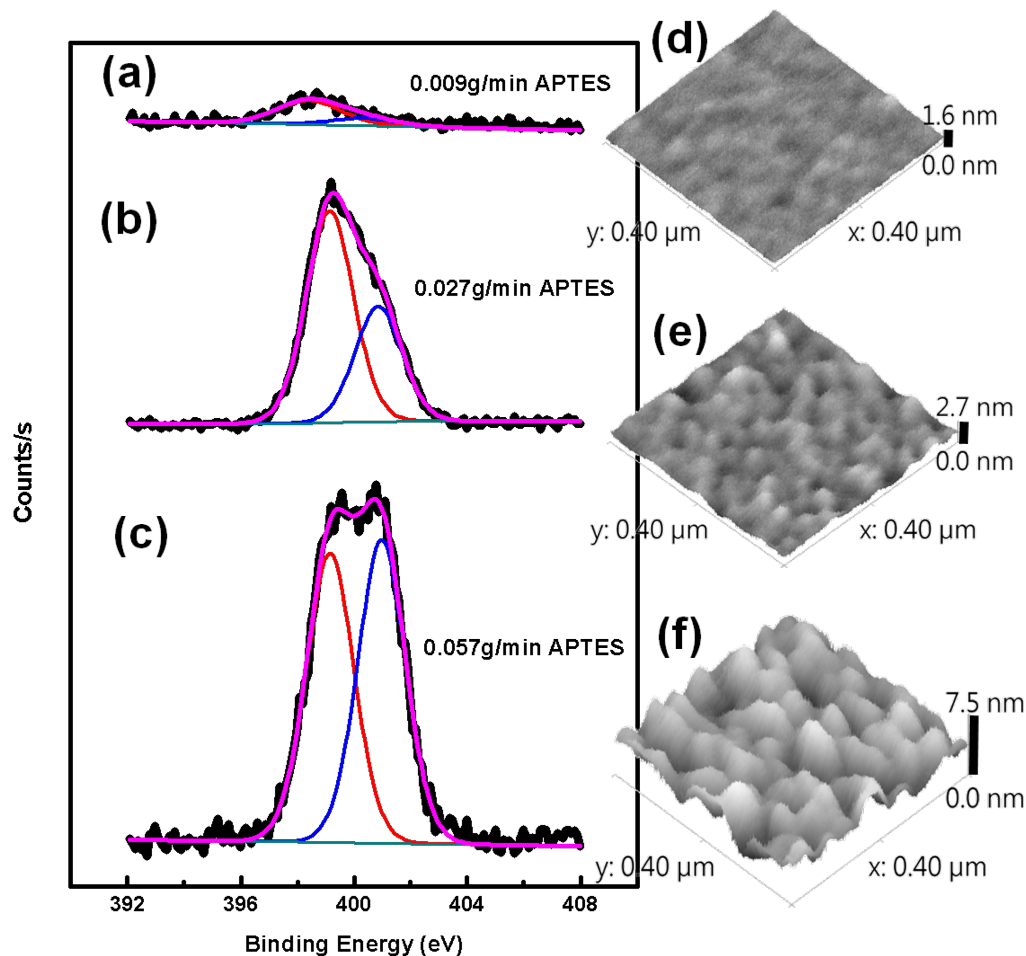

Figure 4-3: High resolution XPS spectra of N_{1s} region for APTES silanized silicon surface deposited by vapor-silanization (110˚C/90 minutes) with different APTES vapor concentration. (a) 0.009g/min APTES in 80sccm nitrogen carrier gas; (b) 0.027g/min APTES in 80sccm nitrogen carrier gas; (c) 0.057g/min APTES in 80sccm nitrogen carrier gas. The intensity of XPS N_{1s} spectra are normalized to that of Si_{2p} and are shifted; (d), (e), and (f) are the AFM topography images of (a), (b), and (c) respectively.

These three samples were further immersed in GO solution to test their reactivity to electrostatic attraction in the colloid. Figures 4-4 (a) to4-4 (c) are the SEM images of the samples corresponding to figures 3a to 3c after immersing in a 0.05mg/ml GO aqueous solution for 40 hours. The results clearly show that the final performance of the APTES layer is determined by the combination of the APTES density (coverage) and free amine ratio. First, the substrate deposited by high a APTES vapor concentration (figure 4-4 (c)) cannot generate a GO density as high as that which is deposited by the medium concentration (figure 4-4 (b)). However, the substrate deposited by the lowest APTES vapor concentration (figure 4-4 (a)) has an even lower GO density although it has the highest free amine ratio. Apparently, the poor APTES density is responsible for the low surface potential in this case. It should also be noted that none of these conditions can generate a continuous film.

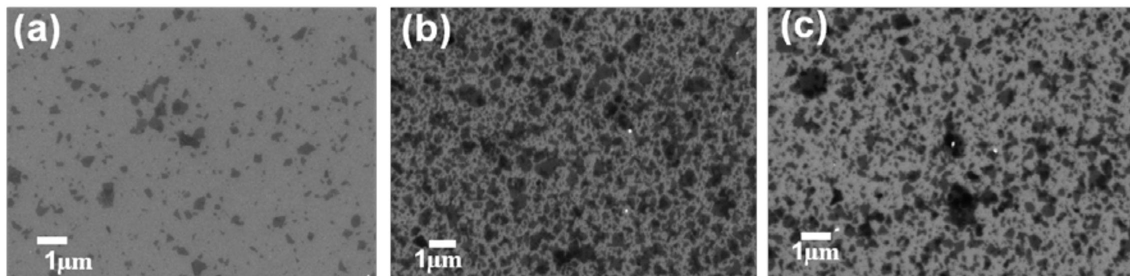

Figure 4-4: SEM images of samples in figure 4-3 after immersing in 0.05mg/ml GO solution for 40 hours. (a) 0.009g/min APTES vapor-silanized sample (figure 4-3 (a) and (d)) post GO immersion; (b) 0.027g/min APTES vapor-silanized sample (figure 4-3 (b) and (e)) post GO immersion; (c) 0.057g/min APTES vapor-silanized sample (figure 4-3(c) and (f)) post GO immersion.

Gas-phase reaction renders one more control factor, that is, the temperature of the substrate. A high temperature reaction could potentially eliminate the trace amount of adsorbed surface water, or alter the silanization rate. Since the reactivity cannot be improved to a satisfactory level simply by differing the APTES vapor concentration or growth time, the next step is to study the effect of the reaction temperature. In previous experiments, we have learned that a medium level APTES vapor concentration is the

compromise for APTES density and free amine content. A 0.027g/min APTES vapor flow in 80 sccm of nitrogen carrier gas, along with 90-minute growth time, was used in the study on temperature effect. Figure 4-5 shows the free amine and nitrogen-silicon ratio of the samples vapor-silanized under the above conditions at different temperatures. Interestingly, the free amine ratio has an initial drop from 90°C to 110°C and then increases with the reaction temperature. Toward the high temperature regime, the free amine ratio reaches a maximum value of 93.74% at 150°C. This is a value that cannot be easily achieved in liquid-silanization. There are two explanations for this. First, the adsorbed water is reduced to a minimum amount or cannot exist at a temperature that high, And, therefore, both silane polymerization and hydrogen-bonding resulting from the hydrolysis of the ethoxy group are inhibited.[14] Second, the high temperature enhances the covalent bonding of all three docking groups to surface siloxane. Although it has only been proved that post curing can help complete the siloxane bond to the surface,[18] we believe that the same result can be achieved while the reaction itself is at such a high temperature, so no unlinked silanol is left to react with the amine moiety by means of hydrogen-bonding. In the low temperature regime, it is unexpected that a high free amine ratio will also be obtained. Theoretically, this is a regime in which the condensation of the APTES happened. The mystery can be solved through comparison to the N/Si ratio in figure 4-5 (b). At 90°C, the N/Si ratio extracted by the XPS showed an extreme value, as high as 0.68. This means that the x-ray probes are almost equal in the amounts of nitrogen and silicon atoms, indicating an extremely thick film. This corresponds to the condensation; the huge amount of condensed APTES generates a strong and sharp primary amine peak (figure 4-6(a)). For high temperature silanization at 150°C, the N/Si ratio decreases to around 0.08. This is about the value of the highly dense APTES monolayer.[30] Further increasing the reaction temperature to 170°C will lower both the free amine ratio and the N/Si ratio. Actually, the free amine ratio stays at a high level

(85.21%); however, the low N/Si ratio (0.047) indicates that the surface is not fully covered (dense) at this condition.

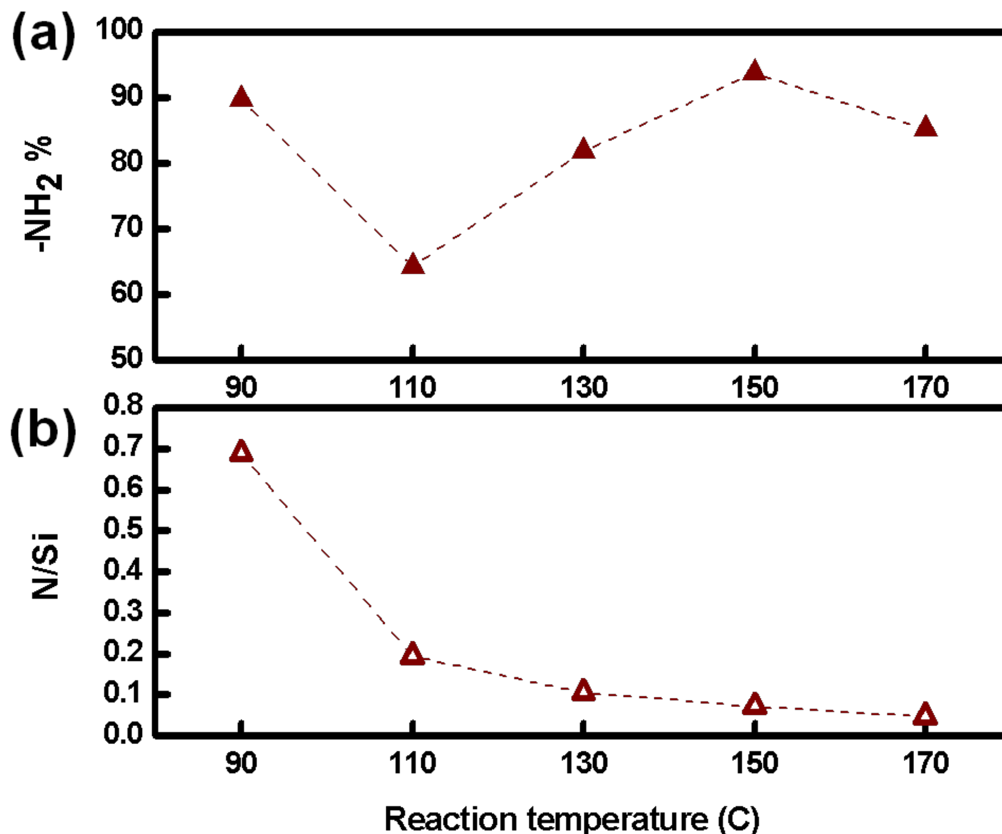

Figure 4-5: (a) Free amine ratio of 0.027g/min APTES vapor-silanized (90 minutes) surface versus reaction temperature; (b) nitrogen/silicon atomic ratio of 0.027g/min APTES vapor-silanized (90 minutes) surface versus reaction temperature.

Figure 4-6 shows the deconvoluted XPS N_{1s} spectra and AFM topography images of the samples in figure 4-5. The intensities of all N_{1s} spectra are normalized to1 in order to compare their free amine ratios. Figures 4-6 (b) to 6d show the real deconvoluted spectra with the increasing free amine from 110°C to 150°C shown in figure 4-5 (a). Although it has a high free amine ratio, figure 4-6 (a) has a peak intensity around five to seven times higher than others, as indicated by N/Si in figure 4-5 (b). Actually, the peak intensity of the hydrogen-bonded amine in figure 4-6 (a) is about the same as that of 4-6

(b) before normalization. It is also well known that monolayers of APTES are oriented with free amine groups away from the silicon surface and with hydrogen-bonded and protonated amines close to the surface, where they bind with surface siloxane.[16] So the total N_{1s} spectrum in 6a can be interpreted as a huge amount of APTES that is physically condensed on top of covalently bonded monolayers and is highly hydrolyzed and polymerized. The AFM topography image also shows rough film, seen in figure 4-6 (a). With the increasing of the reaction temperature, the morphology of the APTES layer tends to be smoother. For the 150°C sample, the film is very homogeneous, and there is no obvious grain boundary. Figure 4-7 (a) shows the ellipsometry thickness of these samples. As we have discussed, for the condensed APTES film in the 90°C silanized sample, the film is as thick as 15.32 nm. This thickness is significantly more than the thickness of the thin water film, so most of the amino groups are still intact, and it is responsible for the strong free amine peak in figure 4-6 (a). On the other hand, the thickness of the 150°C silanized sample is around 1nm, which is about a monolayer. Figure 4-7 (b) shows the RMS roughness extracted from the AFM topography images in figure 4-6. Again, the ultra thick film condensed at 90°C generates a RMS roughness as high as 0.88nm. For high temperature silanization, the surface RMS roughness at 150°C is 0.186 nm, which is around the same level as that of the bare silicon. Taking into account the maximum free amine ratio, the decent N/Si ratio, and the monolayer thickness, we conclude that the 150°C vapor-silanization generates a highly reactive, well ordered, and densely packed APTES monolayer.

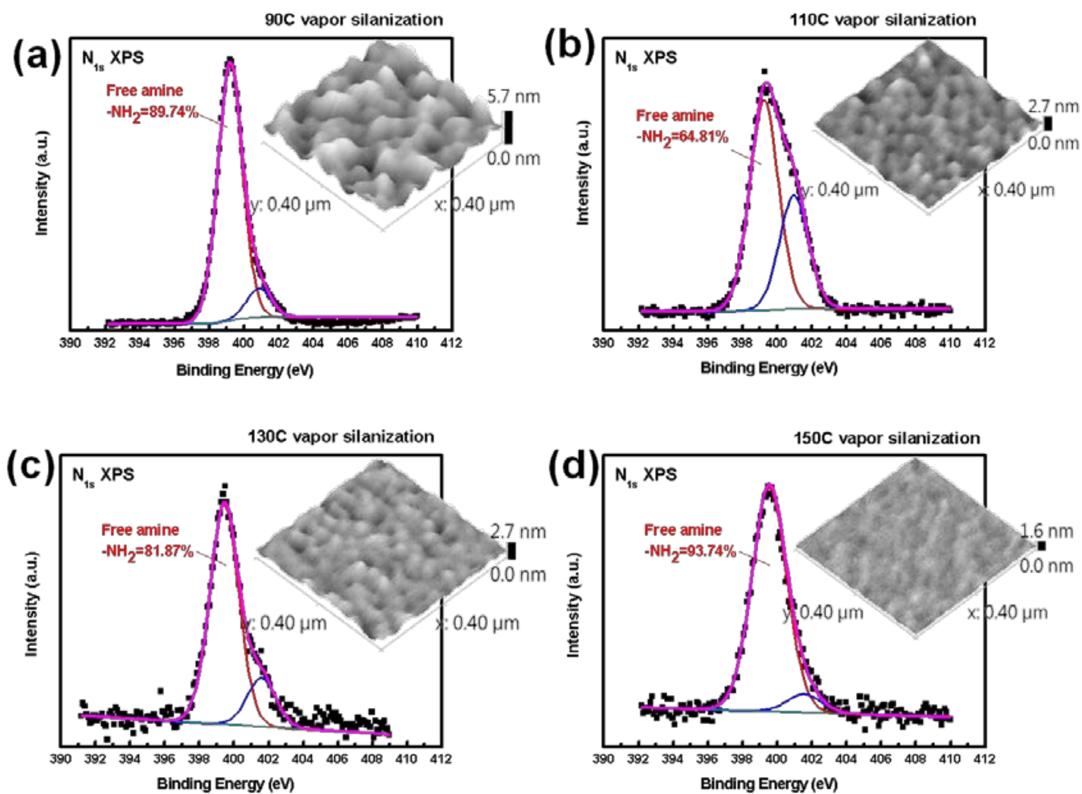

Figure 4-6: High resolution XPS spectra of N_{1s} region for APTES silanized silicon surface deposited by vapor-silanization (0.027g/min APTES vapor in 80 sccm N_2 for 90 minutes) with different reaction temperatures (a) 90˚C, (b) 110˚C, (c) 130˚C, and (d) 150˚C. Insets are the AFM topography images of corresponding XPS samples.

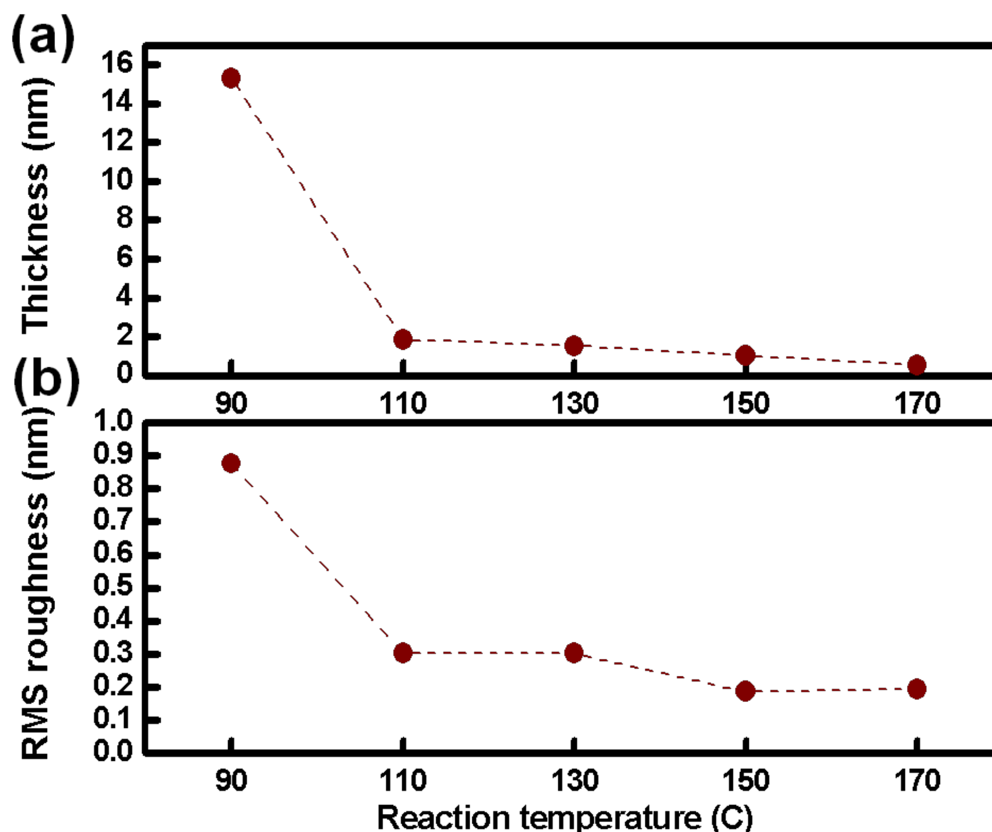

Figure 4-7: (a) Ellipsometry thickness of APTES silanized silicon surface deposited by vapor-silanization (0.027g/min APTES vapor in 80 sccm N_2 for 90 minutes) versus reaction temperature; (b) AFM measured RMS roughness (insets of figure 4-6) of APTES silanized silicon surface deposited by vapor-silanization (0.027g/min APTES vapor in 80 sccm N_2 for 90 minutes) versus reaction temperature.

Graphene oxide (GO) is known to be negatively charged by the carboxylic group at the edge and by the epoxy or hydroxyl group at the basal plane. Once immersed in aqueous solution, the APTES modified surface becomes positively charged and can effectively attract GO flakes. From previous experiments, we know that the vapor-silanization of APTES at 110°C is unable to generate a surface potential strong enough to assemble a continuous GO film (figure 4-4). Here we performed the same test for 150°C vapor-silanized samples (0.027g/min APTES vapor in 80 sccm N_2 for 90 minutes) to

examine the difference in the performance of GO self-assembly. Samples after the vapor-silanization of APTES at 150°C were immersed in 0.05mg/ml of GO aqueous solution for different periods of time, ranging from 30 seconds to 24 hours. For the calculation of the surface coverage rate, the "grains" with 1 nm height thresholds (the thickness of single GO flake) were a perfect match to the shapes of the GO flakes in the AFM topography images. For example, the red color in figures 4-8 (c) and 4-8 (e) indicate the grain area of figures 4-8 (b) and 4-8 (d), respectively. For heavily covered surfaces prepared by a longer GO deposition time (figure 4-8 (b)), it is found that small voids between overlapping flakes were probed at the zero point of height, generating a coverage rate greater than 99% (figure 4-8 (c)). For a shorter deposition time, grains with exactly a 1 nm thickness were isolated as islands (figure 4-8(d)), so it's clear that the GO that is self-assembled on the 150°C vapor-silanized surface can form continuous and overlapped film in 10 minutes. To the best of our knowledge, this is the first time a continuous GO film was formed by self-assembly in such a short time.

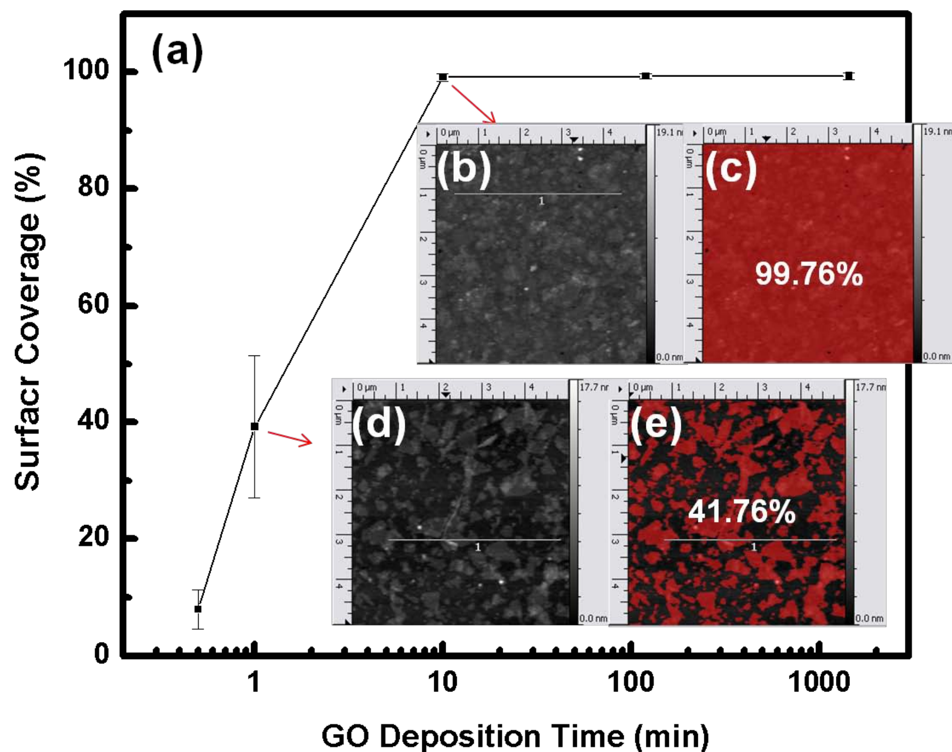

Figure 4-8: (a) Surface coverage rate of GO flakes on APTES silanized silicon surface deposited by vapor-silanization (0.027g/min APTES vapor in 80 sccm N_2 for 90 minutes at 150°C) versus GO solution immersion time; (b) AFM topography image of APTES silanized surface after 10-minute immersion in GO solution; (c) grain area calculated with 1 nm height threshold (red) from image (b); (d) AFM topography image of APTES silanized surface after 1-minute immersion; (e) grain area calculated with 1 nm height threshold (red) from image (d).

Figure 4-9 (a) is the SEM image of the APTES vapor-silanized surface (0.027g/min APTES vapor in 80 sccm N_2 for 90 minutes at 150°C) after a 10-minute immersion in the GO solution. The edge of the individual GO flakes could be clearly seen, and the stacking of the GO flakes could also be observed by the difference in color. Another frequent application for APTES is the immobilization of gold nanoparticles (AuNPs). Therefore, our optimized APTES surface was also tested by confirming the capability of immobilized AuNPs. Figure 4-9 (b) is the AFM topography image of our

APTES surface after a 10-min immersion in AuNPs aqueous solution and a copious rinse. The result also shows highly dense AuNPs arrays with multilayer stacking. In addition to the better APTES quality, vapor-silanization has another advantage in accommodating substrate bearing photoresist patterns, which not accessible in solvent mediated silanization due to re-dissolution problems. In the case of GO deposition, a GO pattern can be generated as follows: 1) vapor-silanization of APTES on photoresist pattern; 2) GO self-assembly; and 3) lift-off the resist. Figures 4-9 (c) and 4-9 (d) are the high magnification SEM images of the GO - SiO_2 border made using the above procedure. They prove that the self-assembled GO film is continuous, and the overlapping of the GO flakes can be clearly observed.

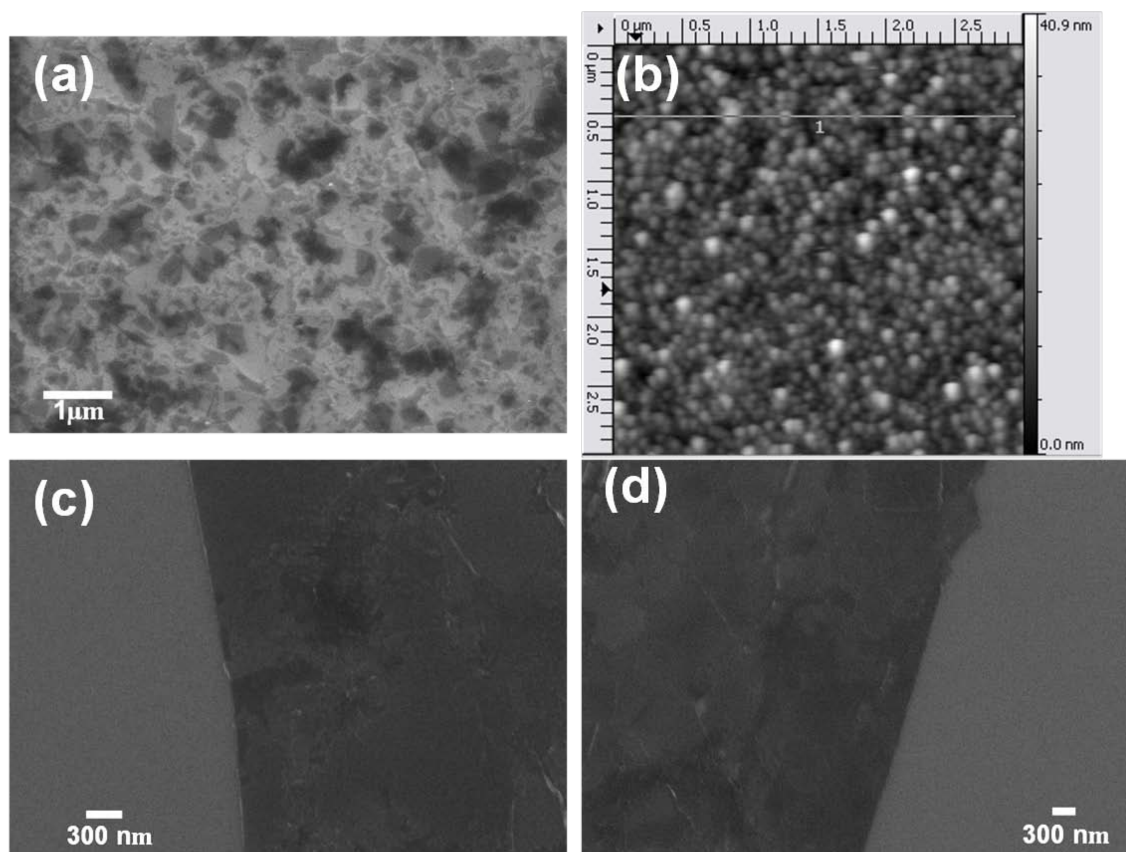

Figure 4-9: (a) SEM image of APTES vapor-silanized surface (0.027g/min APTES vapor in 80 sccm N_2 for 90 minutes at 150°C) after 10 -minute immersion in GO solution; (b) AFM topography image of APTES vapor-silanized surface (0.027g/min APTES vapor in 80 sccm N_2 for 90 minutes at 150°C) after 10-minute immersion in AuNPs solution; (c) and (d) SEM images of edges of continuous GO film made by self-assembly of GO flakes on APTES and lift-off.

4.5 Conclusions

Although it is well known that gas-phase silanization has multiple advantages which a liquid-phase reaction cannot compete with, including the promotion of covalent bonding and removal of surface water with elevated temperatures, not to mention that gas-phase silanization is solvent-free. However, the exact reaction condition and product performance for gas-phase silanization are still not clear. We investigated the effects of factors such as APTES vapor concentration, reaction time, and reaction temperature on

the quality of gas-phase deposited APTES molecular films that were self-assembled on the SiO_2 surface. It was found that increasing the APTES vapor concentration will dramatically reduce the free amine content and result in an extremely rough film. However, even with a low vapor concentration (0.009g/min APTES vapor in 80 sccm N_2), the free amine ratio generated under the low reaction temperature (110°C) is still not able to compete with liquid-silanization. A study on the reaction temperature's effect was then performed using optimized APTES vapor concentration and growth time (0.027g/min APTES vapor in 80sccm N_2 for 90 minutes). Vapor-silanization performed under 150°C can generate an APTES layer that has a high free amine content (93.74%) and that is uniform in morphology (RMS roughness=0.186nm; thickness=0.7nm). We also examined the electrostatic force of vapor-silanized APTES layers by performing the immobilization of GO and AuNPs. With an optimized condition (0.027g/min APTES vapor in 80sccm N_2 for 90 minutes at 150°C), a continuous GO thin film can be deposited on the APTES layer in 10 minutes through the self-assembly of the GO flakes. Similarly, highly dense AuNPs arrays can also be immobilized in the form of multilayer stacking. In addition, patterned GO thin film was generated through the vapor-silanization of APTES, the self-assembly of GO flakes, and the lift-off. This results are not accessible when using liquid-phase silanization.

4.6 References

1. Almeida, A. T.; Salvadori, M. C.; Petri, D. F. S., Enolase adsorption onto hydrophobic and hydrophilic solid substrates. *Langmuir* **2002,** *18* (18), 6914-6920.

2. Tanigawa, M.; Okada, T., Atomic force microscopy of supercoiled DNA structure on mica. *Analytica Chimica Acta* **1998,** *365* (1-3), 19-25.

3. Niwa, D.; Yamada, Y.; Homma, T.; Osaka, T., Formation of molecular templates for fabricating on-chip biosensing devices. *Journal of Physical Chemistry B* **2004,** *108* (10), 3240-3245.

4. Strother, T.; Cai, W.; Zhao, X. S.; Hamers, R. J.; Smith, L. M., Synthesis and characterization of DNA-modified silicon (111) surfaces. *Journal of the American Chemical Society* **2000,** *122* (6), 1205-1209.

5. Lin, Z.; Strother, T.; Cai, W.; Cao, X. P.; Smith, L. M.; Hamers, R. J., DNA attachment and hybridization at the silicon (100) surface. *Langmuir* **2002,** *18* (3), 788-796.

6. Crego-Calama, M.; Reinhoudt, D. N., New materials for metal ion sensing by self-assembled monolayers on glass. *Advanced Materials* **2001,** *13* (15), 1171-+.

7. Kong, D. I.; Park, C. E.; Hong, S. T.; Yang, H. C.; Kim, K. T., Effects of coupling agent thickness on residual stress in polyimide/gamma-APS/silicon wafer joints. *Journal of Adhesion Science and Technology* **1999,** *13* (7), 805-818.

8. Sugimura, H.; Nakagiri, N., Nanoscopic surface architecture based on scanning probe electrochemistry and molecular self-assembly. *Journal of the American Chemical Society* **1997,** *119* (39), 9226-9229.

9. Freeman, R. G.; Grabar, K. C.; Allison, K. J.; Bright, R. M.; Davis, J. A.; Guthrie, A. P.; Hommer, M. B.; Jackson, M. A.; Smith, P. C.; Walter, D. G.; Natan, M. J., Self-Assembled Metal Colloid Monolayers - an Approach to Sers Substrates. *Science* **1995,** *267* (5204), 1629-1632.

10. Becerril, H. A.; Mao, J.; Liu, Z.; Stoltenberg, R. M.; Bao, Z.; Chen, Y., Evaluation of solution-processed reduced graphene oxide films as transparent conductors. *Acs Nano* **2008,** *2* (3), 463-470.

11. Wikstrom, P.; Mandenius, C. F.; Larsson, P. O., Gas-Phase Silylation, a Rapid Method for Preparation of High-Performance Liquid-Chromatography Supports. *Journal of Chromatography* **1988,** *455*, 105-117.

12. Cain, J. F.; Sacher, E., Auger-Electron Spectroscopy of Deposited Silane Layers. *Journal of Colloid and Interface Science* **1978,** *67* (3), 538-540.

13. Ishida, H., A Review of Recent Progress in the Studies of Molecular and Microstructure of Coupling Agents and Their Functions in Composites, Coatings and Adhesive Joints. *Polymer Composites* **1984,** *5* (2), 101-123.

14. White, L. D.; Tripp, C. P., Reaction of (3-aminopropyl)dimethylethoxysilane with amine catalysts on silica surfaces. *Journal of Colloid and Interface Science* **2000,** *232* (2), 400-407.

15. Blum, F. D.; Meesiri, W.; Kang, H. J.; Gambogi, J. E., Hydrolysis, Adsorption, and Dynamics of Silane Coupling Agents on Silica Surfaces. *Journal of Adhesion Science and Technology* **1991,** *5* (6), 479-496.

16. Vandenberg, E. T.; Bertilsson, L.; Liedberg, B.; Uvdal, K.; Erlandsson, R.; Elwing, H.; Lundstrom, I., Structure of 3-Aminopropyl Triethoxy Silane on Silicon-Oxide. *Journal of Colloid and Interface Science* **1991,** *147* (1), 103-118.

17. Boerio, F. J.; Schoenlein, L. H.; Greivenkamp, J. E., Adsorption of Gamma-Aminopropyltriethoxysilane onto Bulk Iron from Aqueous-Solutions. *Journal of Applied Polymer Science* **1978,** *22* (1), 203-213.

18. Engelhardt, H.; Orth, P., Alkoxy Silanes for the Preparation of Silica Based Stationary Phases with Bonded Polar Functional-Groups. *Journal of Liquid Chromatography* **1987,** *10* (8-9), 1999-2022.

19. Chiang, C. H.; Liu, N. I.; Koenig, J. L., Magic-Angle Cross-Polarization C-13 Nmr-Study of Aminosilane Coupling Agents on Silica Surfaces. *Journal of Colloid and Interface Science* **1982,** *86* (1), 26-34.

20. Haller, I., Covalently Attached Organic Monolayers on Semiconductor Surfaces. *Journal of the American Chemical Society* **1978,** *100* (26), 8050-8055.

21. Hozumi, A.; Yokogawa, Y.; Kameyama, T.; Sugimura, H.; Hayashi, K.; Shirayama, H.; Takai, O., Amino-terminated self-assembled monolayer on a SiO2 surface formed by chemical vapor deposition. *Journal of Vacuum Science & Technology a-Vacuum Surfaces and Films* **2001,** *19* (4), 1812-1816.

22. Song, X. Y.; Zhai, J.; Wang, Y. L.; Jiang, L., Self-assembly of amino-functionalized monolayers on silicon surfaces and preparation of superhydrophobic surfaces based on alkanoic acid dual layers and surface roughening. *Journal of Colloid and Interface Science* **2006,** *298* (1), 267-273.

23. Asenath-Smith, E.; Chen, W., How To Prevent the Loss of Surface Functionality Derived from Aminosilanes. *Langmuir* **2008,** *24* (21), 12405-12409.

24. Fiorilli, S.; Rivolo, P.; Descrovi, E.; Ricciardi, C.; Pasquardini, L.; Lunelli, L.; Vanzetti, L.; Pederzolli, C.; Onida, B.; Garrone, E., Vapor-phase self-assembled monolayers of aminosilane on plasma-activated silicon substrates. *Journal of Colloid and Interface Science* **2008,** *321* (1), 235-241.

25. Zhang, F.; Sautter, K.; Larsen, A. M.; Findley, D. A.; Davis, R. C.; Samha, H.; Linford, M. R., Chemical Vapor Deposition of Three Aminosilancs on Silicon Dioxide: Surface Characterization, Stability, Effects of Silane Concentration, and Cyanine Dye Adsorption. *Langmuir* **2010,** *26* (18), 14648-14654.

26. Ek, S.; Iiskola, E. I.; Niinisto, L.; Vaittinen, J.; Pakkanen, T. T.; Keranen, J.; Auroux, A., Atomic layer deposition of a high-density aminopropylsiloxane network on silica through sequential reactions of gamma-aminopropyltrialkoxysilanes and water. *Langmuir* **2003,** *19* (25), 10601-10609.

27. Hummers, W. S.; Offeman, R. E., Preparation of Graphitic Oxide. *Journal of the American Chemical Society* **1958,** *80* (6), 1339-1339.

28. Kovtyukhova, N. I.; Ollivier, P. J.; Martin, B. R.; Mallouk, T. E.; Chizhik, S. A.; Buzaneva, E. V.; Gorchinskiy, A. D., Layer-by-layer assembly of ultrathin composite films from micron-sized graphite oxide sheets and polycations. *Chemistry of Materials* **1999,** *11* (3), 771-778.

29. Simon, A.; Cohen-Bouhacina, T.; Porte, M. C.; Aime, J. P.; Baquey, C., Study of two grafting methods for obtaining a 3-aminopropyltriethoxysilane monolayer on silica surface. *Journal of Colloid and Interface Science* **2002,** *251* (2), 278-283.

30. Heiney, P. A.; Gruneberg, K.; Fang, J. Y.; Dulcey, C.; Shashidhar, R., Structure and growth of chromophore-functionalized (3-aminopropyl)triethoxysilane self-assembled on silicon. *Langmuir* **2000,** *16* (6), 2651-2657.

CHAPTER 5

SOLUTION-PROCESSED GRAPHENE DEVICE FABRICATED BY SELF-ASSEMBLY OF GRAPHENE OXIDE ON VAPOR-DEPOSITED AMINOSILANE

Fabrication of graphene-based electronics by solution-processed graphene oxide (GO) has the advantages of low cost, scalability, ease of processing, and feasibility for various substrates. Reduced graphene oxide (rGO) thin film is electrically conductive, rendering it a potential material for organic electrodes. While reducing its thickness to a few atomic layers, similar to graphene, rGO also shows semiconducting properties along with high chemical sensitivity, making it suitable for sensing applications. In this work, we present a process to pattern and deposit both GO thin film or few-layer GO by a combination of conventional lithography, vapor silanization, GO self-assembly (or spin-coating), and lift-off. We explored an effective method to deposit 3-aminopropyltriethoxysilane (APTES) through a vapor phase and were able to generate a surface with a higher ratio of free amine. The transfer characteristics of GO film self-assembled on vapor-silanized APTES proved that we can precisely deposit continuous few-layer GO with 1~3 layers, and its high on/off ratio is desired for sensory. Besides, the under-layer amine corrected the intrinsic p-doping effect of rGO in air, and the level of n-doping is believed to be tunable. On the other hand, we also showed that the vapor-silanized APTES layer can form strong electrostatic attraction and further increase film thickness to reach higher conductivity, which is desired for organic electrodes. Devices bearing rGO source-drain showed superior performance than gold electrodes.

5.1 Introduction

Graphene is emerging as a promising material that ushers nanoelectronics into a new era. Unlike carbon nanotubes (CNTs), which were proved having amazing properties but limited applications, the 2D structure of graphene makes it scalable and easy to fit into modern semiconductor processes. Among the major synthesis methods of geaphene, GO is the only solution-processed approach that has the advantages of simple, scalable, feasible for various substrates, and most important of all, no need for expensive equipment and harsh conditions such as UHV and high temperatures[1]. By filming from dispersed flakes and varying the thickness, rGO can be applied in two types of devices: (1) Ultra-thin film (~1 to 3 nm) for chemical and biological sensing [2-4], and (2) thicker film (~20 to 50 nm) for transparent organic electrodes [5, 6]. Although stacked by individual flakes, a continuous rGO network with fewer than three layers still shows significant semiconducting properties [7]. Along with the sensitivity of electronic properties to surface conditions, ultra-thin rGO film becomes an excellent candidate for sensing applications. While the rGO film is in the range of 4~7 layers, it becomes semi-metallic[7, 8]. Beyond this range, rGO film tends to be a conductor, and sheet resistance dramatically drops with the increase of thickness. Typically, rGO film with 20 nm in thickness can reach a sheet resistance that is sufficiently low to be electrodes, approximately 10^3 Ω/square. Although the conductivity cannot compete with standard metal electrodes, the superior charge injection in organic-organic contact still renders graphene a promising electrode material[5, 6].

5.2 Background

Since extreme thickness (i.e., ultra-thin for sensory or thick for an electrode) is required, the development of deposition techniques and thickness control become very crucial. Eda et al. first published the filtration method[7]. GO water solution was filtered

through the membrane, leading GO flakes to accumulate and form continuous film. This method was proved to precisely control the layer number of accumulated GO flakes by demonstrating transfer characteristics of both semiconducting (~1 to 3 layers) and semi-metallic (~4 to 6 layers). The key is to control the interaction between concentration and volume of the solution. However, a final step is always needed to transfer the film to the target substrate, which increases the operational difficulties and potential contamination. For this reason, various coating methods, such as dip coating[9], drop casting[10], air spray[9], and L-B film[11], have been adopted to directly coat GO films on the desired substrate. It is known, however, that these methods either have less control of thickness and uniformity or are not suitable for large scale production. Pang et al. demonstrated that GO flakes could be spin-coated on hydrophilic surfaces with the desired thickness and high uniformity[5]. Moreover, multilayer coating is also possible, largely increasing the film thickness and the resulting conductivity. But for ultra-thin film deposition, by spin-coating on a bare surface, it's difficult to fully cover the surface without the edge of GO flakes overlapping each other. That's the explanation for the generally poor on/off ratio of spin-coated rGO ultra-thin film. Becerril et al. spun GO solution on an aminosilane-treated quartz surface and rendered a record-high transmittance-sheet resistance ratio[12]. In other words, lower sheet resistance can be achieved with equally high transmittance, indicating higher surface coverage and more conducting pathways.

For the purpose of device fabrication, development of an efficient patterning method for GO thin film is also important. Pang et al. patterned their spin-coated GO film by an oxygen plasma etch[5]. Wang et al. patterned photoresist first by conventional lithography and did lift-off after GO film was deposited [10]. Becerril et al. in their later publication compared the performance between top-down GO etch and bottom-up GO lift-off by evaluating organic thin-film transistors (OTFTs) bearing GO electrodes deposited by both means[6]. The carrier mobility of the same material such as pentacene was extracted by both types of OTFTs, and they concluded that the GO lift-off method

performs better, because no oxygen plasma was involved in the already reduced GO film. On the other hand, the top-down etch method generated patterns with lower resolution due to the limit of the shadow mask. It should be noted that in this publication, aminosilane was not applied as previously, probably due to the difficulty of performing silanization with a photoresist pattern. For ultra-thin film, amine-terminated self-assembly monolayers (SAMs) were deposited on the surface by means of micro-contact printing (μCP) or dip pen nanolithography (DPN) to selectively attract GO flakes[13-16]. Although GO patterns could be clearly generated, the surface coverage can never reach 100% as concluded [13], and no evidence of I-V data or conductivity measurement was shown in these papers. The possible reason is that the packing order of SAMs and the resulting surface potential from these methods cannot compete with those generated from a silanization reaction.

3-aminopropyltriethoxysilane (APTES) has been widely used to immobilize gold nanoparticles (AuNPs), zinc oxide, or biological molecules (e.g., protein) by electrostatic attraction. Graphene oxide is also known to be negatively charged by the carboxylic group at the edge, and the epoxy or hydroxyl group at the basal plane. Once immersed in aqueous solution, an APTES-modified surface becomes positively charged and can effectively attract GO flakes. Typically, silanization reactions are mostly performed in the liquid phase due to the convenience and well-studied reaction conditions. However, while processing with a patterned surface, solvent will dissolve or swell photoresist and ruin the resolution. Besides, a huge amount of solvent is not preferred in the industry. An alternative approach is vapor-silanization[17]. Similar to atomic layer deposition (ALD), APTES could be treated as a vaporized precursor (gas phase) and react with surface silanol (solid phase) to form an amino self-assembly monolayer (solid phase). In some cases, vapor-silanization was also described as chemical vapor deposition[18, 19]. Performing silanization through the vapor phase is not a new concept. But the process condition and the quality of produced SAMs have not been systematically studied.

In this work, the vapor-silanization of APTES was performed on a photo-resist pattern generated by conventional lithography. The SAMs were proved to have a quality superior to those deposited from the liquid phase by the examination of X-ray photoemission spectroscopy (XPS). For thick film deposition, a combined one-step self-assembly and spin-coating method was performed to generate source-drain patterns with a 45 nm GO film. We also compared the performance of rGO electrodes to gold electrodes by extracting the carrier mobility of P3HT. Ultra-thin films with approximately two GO layers and five GO layers were self-assembled on prepared gold source-drain electrodes, and the transfer characteristics demonstrated semiconducting and semi-metallic features respectively, proving the capability of forming continuous ultra-thin film. Moreover, an important n-doping effect attributed to APTES was also explored. Generally speaking, graphene field-effect transistors (FETs) always show a certain extent of p-doping in an ambient condition. It has been proved that oxygen and water in the air contribute to this p-doping effect[7, 20]. It has been revealed that simply the surface condition of gate oxide (e.g., hydroxyl group and cleaning method) will contribute to the doping effect [21-23]. Wang et al. depicted that modifying the gate oxide surface with various types of silane, including APTES, would promote the charge transfer between graphene and substrate, resulting in the change of surface potential and Fermi level[24]. The n-doping or p-doping of graphene could then be achieved by under-layer surface modification. Here, for the first time, we demonstrate the APTES-induced n-doping of rGO film in the transfer characteristics.

5.3 Experimental

Preparation of Graphene Oxide Aqueous Solution. Graphite oxide was synthesized from natural graphite by a modified Hummers method as originally presented by Kovtyukhova and colleagues [25, 26]. GO solutions with different concentrations were prepared by dispersing synthesized GO powder into DI water, followed by a two-step

sonication. In this experiment, we prepared GO solution for 0.05mg/ml, 3mg/ml, 10mg/ml, and 17mg/ml. First, a mild bath sonication was introduced for 10 minutes to roughly disperse GO powder (Branson model 5510). At this step, GO suspension can be clearly seen, and the particle size cannot be further reduced. Therefore, a second-stage dispersion was performed by horn sonication for one minute (750W, sonics & materials VCX750), which effectively breaks GO flakes into small pieces. The solution is now well dispersed, and suspension particles are not visible anymore. Because GO powder is highly acidic, to stabilize GO flakes, the pH of the prepared GO solution was adjusted to around eight by 1% ammonia. The solution was then centrifuged at 14,000 RPM for 10 minutes to remove significant aggregation.

Substrate preparation and Vapor-Silanization of APTES. Highly doped, n-type (100) silicon wafers bearing 300 nm of thermally grown oxide were used as substrates. Electrode or square active-layer patterns were transferred by conventional lithography. Samples with patterned photoresist (Shipley 1827) were then baked at 110˚C to harden the resist, followed by an oxygen plasma treatment (Harrick PDC-32G plasma cleaner/sterilizer with air as the source gas and a base pressure of 0.4 torr) for one minute to hydroxylate the open area. To obtain best APTES quality (Figure 5-2), vapor silanization was performed with a following procedure. Briefly, the sample was put into the reaction chamber and heated to 140˚C. The evaporator was first isolated and heated to 110˚C to vaporize APTES. In the mean time, an 80 sccm nitrogen carrier gas flow was introduced into the chamber, and chamber pressure was fixed at one torr with flowing nitrogen by controlling the pumping valve. The meter valve of the evaporator was then opened for 90 minutes and controlled at a 2% nitrogen flow (the meter valve was calibrated in advance). After reaction, the sample was rinsed with a copious amount of DI water and blown dry.

Deposition of GO Film. For the self-assembly of ultra-thin film, samples after vapor-silanization were just immersed in a 0.05mg/ml GO solution for 30 minutes or 24

hours, followed by a DI water rinse. For thick film deposition, GO solution was first dropped to fully cover the substrate and rested for 10 minutes. Then the spin-coating was started according to the below recipe: 1). Spin at 600RPM for one minute using 100RPM/sec accelerating rate. 2). Spin at 1200RPM for one minute using 100RPM/sec accelerating rate. Finally, the samples were baked at 100˚C for five minutes.

GO Thermal Reduction. Samples were annealed in a Lindberg furnace backfilled with forming gas (4% hydrogen in argon). The ramping rate was 10˚C/min and the annealing time was three hours.

OFET and 4-pt probe Measurement. The OFET transfer characteristics were monitored using a semiconductor device analyzer (AGILENT b 1500a) either in a glove box with nitrogen or in air. The four-point probe measurement was performed using a signatone four-point probe station and Keithley 2400 multimeter.

Characterization of GO Film (AFM, XPS, and Ellipsometry). The topography of the GO surface and thickness of the GO electrode was investigated by tapping-mode AFM (Agilent 5500, picoplus system). Probes used for this study had a spring constant = 40N/m and tip curvature < 10 nm. The composition of nitrogen bonding in APTES and the thermal reduction progress of GO were probed by X-ray photoelectron spectroscopy (XPS, Thermo-K Alpha). Al K α X-ray radiation was X-ray excitation source, and beam size was set to be 400μm. The power was set to 150W and the voltage to 20eV for high-resolution scanning. The fitted peaks of XPS spectra were determined by a combination of Gaussion and Lorentzian distributions. The thickness of GO films was measured by an M-2000 Variable Angle Spectroscopic Ellipsometer (VASE, J.A. Woollam). Ellipsometry data were collected over a wavelength range from 400 to 1000 nm at angles of 65°, 70° and 75° (with respect to the normal substrate plane). Data were analyzed and fit to determine film thickness and refractive index by employing a Cauchy model for the films and using stacked layers including GO, APTES, SiO_2, and Si. To precisely extract

the GO thickness, the thickness of SiO_2 and APTES were both measured prior to the deposition of the next layer.

5.4 Results and Discussion

Figure 5-1 illustrates the overall scheme of the process of making ultra-thin or thick GO patterns, along with the concept of vapor-silanization. The overall process is based on the lift-off method combined with newly developed techniques, including vapor-silanization and combined self-assembly & spin-coating. The lift-off method avoids applying each process in rGO film, which involves both oxygen plasma and photoresist on already-reduced GO. Besides, it generates a higher resolution compared to a metal shadow mask. To adopt lift-off, vapor-silanization replaces the conventional liquid-phase silane modification in order to preserve photoresist. The APTES layer functions as a GO-SiO_2 interface that provides adequate electrostatic force to perform GO self-assembly. Therefore, the quality of surface amine is very important. Vapor-silanization has been proved capable of generating equally high quality SAMs with a liquid-phase reaction. It was also believed that printing methods such as PDMS stamp and DPN cannot generate high-density and well-ordered amino SAMs due to the lack of surface reaction. With strong electrostatic attraction, continuous GO film can be achieved by self-assembly of GO flakes. The spin-coated thicker film can also increase its thickness by the presence of an APTES layer. It indicates that both a sensing application (which requires few-layer graphene as semiconductor) and organic electrodes (which need thick layers of graphene as conductor) can be benefited by our process.

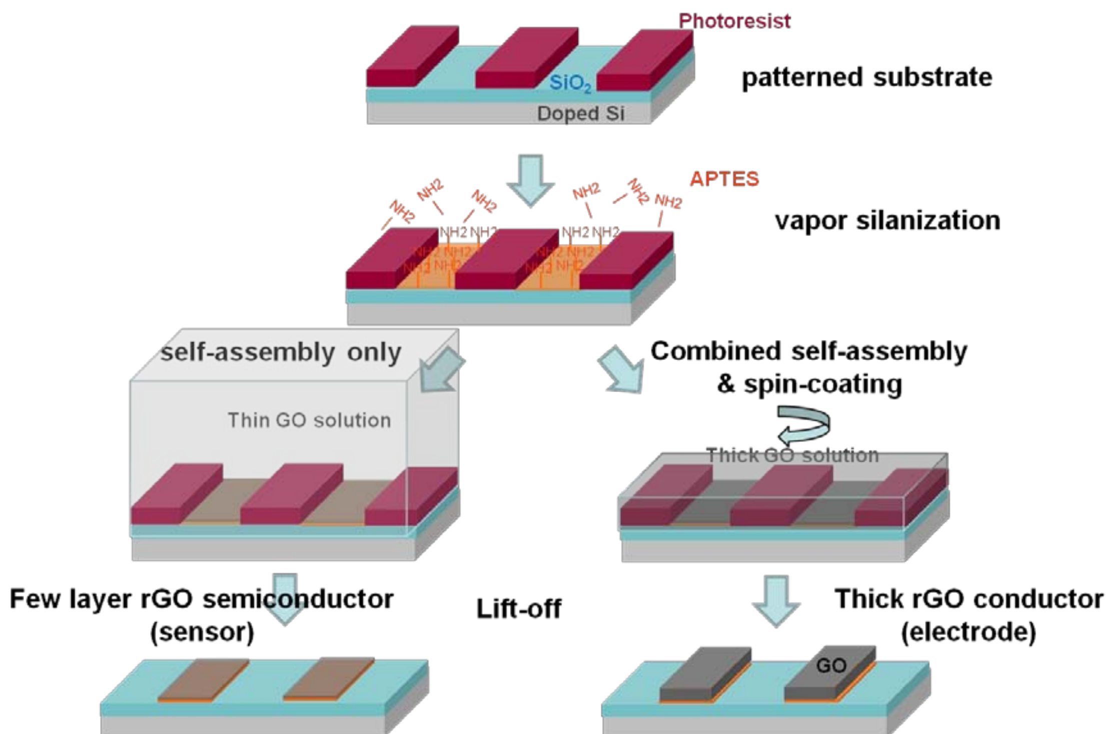

Figure 5-1: Schematic illustration of the lift-off process for fabricating both few-layer rGO active layer and thick rGO electrodes by the aid of vapor-silanization of APTES.

Unlike the solvent-mediated silanization method, growing self-assembly monolayers thorough the vapor phase has not been a mature process, and many factors that might influence SAMs' quality are not well studied yet. For example, temperature effect has been ignored in most literature, and the surface reaction was operated either at an inappropriate temperature or in the same chamber as APTES. The volume percentage of the APTE vapor in carrier gas has not been given enough attention either, while concentration is the key factor in the liquid-silanization. Figure 5-2 shows the high resolution XPS spectra of the N_{1s} region for an APTES silanized surface modified in different silanization conditions. N_{1s} XPS is the best tool to examine the quality of surface amine, and most of the liquid-silanization conditions were determined by this technique[27]. Briefly, N_{1s} peak acquired from an aminosilane-treated surface could be de-convoluted into two peaks: 398.7eV for free amine and 400.7eV for hydrogen-bonded amine. Differing from alkyl SAMs, such as Octadecyltrichlorosilane (OTS), aminosilane has

greater complexity due to the high reactivity between the amino head group and either surface silanol or hydrolyzed silanol of its neighbor's docking group. Both of these reactions will generate hydrogen bongings and occupy lone pairs, making the loss of active sites. Accordingly, a higher ratio of free amine is desired. We performed vapor-silanization in a homemade vacuum system containing separated reactor chambers and a silane evaporator. A carrier gas-flow system was used to deliver APTES vapor. The temperatures of the reactor and the APTES evaporator (110° C) was controlled separately and the pressure baseline in the system was set to 1 torr. Figure 5-2 (a) is the XPS result of an APTES-modified SiO_2 surface prepared by immersion in 3mM APTES/dry toluene solution for three hours. This is a standard liquid-silanization procedure and generates 84.25% of free amine on the surface. Figure 5-2 (b) shows the XPS result of a surface prepared by vapor-silanization. Both reactor chamber and evaporator were set to 110° C, and the concentration of the APTES vapor in the carrier gas flow was tuned to 3%. This temperature can barely avoid the condensation of APTES, and the XPS result shows a poor free amine rate (only 48.83%). By lowering the amine concentration, the free amine rate can be increased to 64.81% (Figure 5-2 (c)). Similar to liquid-silanization, a lower concentration is always preferred for surface modification. One more factor that could be altered in the vapor-phase reaction is the temperature. While the reactor temperature is elevated to 140° C, the free amine rate can be increased to 93.74% (Figure 5-2 (d)). This value has been higher than the standard liquid-phase method. The explanation is that a high temperature can hugely increase the reaction rate of silanization. Combined with the low reactant concentration, the vapor-silanization turns out to be diffusion-controlled, which is preferred in monolayer deposition. Moreover, a higher silanization rate makes silanols react with adjacent compound before having a chance to form hydrogen bonding with amine. Details of the APTES vapor-

silanization research will be reported elsewhere. All the APTES vapo-silanization processed in this experiment followed the optimized condition as in Figure 5-2 (d).

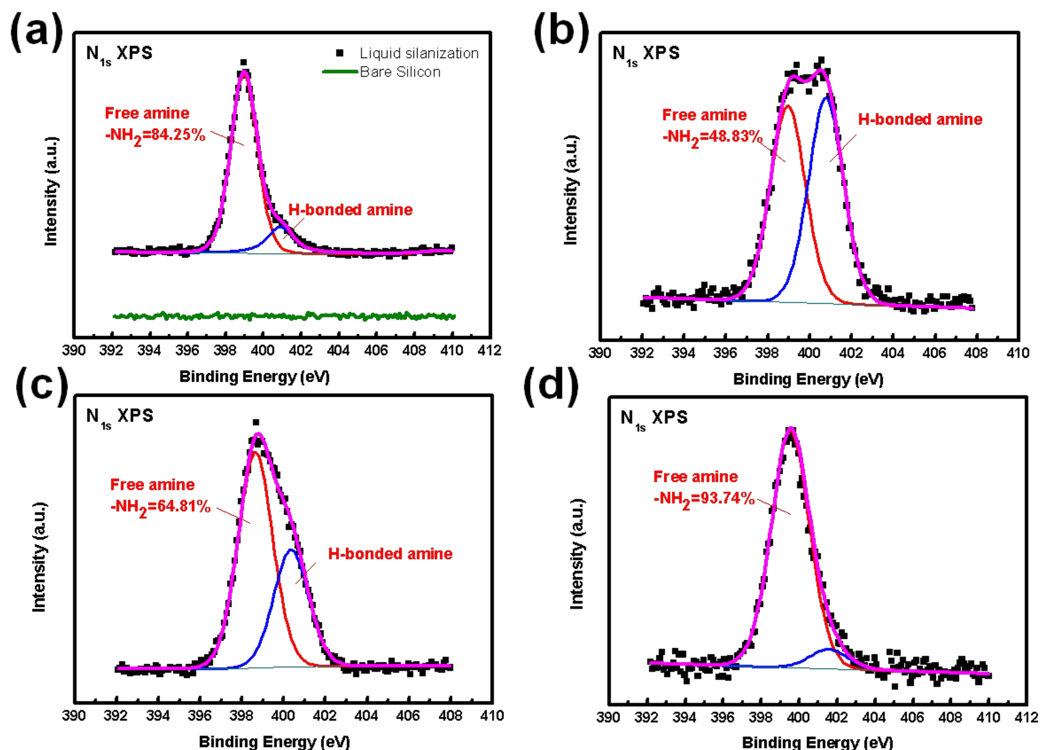

Figure 5-2: High resolution XPS spectra of N_{1s} region for an APTES-silanized silicon surface under different silanization conditions: (a) liquid-silanization in dry toluene for 3mM/3hrs and a control scan on a bare silicon substrate, (b) vapor-silanization using 3% APTES in carrier N_2 gas/ 90 min/110° C, (c) vapor-silanization using 2% APTES in carrier N_2 gas/ 90 min/110° C, (d) vapor-silanization using 2% APTES in carrier N_2 gas/90 min/140° C.

The self-assembly of GO was first evaluated on a blank amine surface prepared by the vapor-silanization of APTES. Figure 5-3 shows the dynamic studies of the coverage rate and the thickness of GO layers measured by AFM and ellipsometry respectively. For the calculation of the surface coverage rate, the “grains” with a 1 nm height threshold (the thickness of a single GO flake) gave a perfect match of the shapes of GO flakes in AFM topography images. For heavily covered surfaces prepared by

longer GO deposition time, it is found that small voids between overlapping flakes were probed as a zero point of height, generating a coverage rate > 99% (last four points in Figure 5-3 (a)). For shorter deposition time, “grains” exactly 1 nm thick are isolated as islands. So it’s clear that GO self-assembled on a vapor-silanized surface can form continuous and overlapped film in 30 minutes. Surprisingly, we also found that the deposition of GO flakes didn’t stop after the surface was fully covered. Figure 5-3 (b) shows that the GO layer kept growing after 30 minutes, and a thickness plateau of around 2 to 2.5 nm was formed after two hours (log scale in x-axis). The saturation thickness corresponds three to five layers of GO.

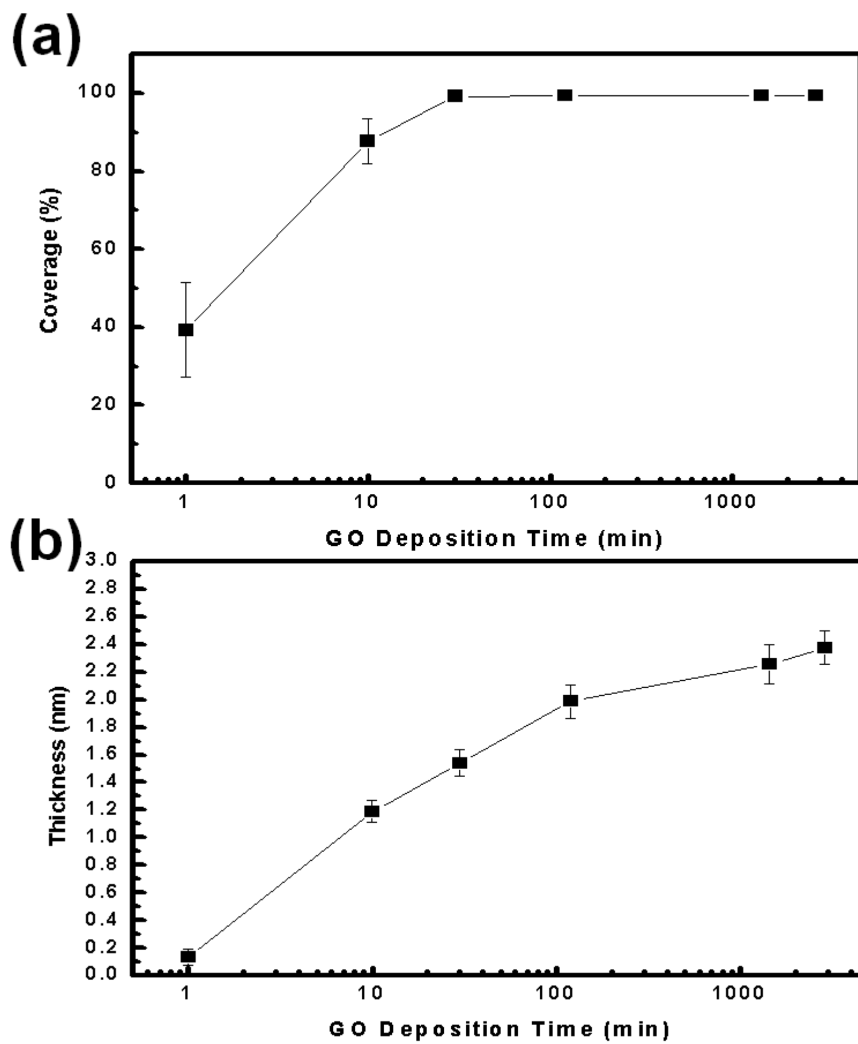

Figure 5-3: (a) Surface coverage rate of GO flakes self-assembled on an APTES vapor-silanized surface calculated from AFM topography images versus GO deposition time. (b) Thickness of GO film self-assembled on an APTES vapor-silanized surface measured by ellipsometry versus GO deposition time.

Graphene oxide is intrinsically insulating and must restore all electronic properties by reduction. A variety of reduction methods (e.g., hydrazine and thermal reduction) have been intensively studied. It is necessary, however, to verify the effect of under-layer APTES. We studied the results of thermal reduction in a hydrogen environment (4% hydrogen in argon, forming gas) by XPS C_{1s} and N_{1s} scans. Samples

bearing GO film self-assembled for 24 hours were annealed at different temperatures for three hours in forming gas. In Figure 5-4 (a), processed GO film shows an oxidized carbon state, such as C-O at ~ 286.3eV, C=O at ~ 287.2eV, and O-C=O at ~ 288.5 eV, as expected. It should be noticed, however, that the intensity of carbon-carbon SP2 (and SP3) (~284.5eV) is much higher than the general C_{1s} spectrum of GO. It is reasonable, because the under-layer APTES contains abundant C-C bonds. In Figure 5-4 (a), two significant trends could be observed when the reduction temperature went higher. First, the intensity of the peaks of oxidized carbon decreases dramatically after annealing at 400° C, followed by a minor decay with rising temperature. It corresponds with literature that most of the oxygen atoms were removed before 400° C[8, 28]. Second, the width of the C_{1s} peak also narrows as the reduction temperature rises until 800° C. Dai et al. have depicted that the width of the C_{1s} peak could be used as an indicator of the change of the C-N peak (285.8eV), which is difficult to precisely de-convolute from the C-C peak[29]. In our case, the C-N peak seems to reach the lowest level after annealing at 800° C. As a matter of fact, the full-width-half-maximum (FWHM) of 800° C-annealed C_{1s} peak is 1.17eV, which matches the reported FWHM of pure GO reduced at 900° C in hydrogen[29]. It indicates that amine is totally decomposed before 800° C. The N_{1s} scans in Figure 5-4 (b) also reveal that no peak shows up after 800° C. This is important for the later study of the n-doping effect in GO. Figure 5-5 shows the AFM topography images of a 24-hr self-assembled GO film before and after 1000° C annealing. The film packs more densely due to the removal of oxygen and water, and the edge of flakes become obscure due to high-temperature graphitization.

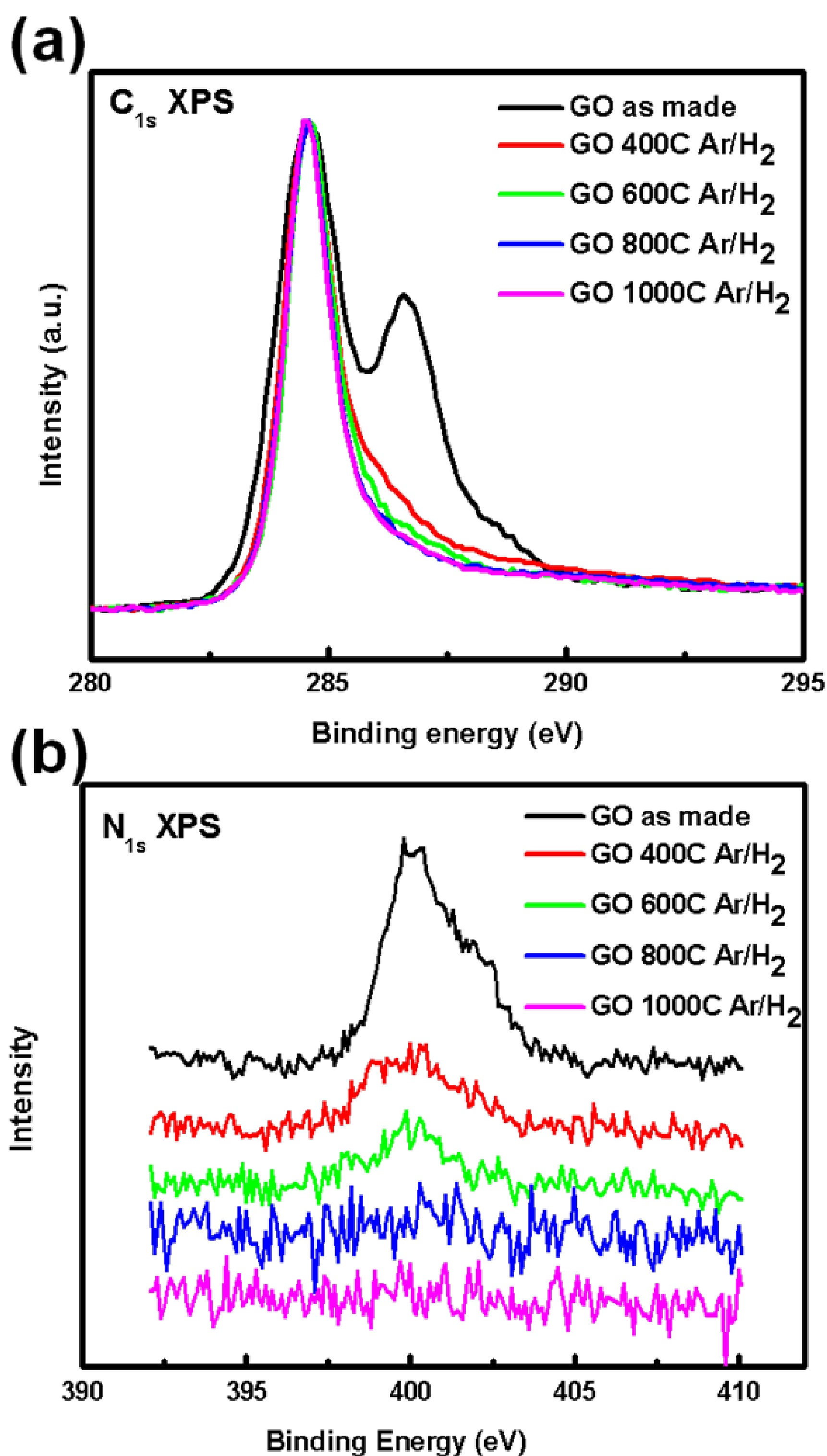

Figure 5-4: High resolution XPS spectra of (a) C_{1s} and (b) N_{1s} region for the 24-hr self-assembled GO films thermally reduced at a different temperature in forming gas.

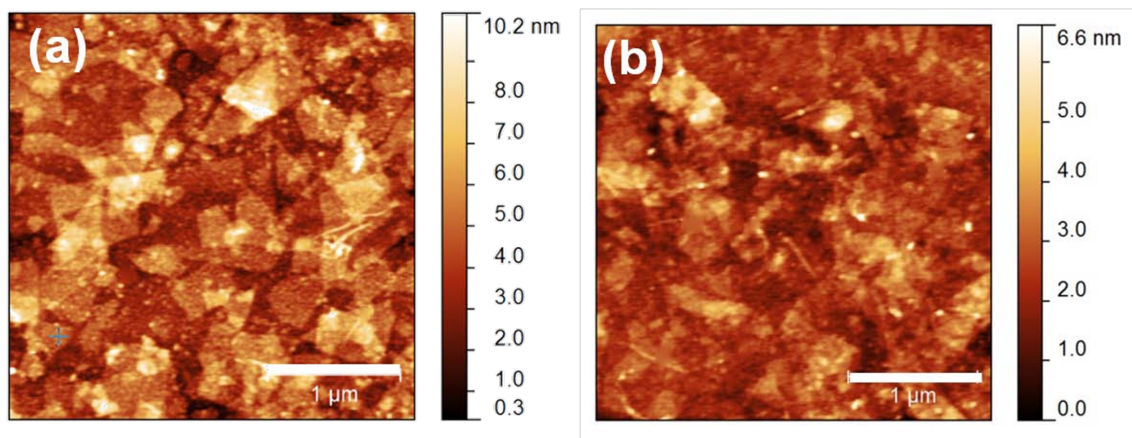

Figure 5-5: AFM topography image of a 24-hr self-assembled GO film: (a) as deposited, (b) after 1000°C reduction in forming gas.

To confirm the electronic properties of self-assembled GO film, we directly patterned and deposited GO on top of pre-evaporated gold source-drain electrodes to make bottom gate/bottom contact organic field-effect transistors (OFETs). Channel length is 50 μm and channel width is 2000 μm. Then GO film was self-assembled and lifted off by the process depicted in Figure 5-1 and covered gold source-drain along with the channel area only in order to prevent current leakage. Figure 5-6 (a) is the optical microscope image of a corner of the 24-hr self-assembled GO pattern after 600°C annealing. The 300nm under-layer oxide is known to improve the contrast and makes single-layer graphene visible. The pattern can be clearly seen and contains around three to five layers of GO from the ellipsometry study in Figure 5-3 (b). Figure 5-6 (b) is the high magnification SEM image of the GO - SiO_2 border. It proves that this self-assembled GO film is continuous, and the overlapping of GO flakes can be clearly seen. A 30-min self-assembled GO device was also made, because the continuous GO film could be as thin as one to two layers according to the AFM and ellipsometry studies. Figure 5-6 (c) is an overview of the channel area of the 30-min self-assembled GO device after 600°C annealing, and Figure 5-6 (d) is the zoomed-in view of the electrode-channel

border. The edges of GO flakes in this ultra-thin film can still be seen, and GO film touches the electrode by a certain extent.

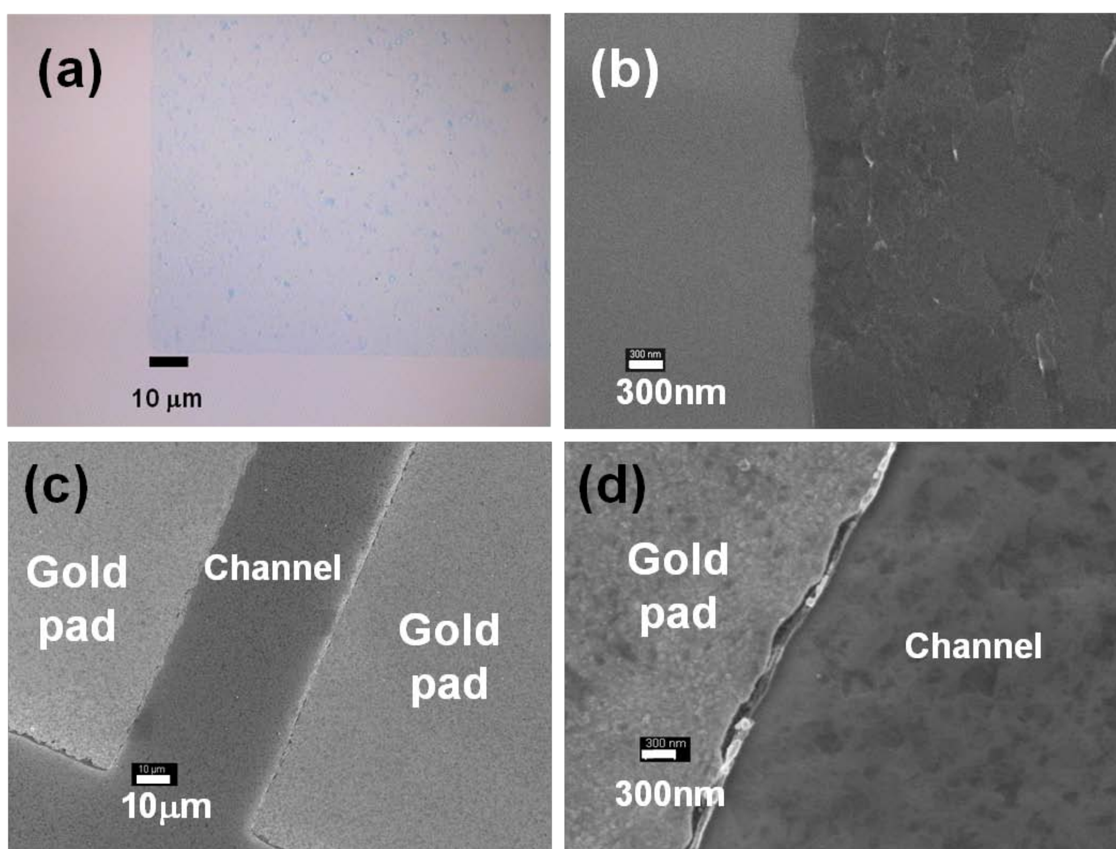

Figure 5-6: (a) Optical microscope image of a corner of the 24-hr self-assembled GO pattern after 600˚C annealing on top of a 300 nm SiO_2 surface. (b) SEM image of a GO - SiO_2 border in (a). (c) SEM overview of the 30-min self-assembled GO film on pre-patterned gold electrodes and channel after 600˚C annealing. (d) Zoom-in of the channel-gold electrode border in (c).

It is known that ultra-thin rGO with one to three layers has semiconducting properties, and thicker ones with over five layers behave more semi-metallic[7, 10]. Figure 5-7 (a) despicts the transfer characteristics of the 24-hr, self-assembled GO device, which contains around five layers of GO flakes after 600˚C annealing. The applied source-drain voltage V_{sd} was 0.1V, and the sheet resistance was measured to be 770,000 Ω/square (by the standard 4-pt probe method). The measurement was performed in ambient air in order to compare with literature. Generally speaking, the whole mobility of rGO thin film in air is between 0.01 to 1 cm^2/V-s for regular GO flakes without any modification[30]. The hole

mobility extracted from our data is 0.2 cm^2/V-s. It also shows p-type semiconductor behavior with a low on/off ratio, which matches with the transfer characteristics of "thicker" rGO film in literature[7]. For the device built by 30-min, self-assembled GO, which contains only one to three layers of GO flakes, a much weaker current was measured but showed an ambipolar and higher on/off ratio (Figure 5-7 (b)). The measurement was performed in a nitrogen environment for the purpose of observing potential ambipolar and deep "V"-shape behavior. The low current is not surprising, because the sheet resistance was measured to be over 2×10^9 Ω/square, a known value for GO down to one nm thick (ref). However, compared to literature, the on/off ratio is still very high. It should be noted that our device is the bottom-contact design. The contact area may not compete with the top-contact device, which was widely used in literature. This might be an explanation for the low current. However, the high on/off ratio and apparent ambipolar behavior still show promising results. As we have known, there are also very few publications that are able to show the high on-off ratio of ultra-thin rGO film. Our result proves that the vapor-silanized APTES layer is capable of forming a continuous GO film within three layers.

One important feature that should be noticed is that the valley points of both curves shift around 20V toward a negative gate voltage, indicating n-doping. For a regular rGO device measured in air, electron transfer is retarded by physisorbed oxygen and water. It shifts the curve toward positive gate voltage and behaves p-doping. For devices measured in nitrogen, the ambipolar curves are always centered at zero-gate voltage[7, 9, 10, 20, 30]. It is well-known that simply by differing the surface condition of gate oxide, such as the hydroxyl group and cleaning method, will alter the doping effect [21, 22]. SAMs with alkyl group, such as OTS and HMDS, have been used to "protect" the surface and avoid interface dipole [21, 31]. Furthermore, SAMs with electron donor, such as F and Cl, have also been proved to p-dope the material [24]. By a different approach, Dai et al. annealed either GO or pristine graphene in amine and successfully generated an n-doping

effect [29, 32]. For APTES, Wang et al. used AFM to measure the surface potential of graphene flakes deposited on an APTES-modified surface [24]. The result also showed an n-doping effect. In this experiment, devices were only annealed at 600 °C. From both the XPS C_{1s} and N_{1s} spectra in Figure 5-4, a certain amount of nitrogen still survived under 600 °C annealing, providing the doping source. This is the first time that the n-doping of rGO by APTES was demonstrated in transfer characteristics.

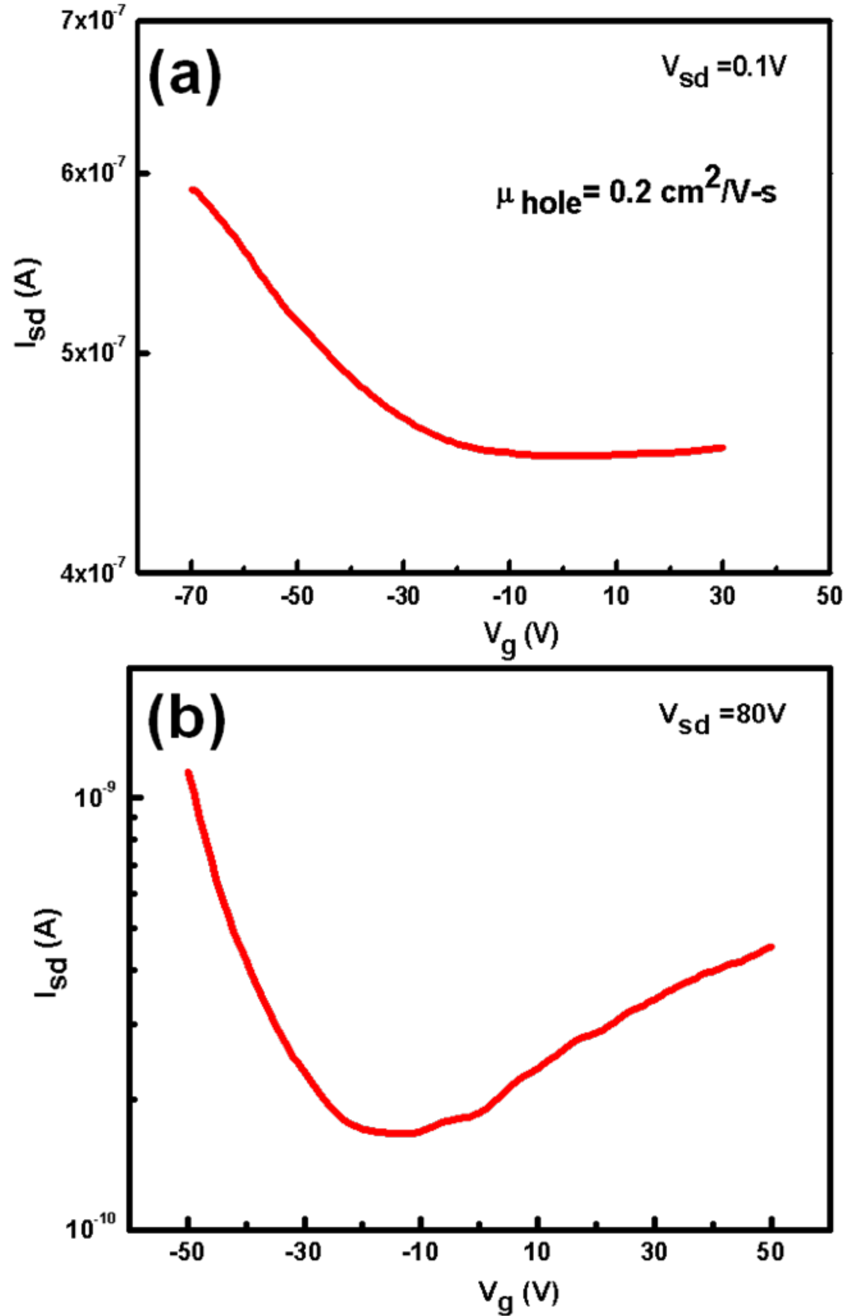

Figure 5-7: (a) Transfer characteristics at a source-drain bias V_{SD}= -0.1V of the 24-hr self-assembled GO OFET with bottom gate, bottom contact (pre-evaporated gold source-drain) annealed at 600°C. (b) Transfer characteristics at a source-drain bias V_{SD}= -80V of the 30-min self-assembled GO OFET with bottom gate, bottom contact (pre-evaporated gold source-drain) annealed at 600°C.

In addition to the sensing application, rGO is also a potential candidate of organic electrode material due to its high conductivity. Both Mullen's group and Bao's group have shown that the OFETs using rGO electrodes generate lower contact resistance for charge injection into the selected organic semiconductors because of the reduction of the dipole barrier and the improvement of 2D morphology by interorganic interfaces[5, 6]. Bao's group also claimed that the combination of GO spin-coating and lift-off on lithographically patterned resist had better resolution and performance in the device. The only concern is how to efficiently deposit a GO film that is thick enough to compensate for thickness loss during reduction and then still have sufficient conductivity to be used as an electrode. Because of the remarkable improvement in 2D morphology of evaporated pentacene on rGO, Bao's group only employed a milder reduction in 400°C and was able to generate a contact resistance 100 times lower then gold electrodes by a 15nm film with $\sigma = 74$ S/cm. For conducting polymer, Mullen's report concluded that a 20nm rGO film with $\sigma = 500$ S/cm is needed to generate higher carrier mobility in P3HT than gold electrodes. So considering the thickness loss during reduction, a coated GO film should be at least 40 nm to generate a usable electrode. On bare substrate, people have to repeat multiple spin-and-bake steps to reach this limit. This increases the operational complexity, and the re-dissolution of the previous layer is always a problem. We attempted to study the effect of APTES modification to GO spin-coating as shown in Figure 5-8. A combined self-assembly and spin-coating process was demonstrated to further increase the thickness in single spin. According to Figure 5-3 (a), a 10-min self-assembly of GO flakes on an APTES-modified surface can afford a nearly fully covered surface. Therefore, we introduced this step before spinning. In other words, GO solution was first applied to cover the APTES-modified substrate for 10 minutes and then started to spin. For control, the same procedure was applied on an oxygen-plasma-treated SiO_2 surface. As shown in Figure 5-8, the result showed higher thickness for each of the GO concentrations. We proposed the coating mechanism as follows: while dropping the GO

solution on an APTES-treated surface, a much higher amount of liquid could be held on the substrate due to the higher contact angle (θ=56°). In the followed step of 10-minute rest, the substrate could be fully covered by a layer of GO flakes, turning the interface condition into more of a GO surface (θ=34°). It is believed that the higher amount of material along with the optimized surface energy (GO spin on GO) contributes to the increase of thickness. For a saturated solution (17mg/ml), the film thickness of a single spin can be improved from 32 nm to 45 nm, sufficient for the electrode application. Figure 5-9 shows the AFM topography images of 45 nm GO film before and after 1000˚C reduction. The typical wrinkle feature of thick GO film can be observed. After 1000˚C graphitization, the film is packed more densely with less roughness.

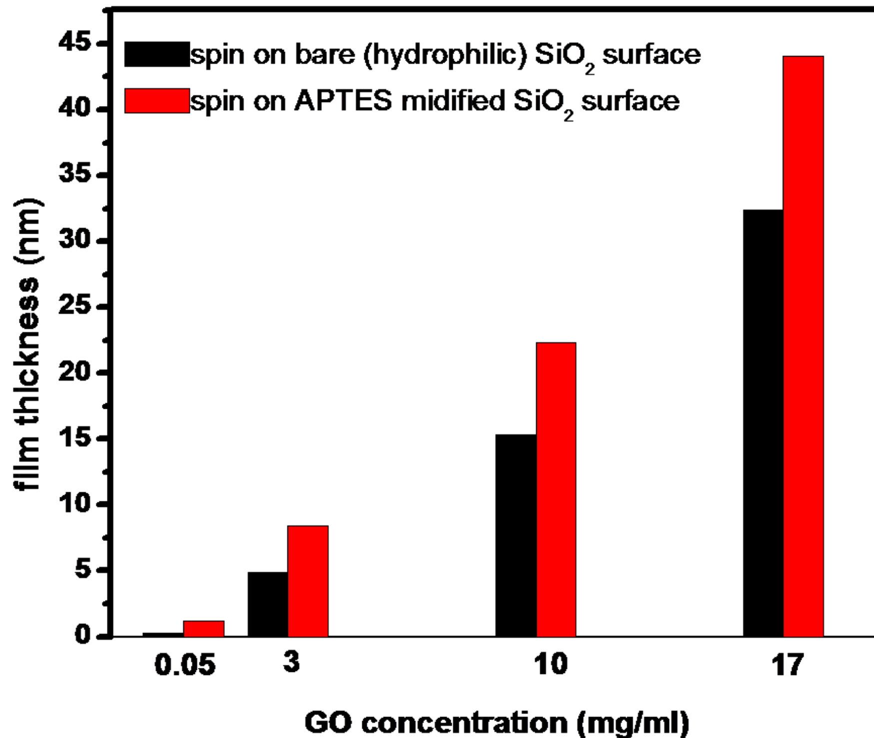

Figure 5-8: Relationship between film thickness and GO concentration in solution for spin-coated, bare SiO_2, or APTES-treated SiO_2 samples (with single spin). Black bar: spin on oxygen-plasma-treated SiO_2 surface (10 minutes after dropping GO solution). Red bar: spin on APTES-treated SiO_2 surface (10 minutes after dropping GO solution).

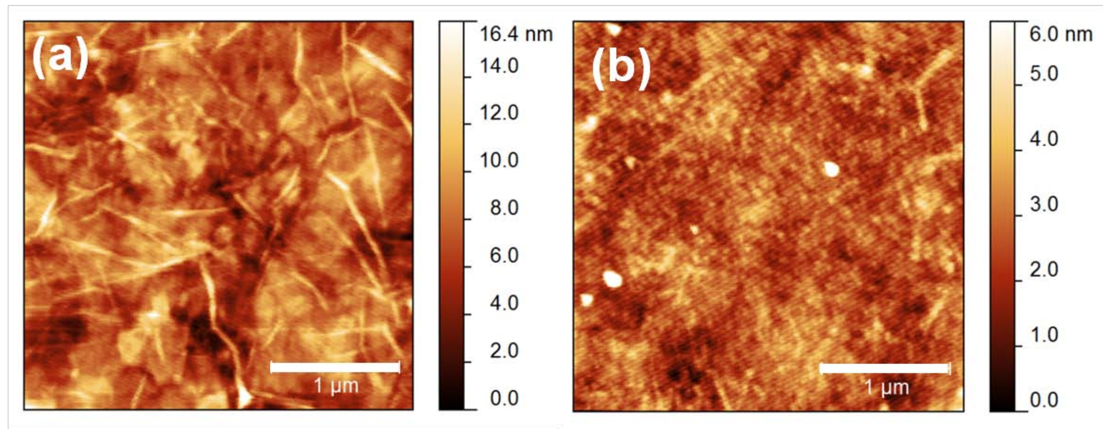

Figure 5-9: AFM topography image of spin-coated 45nm GO film: (a) as deposited, (b) after 1000°C reduction in forming gas.

GO electrode patterns were deposited on a highly doped silicon wafer bearing 300nm of thermally grown oxide by following the procedure depicted in Figure 5-1. A 17 mg/ml GO solution was used to deposit the film. To generate high conductivity, harsh reduction at 1000°C was adopted. Figure 5-10 (a) is the overview SEM image of the source-drain and channel area. Figure 5-10 (b) shows the border of thick rGO film and the channel oxide area. To measure the thickness, AFM was performed across this border as in Figure 5-10 (c) (topography image). The cross-section (shown in Figure 5-10 (d)) shows a sharp edge, implying the potential for high-resolution patterning. As a matter of fact, Bao's report claimed that a minimum pattern of 2 nm could be generated by the lift-off method[6]. The thickness of reduced GO electrode is around 35 nm, which matches the reported 30% thickness loss after 1000°C reduction.

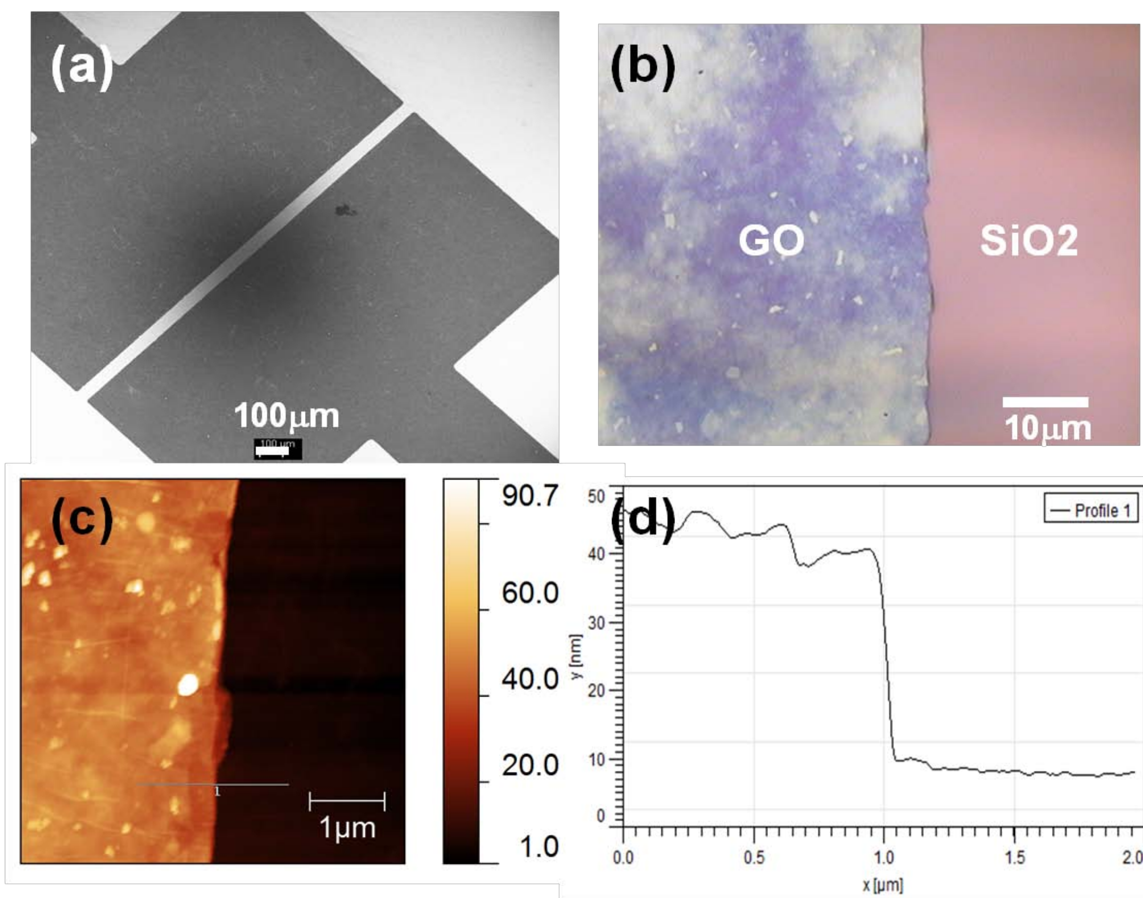

Figure 5-10: (a) SEM overview of patterned GO electrode (after 1000°C reduction in forming gas). (b) Optical microscope image of the border between GO electrode and channel (after 1000°C annealing). (c) AFM topography image of the border between GO electrode and channel (after 1000°C annealing). (d) AFM cross section of line 1 in (c).

To confirm the performance of our GO electrode, P3HT was drop-casted on top of the source-drain area and measured in an ambient environment. The conductivity of electrodes was checked by a standard four-pt probe, giving 285.7 S/cm. The same material was also measured by devices with gold source-drain electrodes in comparison. Figure 5-11 (a) depicts the transfer characteristics of P3HT measured by gold electrodes, and Figure 5-11 (b) depicts the measurements by rGO electrodes. A source-drain voltage of -60V is added, and gate voltage was altered from 0 to -80V. The whole mobility extracted from rGO electrodes is 1.74×10^{-3} $cm^2/V\text{-}s$, which is comparable to that extracted from gold electrodes (1.11×10^{-3} $cm^2/V\text{-}s$). This result also proves that our

"single spin" process with the aid of vapor-silanized APTES is able to provide high-quality rGO electrodes.

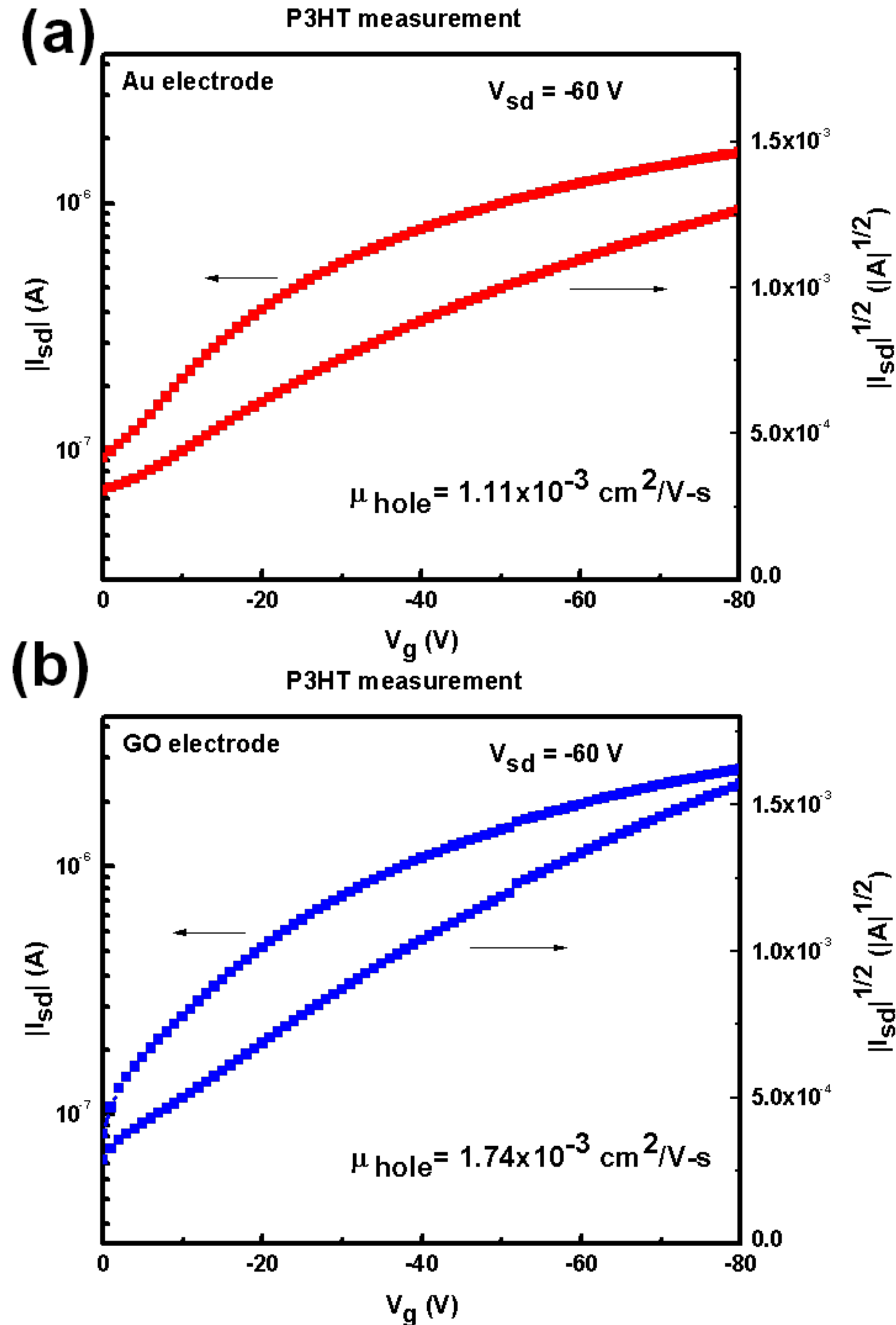

Figure 5-11: (a)Transfer characteristics at a source-drain bias V_{SD}= -60V of P3HT OFET using evaporated 50nm gold S/D electrodes. (b) Transfer characteristics at a source-drain bias V_{SD}= -60V of P3HT OFET employing 35nm thick rGO S/D electrodes annealed at 1000°C.

5.5 Conclusions

To conclude, we have demonstrated a modified lift-off process by the aid of APTES vapor-silanization for building up either a thin rGO sensor or a thick rGO electrode. For APTES vapor-silanization, the XPS result proved that we are able to deposit high-quality APTES from the vapor phase. For the sensing application, OFETs results proved that we can control the GO deposition down to one to three layers by the differentiation of semiconducting and semi-metallic transfer characteristics. The thinnest, fully covered surface by self-assembly of GO flakes was demonstrated. In addition, this is the first time that n-doping from APTES was presented in transfer characteristics. For the organic electrode application, we found that a 10-minute rest prior to spin-coating can effectively increase the GO thickness. We also showed that a 35 nm rGO film deposited by single spin can function well in an organic semiconductor measurement.

5.6 References

1. Lotya, M.; Hernandez, Y.; King, P. J.; Smith, R. J.; Nicolosi, V.; Karlsson, L. S.; Blighe, F. M.; De, S.; Wang, Z. M.; McGovern, I. T.; Duesberg, G. S.; Coleman, J. N., Liquid Phase Production of Graphene by Exfoliation of Graphite in Surfactant/Water Solutions. *Journal of the American Chemical Society* **2009,** *131* (10), 3611-3620.

2. He, Q. Y.; Sudibya, H. G.; Yin, Z. Y.; Wu, S. X.; Li, H.; Boey, F.; Huang, W.; Chen, P.; Zhang, H., Centimeter-Long and Large-Scale Micropatterns of Reduced Graphene Oxide Films: Fabrication and Sensing Applications. *Acs Nano* **2010,** *4* (6), 3201-3208.

3. Jung, I.; Dikin, D. A.; Piner, R. D.; Ruoff, R. S., Tunable Electrical Conductivity of Individual Graphene Oxide Sheets Reduced at "Low" Temperatures. *Nano Letters* **2008,** *8* (12), 4283-4287.

4. Lu, G. H.; Ocola, L. E.; Chen, J. H., Gas detection using low-temperature reduced graphene oxide sheets. *Applied Physics Letters* **2009,** *94* (8), -.

5. Pang, S. P.; Tsao, H. N.; Feng, X. L.; Mullen, K., Patterned Graphene Electrodes from Solution-Processed Graphite Oxide Films for Organic Field-Effect Transistors. *Advanced Materials* **2009,** *21* (34), 3488-+.

6. Becerril, H. A.; Stoltenberg, R. M.; Tang, M. L.; Roberts, M. E.; Liu, Z. F.; Chen, Y. S.; Kim, D. H.; Lee, B. L.; Lee, S.; Bao, Z. A., Fabrication and Evaluation of Solution-Processed Reduced Graphene Oxide Electrodes for p- and n-Channel Bottom-Contact Organic Thin-Film Transistors. *Acs Nano* **2010,** *4* (11), 6343-6352.

7. Eda, G.; Fanchini, G.; Chhowalla, M., Large-area ultrathin films of reduced graphene oxide as a transparent and flexible electronic material. *Nature Nanotechnology* **2008,** *3* (5), 270-274.

8. Mattevi, C.; Eda, G.; Agnoli, S.; Miller, S.; Mkhoyan, K. A.; Celik, O.; Mostrogiovanni, D.; Granozzi, G.; Garfunkel, E.; Chhowalla, M., Evolution of Electrical, Chemical, and Structural Properties of Transparent and Conducting Chemically Derived Graphene Thin Films. *Advanced Functional Materials* **2009,** *19* (16), 2577-2583.

9. Su, C. Y.; Xu, Y. P.; Zhang, W. J.; Zhao, J. W.; Tang, X. H.; Tsai, C. H.; Li, L. J., Electrical and Spectroscopic Characterizations of Ultra-Large Reduced Graphene Oxide Monolayers. *Chemistry of Materials* **2009,** *21* (23), 5674-5680.

10. Wang, S.; Ang, P. K.; Wang, Z. Q.; Tang, A. L. L.; Thong, J. T. L.; Loh, K. P., High Mobility, Printable, and Solution-Processed Graphene Electronics. *Nano Letters* **2010,** *10* (1), 92-98.

11. Li, X. L.; Zhang, G. Y.; Bai, X. D.; Sun, X. M.; Wang, X. R.; Wang, E.; Dai, H. J., Highly conducting graphene sheets and Langmuir-Blodgett films. *Nature Nanotechnology* **2008,** *3* (9), 538-542.

12. Becerril, H. A.; Mao, J.; Liu, Z.; Stoltenberg, R. M.; Bao, Z.; Chen, Y., Evaluation of solution-processed reduced graphene oxide films as transparent conductors. *Acs Nano* **2008,** *2* (3), 463-470.

13. Wei, Z. Q.; Barlow, D. E.; Sheehan, P. E., The Assembly of Single-Layer Graphene Oxide and Graphene Using Molecular Templates. *Nano Letters* **2008,** *8* (10), 3141-3145.

14. Li, H.; Zhang, J.; Zhou, X. Z.; Lu, G.; Yin, Z. Y.; Li, G. P.; Wu, T.; Boey, F.; Venkatraman, S. S.; Zhang, H., Aminosilane Micropatterns on Hydroxyl-Terminated Substrates: Fabrication and Applications. *Langmuir* **2010,** *26* (8), 5603-5609.

15. Allen, M. J.; Tung, V. C.; Gomez, L.; Xu, Z.; Chen, L. M.; Nelson, K. S.; Zhou, C. W.; Kaner, R. B.; Yang, Y., Soft Transfer Printing of Chemically Converted Graphene. *Advanced Materials* **2009,** *21* (20), 2098-2102.

16. Li, B.; Lu, G.; Zhou, X. Z.; Cao, X. H.; Boey, F.; Zhang, H., Controlled Assembly of Gold Nanoparticles and Graphene Oxide Sheets on Dip Pen Nanolithography-Generated Templates. *Langmuir* **2009,** *25* (18), 10455-10458.

17. Fiorilli, S.; Rivolo, P.; Descrovi, E.; Ricciardi, C.; Pasquardini, L.; Lunelli, L.; Vanzetti, L.; Pederzolli, C.; Onida, B.; Garrone, E., Vapor-phase self-assembled monolayers of aminosilane on plasma-activated silicon substrates. *Journal of Colloid and Interface Science* **2008,** *321* (1), 235-241.

18. Hozumi, A.; Yokogawa, Y.; Kameyama, T.; Sugimura, H.; Hayashi, K.; Shirayama, H.; Takai, O., Amino-terminated self-assembled monolayer on a SiO2 surface

formed by chemical vapor deposition. *Journal of Vacuum Science & Technology a-Vacuum Surfaces and Films* **2001,** *19* (4), 1812-1816.

19. Zhang, F.; Sautter, K.; Larsen, A. M.; Findley, D. A.; Davis, R. C.; Samha, H.; Linford, M. R., Chemical Vapor Deposition of Three Aminosilancs on Silicon Dioxide: Surface Characterization, Stability, Effects of Silane Concentration, and Cyanine Dye Adsorption. *Langmuir* **2010,** *26* (18), 14648-14654.

20. Yamaguchi, H.; Eda, G.; Mattevi, C.; Kim, H.; Chhowalla, M., Highly Uniform 300 mm Wafer-Scale Deposition of Single and Multilayered Chemically Derived Graphene Thin Films. *Acs Nano* **2010,** *4* (1), 524-528.

21. Lafkioti, M.; Krauss, B.; Lohmann, T.; Zschieschang, U.; Klauk, H.; von Klitzing, K.; Smet, J. H., Graphene on a Hydrophobic Substrate: Doping Reduction and Hysteresis Suppression under Ambient Conditions. *Nano Letters* **2010,** *10* (4), 1149-1153.

22. Fratini, S.; Guinea, F., Substrate-limited electron dynamics in graphene. *Physical Review B* **2008,** *77* (19), -.

23. Adam, S.; Hwang, E. H.; Galitski, V. M.; Das Sarma, S., A self-consistent theory for graphene transport. *Proceedings of the National Academy of Sciences of the United States of America* **2007,** *104* (47), 18392-18397.

24. Wang, R.; Wang, S. N.; Zhang, D. D.; Li, Z. J.; Fang, Y.; Qiu, X. H., Control of Carrier Type and Density in Exfoliated Graphene by Interface Engineering. *Acs Nano* **2010,** *5* (1), 408-412.

25. Kovtyukhova, N. I.; Ollivier, P. J.; Martin, B. R.; Mallouk, T. E.; Chizhik, S. A.; Buzaneva, E. V.; Gorchinskiy, A. D., Layer-by-layer assembly of ultrathin composite films from micron-sized graphite oxide sheets and polycations. *Chemistry of Materials* **1999,** *11* (3), 771-778.

26. Hummers, W. S.; Offeman, R. E., Preparation of Graphitic Oxide. *Journal of the American Chemical Society* **1958,** *80* (6), 1339-1339.

27. Zhang, F. X.; Srinivasan, M. P., Self-assembled molecular films of aminosilanes and their immobilization capacities. *Langmuir* **2004,** *20* (6), 2309-2314.

28. Yang, D.; Velamakanni, A.; Bozoklu, G.; Park, S.; Stoller, M.; Piner, R. D.; Stankovich, S.; Jung, I.; Field, D. A.; Ventrice, C. A.; Ruoff, R. S., Chemical analysis of graphene oxide films after heat and chemical treatments by X-ray photoelectron and Micro-Raman spectroscopy. *Carbon* **2009,** *47* (1), 145-152.

29. Li, X. L.; Wang, H. L.; Robinson, J. T.; Sanchez, H.; Diankov, G.; Dai, H. J., Simultaneous Nitrogen Doping and Reduction of Graphene Oxide. *Journal of the American Chemical Society* **2009,** *131* (43), 15939-15944.

30. Jeong, S. Y.; Kim, S. H.; Han, J. T.; Jeong, H. J.; Yang, S.; Lee, G. W., High-Performance Transparent Conductive Films Using Rheologically Derived Reduced Graphene Oxide. *Acs Nano* **2011,** *5* (2), 870-878.

31. Lin, Y. Y.; Gundlach, D. J.; Nelson, S. F.; Jackson, T. N., Stacked pentacene layer organic thin-film transistors with improved characteristics. *Ieee Electron Device Letters* **1997,** *18* (12), 606-608.

32. Wang, X. R.; Li, X. L.; Zhang, L.; Yoon, Y.; Weber, P. K.; Wang, H. L.; Guo, J.; Dai, H. J., N-Doping of Graphene Through Electrothermal Reactions with Ammonia. *Science* **2009,** *324* (5928), 768-771.

CHAPTER 6

SELECTIVE SELF-ASSEMBLY OF GOLD NANOPARTICLES ON MONOLAYER PATTERNS ACTIVATED BY THERMOCHEMICAL NANOLITHOGRAPHY

Thermochemical nanolithography, which in this case involves use of a heated nanoprobe to pattern a protected reactive self-assembled monolayer (SAM), is used to perform controlled patterning and assembly of gold nanoparticles (AuNPs). The SAM used was a THP-protected thiol-functionalized triethoxysilane. When the cantilever heater was operated at 360°C (corresponding to a surface temperature of approximately 200°C), negative tone AuNP assemblies were formed through local SAM deprotection followed by solution deposition of AuNPs. When the cantilever heater was operated at 560°C (corresponding to a tip temperature of approximately 290°C), the SAM was ablated to produce positive tone AuNP features. We show AuNP features ranging from large densely covered squares to single particle wide lines and features. This method can be performed on a wide variety of substrates, e.g. including a range of metal oxide surfaces using the silane surface coupling functionalized SAMs reported here, by simply choosing an appropriate surface reactive group for the SAM layer.

6.1 Introduction

Thermochemical nanolithography (TCNL)[1-5] allows for physical and chemical patterning of surfaces with nanometer scale precision using a heated cantilever probe[6]. A resistive heating element integrated into an atomic force microscope (AFM) cantilever can perform ultra-fast heating of the probe tip up to temperature above 1050 ºC[7]. The hot spot created by a heated cantilever can be as small as 2 nm and the temperature of the substrate can easily be heated to over 500 ºC at the tip-substrate contact[8]. Unlike other

previous scanning probe lithography methods, TCNL can pattern samples using a combination of chemical and mechanical modification and can serve to produce a wider variety of pattern types for a broader range of potential applications. TCNL has the advantages of very fast writing speeds, the ability to use a single tip type for all materials, no significant substrate limitations, and fast dynamic on-off switching of the writing process (i.e. ~ 10μs modulation is possible[7, 8]) without disengaging the tip from the surface to modulate the writing process. A variety of material patterning methods have been demonstrated using such a heated nanoprobe including: (1) sculpting of polymer films and surfaces in three dimensions[2, 3], (2) selective modification of the surface chemistry of polymer films[1, 3-5], and (3) the use of such sculpted and surface modified patterns to guide the further growth (e.g. by ALD) or deposition (e.g. adsorption of proteins from solution) of materials onto these patterns[5].

More recently, it has been of interest to investigate the use of TCNL methods to develop directed assembly approaches such as using patterns generated by the tip to guide the assembly of nanoparticles onto a surface. The selective self-assembly of AuNPs has been applied to advanced electro-optical devices[9] and to form metal seeds/catalysts for other subsequent processes (e.g. electroless plating of nanostructures[10]). Owing to the wide interest in AuNPs and assemblies of AuNPs, a direct method for controlled patterning of AuNPs has been developed in this work. This method combines: (1) the synthesis and immobilization of a protected reactive self-assembled monolayer (SAM), (2) local selective thermal decomposition of the protecting functional group on the SAM or thermal ablation of the SAM from the surface by TCNL, and (3) the synthesis and selective immobilization of AuNPs on the patterned SAM. Using this approach, lines and arbitrary patterns of ranging from very large features to single particle wide structures can be fabricated on a wide variety of surfaces.

6.2 Experimental

It is well known that the thiol (-SH) group can form a covalent bond with gold. Therefore methods that produce thiol functional groups locally on a surface can enable the selective deposition of AuNPs[11]. For this purpose, a protected 3-mercaptotriethoxysilane (MPTES) SAM was chosen for this application. Tetrahydropyran (THP) has been widely used as the protecting group for alcohols in organic synthesis and chemically amplified resists[12], and deprotection of this group can be triggered by either acidic hydrolysis or heat treatment at moderate temperatures (i.e. approximately 150°C to 200°C not in the presence of acid and as low as 50°C in the presence of acid). Since THP can also be reacted to protect thiol groups[13], in this work THP protected MPTES has been used as a thermally switchable surface thiol generator using probe tip based thermal deprotection. Figure 6-1 shows a schematic of the entire process. First, THP protected MPTES was synthesized by a one step reaction of 3,4-dihydro-2H-pyran with MPTES in anhydrous dichloromethane with a catalytic amount of pyridinium p-toluenesulfonate (PPTS). Second, 5mM THP-MPTES in dry toluene solution was prepared to perform the surface modification. Hydroxylated silicon wafers were immersed in the THP-MPTES solution for 16 hours to form a SAM surface monolayer[14]. Local thermal writing was performed using a heated cantilever probe under normal contact mode AFM conditions. Thermal deprotection of the THP-MPTES followed by direct exposure to AuNPs was found to result in poor coupling of the AuNPs to the surface (i.e. very little difference between non-specific AuNP deposition on both silicon control and protected SAM surfaces as compare to the thermally deprotected surfaces could be observed), consistent with previous reports that such protected thiols readily form disulfide bonds upon thermal deprotection[11, 15] Therefore, reduction of the thermally deprotected SAM pattern by immersion in 1% DL-dithiothreitol (DTT) solution for 3 hours was performed to ensure production of the desired thiol surface patterns. After reduction, the patterned SAM coated silicon substrates were immersed in a

AuNP solution in water for another 24 hours to selectively immobilize AuNPs on the thiol groups exposed by the patterned thermal deprotection, and finally washed in deionized water. The AuNPs used in this work were made by the citrate reduction of $HAuCl_4$ using standard techniques reported in literature[16]. The absorption peak maximum of the nanoparticles made in this work was at 520 nm, corresponding to an average AuNPs diameter of 10 nm which was also confirmed by TEM analysis.

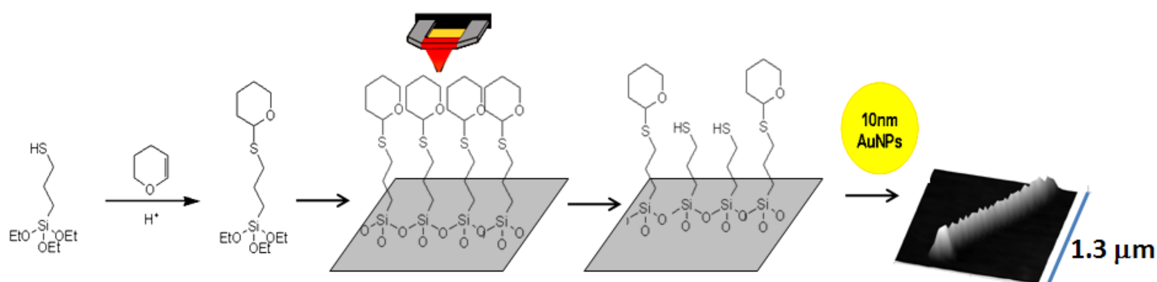

Fig. 6-1: Scheme of this work. (a) Synthesis of THP-MPTES SAM. (b) Surface modification of silicon substrate. (c) Local thermal decomposition of THP protecting group. (d) Selective self-assembly of 10nm AuNPs

6.3 Results and Discussion

In order to develop initial estimates of the proper thermal writing conditions for the THP-MPTES SAM monolayers, the thermal behavior of THP-MPTES was first characterized by a thermogravimetric analysis system (TGA) coupled to a mass spectrometer (Pfeiffer GSD301C) using standard room air as the purge gas. To produce samples for TGA analysis in a manner that would somewhat simulate the SAM conditions on a silicon oxide surface, water was added to the THP-MPTES solution in order to hydrolyze and condense the reactive triethoxysilane end groups on the SAM compound. The cross-linked THP-MPTES gel was collected after centrifugation at 10,000rpm for 10 min from the solution and then loaded in the TGA. Fig. 6-2 (a) shows the ion current of expected major product species that show some change in ion current as a function of temperature, and the ramping rate here is 5° C/min. First, the 84 amu

signal, which according to the decomposition mechanism of THP protected compounds should correspond to the known dihydropyran byproduct of the deprotection reaction[17], shows apparent onset of deprotection above approximately 150 ºC with high rates of decomposition occurring above 200 ºC. Thus, as a first good estimate it was assumed that probe tip temperatures which heated the sample surface above approximately 200 ºC should be sufficient to demonstrate good local deprotection and writing of a thiol pattern on the SAM. Upon further heating, the ion current level of a 64 amu species elevates at temperatures above approximately 270 ºC. This 64 amu species is assumed to be SO_2 formed from decomposition and oxidation of the thiol end group of the SAM[18]. It appears that the C-S bond cleavage and oxidation of the sulfur is the major reaction on the SAM under an oxygen containing atmosphere in this temperature range. This is reasonable given that the carbon-sulfur bond dissociation energy (259kJ/mol) would indicate that it is a significantly weaker bond in MPTES as compared to the C-C bonds (347 kJ/mol) in the alkyl spacer. These TGA decomposition temperature results were further verified using both contact angle and particle deposition tests. Static water contact angles were measured for THP-MPTES monolayers grown on silicon oxide substrates after hot plate heating for 10 minutes over a range of temperatures from 50ºC to 300ºC. Figure 6-2 (b) shows the contact angle of the SAM coated silicon surface as a function of bake temperature. The water contact angle on the THP-MPTES modified surface began to noticeably decrease at temperatures above approximately 150ºC. This decrease in contact angle is consistent with the expected loss of the THP protecting group and the production of thiol or disulfide bonds. For baking temperatures above 210ºC, the water contact angle decreases further until it reaches a value of roughly 10º at temperatures above ~290ºC. This further reduction of contact angle is likely due to the onset of C-C bond cleavage, oxidation of the carbon backbone, and the production of more hydrophilic species such as carboxylic acids, etc. This observed behavior is similar to and consistent with that reported previously for the thermal decomposition behavior of octadecyltrichlorosilane

(OTS) SAM coatings[19]. AuNP deposition experiments were also performed on sample coupons coated with the SAM that were baked on a hotplate for 10 minutes over the same range of temperatures used in the contact angle study, treated in DTT, and then immersed in the AuNP solution for 24 hours. As shown in the AFM picture insets of these samples in Fig. 6-2 (b), samples baked at 210ºC (with a corresponding water contact angle of 36º) yielded a surface densely covered by AuNPs after exposure to AuNP solution and washing. This is consistent with the previous tests that suggest that extensive deprotection of the THP-MPTES surface has occurred at this temperature without causing any significant degradation of the thiol end group. On the other hand, virtually no particle deposition is observed on samples baked up to temperature of ~100ºC, and only sporadic particle coverage is observed in samples baked at 150ºC. For samples heated above 230ºC, the density of particle deposition on the surface decreased with increasing baking temperature until again virtually no AuNPs are observed on samples baked at 290ºC and above, further reinforcing the idea that loss of the thiol group occurs if the thermal treatment temperature is taken too high. These results suggested a likely range of target surface writing temperatures between roughly 150ºC and 250ºC over which to conduct TCNL pattern writing experiments.

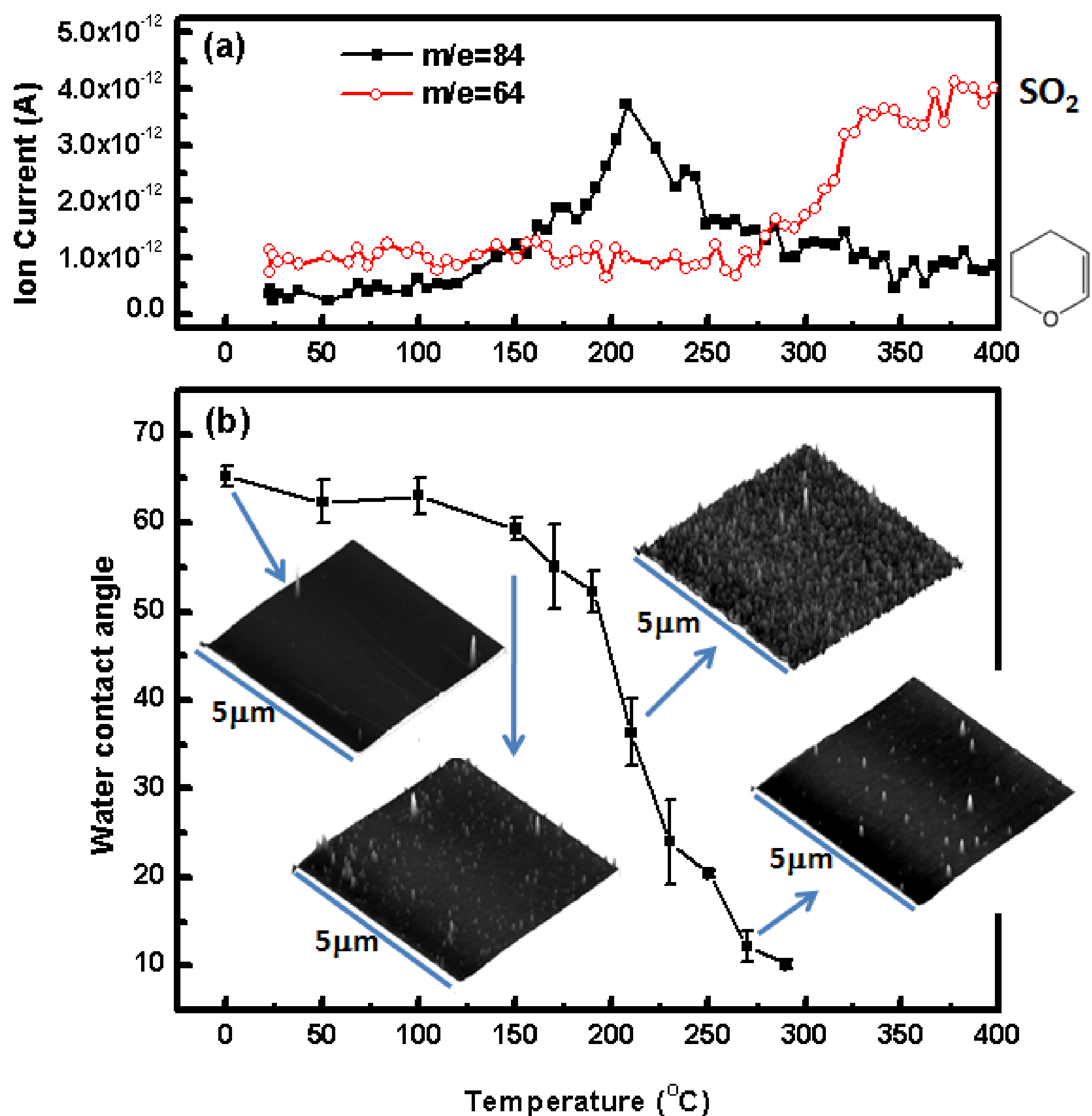

Fig. 6-2: (a) Thermal mass spectrum of hydrolyzed THP-MPTES. Ramping rate is 5° C/sec. The two major species here are m/e=84 (dihydropyran) and 64 (sulfur dioxide). (b) Static water contact angle of THP-MPTES modified silicon oxide substrate after hot plate baking. Insets are the AFM topography images of same sample after AuNPs deposition.

Thermal writing was performed in an ambient environment using an Agilent PicoPlus AFM system configured with a custom thermal cantilever and voltage control circuit. Contact mode scanning with the same force load as used for imaging was employed for the writing experiments. The temperature versus voltage calibration for the thermal cantilever was obtained through Raman thermometry for each cantilever tip used in the experiments to ensure accurate temperature control and reporting[20]. The ratio of temperature drop between calibrated cantilever heater and the tip-surface interface was determined by detecting the onset temperature of the wavelength increase of scan and heat-induced ripples, which indicates the glass transition temperature, on polymers with known Tg. A ratio of 0.4 - 0.6 between the tip contact point and the cantilever heater was reported[4, 21, 22]. A steady-state simulation calculating the integrated thermal resistance of tip, contact, and substrate also indicates that for loading force 50nN and a tip radius of 20nm, a cantilever heater temperature of 350° C is required to make contact temperature reach 210° C[23]. For imaging of the samples, the same thermal cantilever was used to characterize the friction difference across the surface right after thermal writing in order to image the written pattern in the SAM itself, while regular tapping mode tip was used to image the AuNPs patterns in order to produce high resolution images with minimal disturbance of the patterned features. High quality writing results thus were expected to be obtained using a cantilever heater temperature in the range of 360ºC since the best quality particle deposition was obtained at a baking temperature of approximately 210ºC in the earlier blanket AuNP deposition experiments.

Studies were performed to further probe and refine the proper writing temperature for the THP-MPTES SAM patterning. A series of 1μm by 1μm squares were written at different temperatures using a 1.5 Hz scan frequency (i.e. corresponding to a 3 μm/s writing speed) and 128 pixel resolution. Fig. 6-3 (a) is the friction image of square written using a cantilever heater temperature of 360ºC taken right after thermal writing. The surface energy difference between the protected and deprotected THP-MPTES SAM

results in the friction change and thus the friction image of the square, confirming that a chemical pattern is induced in the SAM at this writing temperature. Fig. 6-3 (b) shows the results for the array of squares after writing, DTT treatment, and immersion in AuNP solution. At low cantilever temperatures (<280 ºC), the SAM appears to be relatively unaffected and no significant AuNP deposition is observed on the surface. At intermediate cantilever temperatures (~320ºC to ~440ºC), the SAM is deprotected and the resulting pattern clearly guides the capture and assembly of AuNPs. At high temperatures (>440 ºC), the SAM loses its ability to capture particles and again little to no particle deposition is observed which is consistent with thermal decomposition and ablation of the SAM. The fact that AuNPs only appear in a certain writing temperature range is consistent with our macroscopic bulk sample studies and the optimum writing temperature for the 3 μm/s writing speed used appears to be in the range of 360ºC to 400 ºC, again consistent with our expectations from the bulk experiments and thermal simulations.

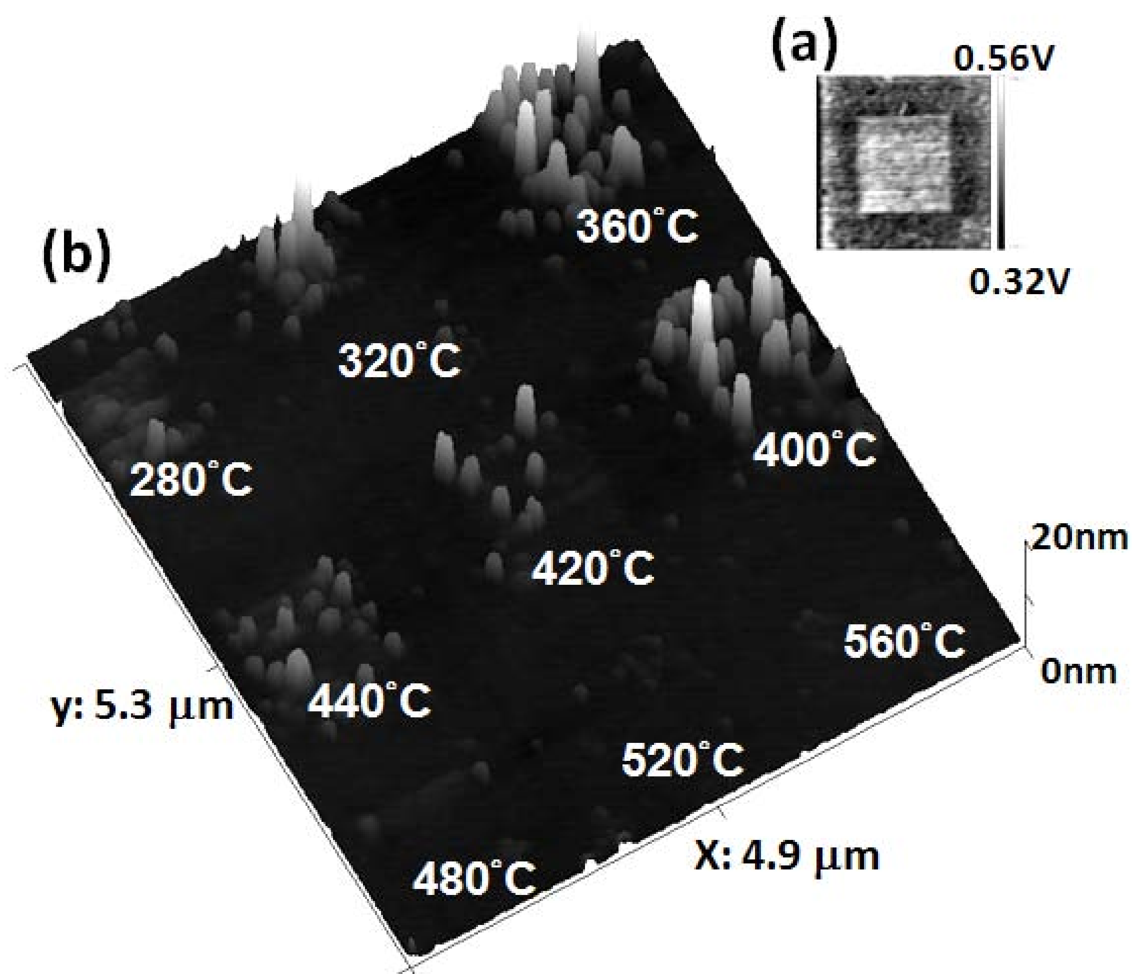

Fig. 6-3: Topography and friction images of THP-MPTES SAM modified silicon substrate after TCNL. (a) Friction image of 360 ºC area after thermal writing and before AuNPs deposition. (b) Topography image of nine 1μm squares written in different temperature after AuNPs deposition. The scan frequency is 1.5 Hz and resolution is 128 pixels. The size of gold nanoparticles is around 10nm and can not be resolved well by the AFM tip used here (The radius of curvature of this tip is larger than 10nm), which makes the AuNPs deposited area looks more like aggregated clusters.

A variety of features were then thermally patterned onto THP-MPTES SAM coated surfaces using a cantilever temperature of 360 ºC (see Fig. 6-4). For square patterns (see Fig. 6-4 (a) and 6-4 (b)), sparse AuNP deposition was observed in a 2 µm square written at 1.5Hz (i.e. equating to a 6µm/s writing speed). This indicates that scan speed plays an important role in addition to temperature in terms of controlling the quality and extent of the deprotection pattern written into the SAM, and the 6 µm/s scan speed is too fast when using the 360ºC cantilever temperature to achieve dense patterns. In contrast, writing at the same 1.5 Hz frequency in 0.5 µm square (1.5 µm/s writing speed) again generates a densely covered AuNPs square feature. Fig. 6-4 (c) shows an attempt to write a single particle wide AuNP line using a single pass of a 360 ºC heated cantilever at a writing speed of 1.5 µm/s. Imaging of the line does in fact appear to show a nanoparticle line that is only one particle wide, confirming the ability of the technique to produce features which are limited ultimately by the size of the AuNPs. Such a local confinement of the temperature rise under the tip-substrate contact point and the resulting high resolution chemical patterning of the surface is consistent with previous reports of the expected temperature profiles in the vicinity of the tip-substrate contact point[23]. Positive tone particle patterning using the same THP-MPTES SAM and heated probe is also easily accessible using these methods. Fig. 6-4 (d) shows a positive tone AuNP pattern formed by thermal ablation of a line in the SAM using a cantilever temperature of 600ºC followed by blanket thermal deprotection of the remaining substrate on a hotplate, followed by DTT treatment and immersion in AuNP solution. It is thus clear that a wide range of AuNP patterns can easily be achieved with high pattern resolution using combinations of thermal writing to generate deprotected SAM patterns, thermal writing to ablate the SAM, and uniform baking of the substrate to drive deprotection or ablation of the SAM. It is easy to envision using a sequence of such processes to deposit very complex nanoparticle assemblies consisting of particles of both different sizes and potentially different chemical compositions.

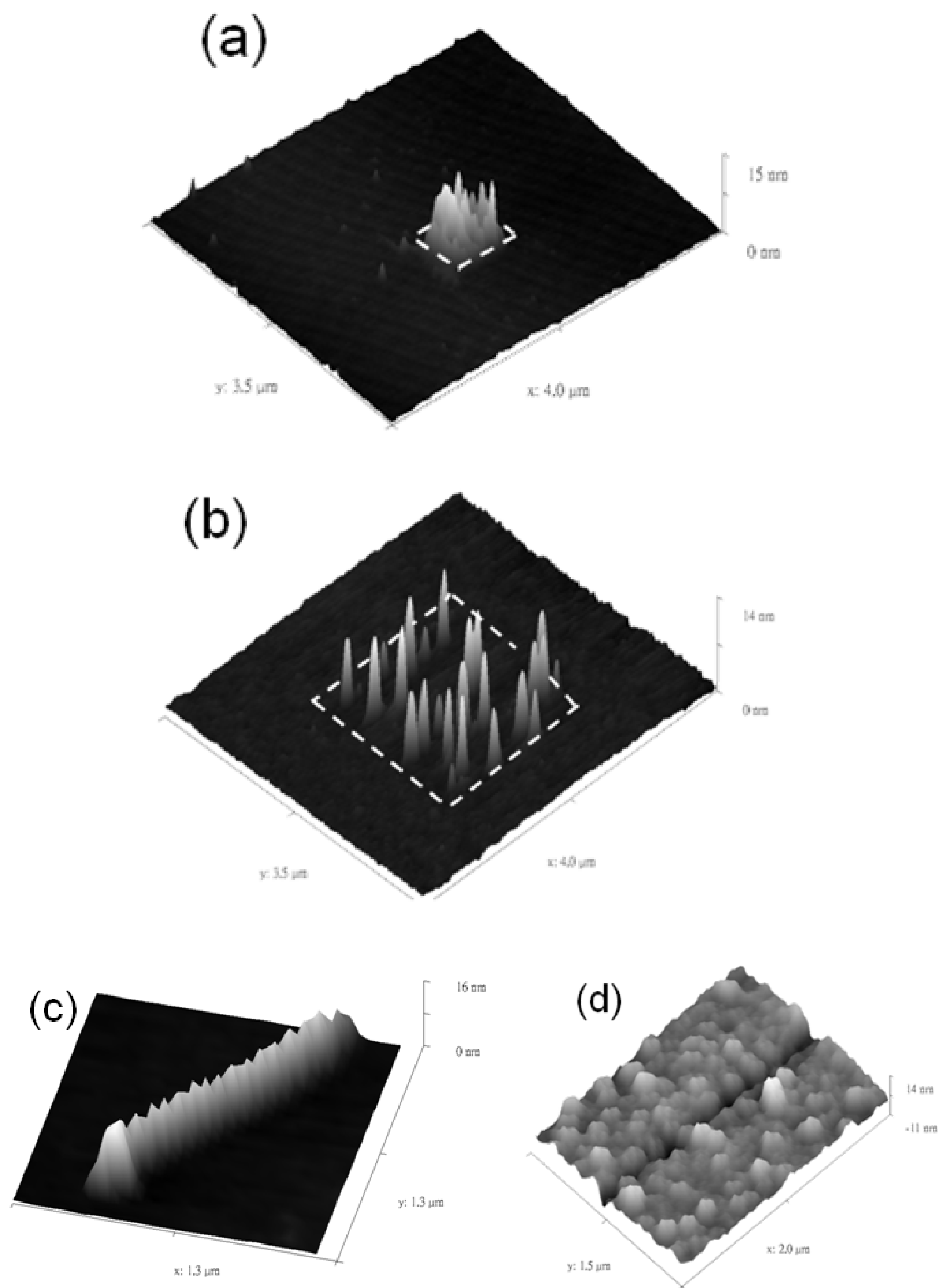

Fig. 6-4: A variety of AuNPs patterns generated by thermal writing. (a) 0.5µm square with 360 ºC, 1.5Hz scan frequency (1.5µm/s). (b) 2 µm square with 360 ºC, 1.5Hz scan frequency (6µm/s, AuNPs cannot fully cover the area due to high scan speed). (c) Straight AuNPs line with single particle in width (360 ºC, 1.5µm/s). (d) Postive tone line pattern (560 ºC, 1.5µm/s).

6.4 Conclusions

In summary, the selective activation of a protected THP-MPTES SAM using TCNL has been demonstrated and the use of such patterned SAMs to guide the assembly of gold nanoparticles has been successfully achieved. At a writing speed of 1.5 μm/s, cantilever temperatures in the range of 360 ºC to 400 ºC deprotect the THP-MPTES and the resulting patterns can be used to form negative tone AuNP patterns. Writing using cantilever temperatures above 560 ºC can cleanly thermally ablate the THP-MPTES SAM and can be generate positive tone AuNP patterns.

6.5 References

1. Szoszkiewicz, R.; Okada, T.; Jones, S. C.; Li, T. D.; King, W. P.; Marder, S. R.; Riedo, E., High-speed, sub-15 nm feature size thermochemical nanolithography. *Nano Letters* **2007,** *7* (4), 1064-1069.

2. Gotsmann, B.; Duerig, U.; Frommer, J.; Hawker, C. J., Exploiting chemical switching in a Diels-Alder polymer for nanoscale probe lithography and data storage. *Advanced Functional Materials* **2006,** *16* (11), 1499-1505.

3. Hua, Y. M.; Saxena, S.; Clifford, H.; King, W. P., Nanoscale thermal lithography by local polymer decomposition using a heated atomic force microscope cantilever tip. *Journal of Micro-Nanolithography Mems and Moems* **2007,** *6* (2), -.

4. Wang, D. B.; Szoszkiewicz, R.; Lucas, M.; Riedo, E.; Okada, T.; Jones, S. C.; Marder, S. R.; Lee, J.; King, W. P., Local wettability modification by thermochemical nanolithography with write-read-overwrite capability. *Applied Physics Letters* **2007,** *91* (24), -.

5. Hua, Y. M.; King, W. P.; Henderson, C. L., Nanopatterning materials using area selective atomic layer deposition in conjunction with thermochemical surface modification via heated AFM cantilever probe lithography. *Microelectronic Engineering* **2008,** *85* (5-6), 934-936.

6. Vettiger, P.; Despont, M.; Drechsler, U.; Durig, U.; Haberle, W.; Lutwyche, M. I.; Rothuizen, H. E.; Stutz, R.; Widmer, R.; Binnig, G. K., The "Millipede" - More than one thousand tips for future AFM data storage. *Ibm Journal of Research and Development* **2000,** *44* (3), 323-340.

7. Lee, J.; Beechem, T.; Wright, T. L.; Nelson, B. A.; Graham, S.; King, W. P., Electrical, thermal, and mechanical characterization of silicon microcantilever heaters. *Journal of Microelectromechanical Systems* **2006,** *15* (6), 1644-1655.

8. Park, K.; Cross, G. L. W.; Zhang, Z. M. M.; King, W. P., Experimental investigation on the heat transfer between a heated microcantilever and a substrate. *Journal of Heat Transfer-Transactions of the Asme* **2008,** *130* (10), -.

9. Wuelfing, W. P.; Murray, R. W., Electron hopping through films of arenethiolate monolayer-protected gold clusters. *Journal of Physical Chemistry B* **2002,** *106* (12), 3139-3145.

10. Niidome, Y.; Urakawa, S.; Kawahara, M.; Yamada, S., Dichroism of poly(vinylalcohol) films containing gold nanorods induced by polarized pulsed-laser irradiation. *Japanese Journal of Applied Physics Part 1-Regular Papers Short Notes & Review Papers* **2003,** *42* (4A), 1749-1750.

11. Fresco, Z. M.; Frechet, J. M. J., Selective surface activation of a functional monolayer for the fabrication of nanometer scale thiol patterns and directed self-assembly of gold nanoparticles. *Journal of the American Chemical Society* **2005,** *127* (23), 8302-8303.

12. Hayashi, N.; Hesp, S. M.; Ueno, T.; Toriumi, M.; Iwayanagi, T.; Nonogaki, S., *Polymeric Materials Science and Engineering* **1989,** *61*, 417.

13. Kipnis, F.; Ornfelt, J., 2-Substituted Tetrahydropyranyl Sulfides. *Journal of the American Chemical Society* **1951,** *73* (2), 822-822.

14. Hu, M. H.; Noda, S.; Okubo, T.; Yamaguchi, Y.; Komiyama, H., Structure and morphology of self-assembled 3-mercaptopropyltrimethoxysilane layers on silicon oxide. *Applied Surface Science* **2001,** *181* (3-4), 307-316.

15. Pavlovic, E.; Quist, A. P.; Gelius, U.; Nyholm, L.; Oscarsson, S., Generation of thiolsulfinates/thiolsulfonates by electrooxidation of thiols on silicon surfaces for reversible immobilization of molecules. *Langmuir* **2003,** *19* (10), 4217-4221.

16. Freund, P. L.; Spiro, M., Colloidal Catalysis - the Effect of Sol Size and Concentration. *Journal of Physical Chemistry* **1985,** *89* (7), 1074-1077.

17. Hesp, S. A. M.; Hayashi, N.; Ueno, T., Tetrahydropyranyl-Protected and Furanyl-Protected Polyhydroxystyrene in Chemical Amplification Systems. *Journal of Applied Polymer Science* **1991,** *42* (4), 877-883.

18. Wu, Z. L.; Ondruschka, B.; Stark, A., Ultrasonic cleavage of thioethers. *Journal of Physical Chemistry A* **2005,** *109* (16), 3762-3766.

19. Kim, H. K.; Lee, J. P.; Park, C. R.; Kwak, H. T.; Sung, M. M., Thermal decomposition of alkylsiloxane self-assembled monolayers in air. *Journal of Physical Chemistry B* **2003,** *107* (18), 4348-4351.

20. Nelson, B. A.; King, W. P., Temperature calibration of heated silicon atomic force microscope cantilevers. *Sensors and Actuators a-Physical* **2007,** *140* (1), 51-59.

21. Schmidt, R. H.; Haugstad, G.; Gladfelter, W. L., Scan-induced patterning and the glass transition in polymer films: Temperature and rate dependence of plastic deformation at the nanometer length scale. *Langmuir* **2003,** *19* (24), 10390-10398.

22. Lantz, M. A.; Gotsmann, B.; Durig, U. T.; Vettiger, P.; Nakayama, Y.; Shimizu, T.; Tokumoto, H., Carbon nanotube tips for thermomechanical data storage. *Applied Physics Letters* **2003,** *83* (6), 1266-1268.

23. King, W. P.; Goodson, K. E., Thermomechanical formation of nanoscale polymer indents with a heated silicon tip. *Journal of Heat Transfer-Transactions of the Asme* **2007,** *129* (11), 1600-1604.

CHAPTER 7

CONCLUSIONS AND RECOMMENDATIONS

7.1 Conclusions

The general goals of the work have been to: (1) develop novel methods for producing electrically interesting carbon-based thin film materials and (2) develop novel methods for direct thermal tip-based fabrication of nanostructures for electronic and photonic devices. First, a process was developed in which a novel macromolecular surfactant dicholesteryl dithienothiophene (ChDTT) was used to accomplish graphene exfoliation and dispersion in organic solvents from graphitic starting materials. While these methods produce relatively large size graphene flakes that have excellent electrical properties, the still relatively low concentration of these solutions combined with no strong affinity for the graphene flakes with typical substrate surfaces (i.e. silicon oxide or other insulator films on silicon or other inorganic supports) leads to difficulty in producing continuous thin films from such materials that might be interesting as transparent conductors or for other electrical applications. The use of non-polymeric surfactants such as ChDTT also offers a convenient route to large-area pieces graphene which may be further manipulated mechanically or through lithographic techniques. An important issue, obviously, is mechanical handling. The use of ultrasonication provides a means to create suspensions which can be coated onto surfaces. However, methods to directly move large pieces of graphene onto other surfaces without such mechanical disruption are obviously desirable. Such techniques are under investigation.

Second, the vapor-phase silanization of APTES was demonstrated. Although it is well known that gas-phase silanization has multiple advantages which a liquid-phase reaction cannot compete with, including the promotion of covalent bonding and removal

of surface water with elevated temperatures, not to mention that gas-phase silanization is solvent-free. However, the exact reaction condition and product performance for gas-phase silanization are still not clear. We also examined the electrostatic force of vapor-silanized APTES layers by performing the immobilization of GO and AuNPs. With an optimized condition, a continuous GO thin film can be deposited on the APTES layer in 10 minutes through the self-assembly of the GO flakes. Similarly, highly dense AuNPs arrays can also be immobilized in the form of multilayer stacking. In addition, patterned GO thin film was generated through the vapor-silanization of APTES, the self-assembly of GO flakes, and the lift-off. These results are not accessible when using liquid-phase silanization.

For the fabrication of graphene oxide devices, we have demonstrated a modified lift-off process by the aid of APTES vapor-silanization for building up either a thin rGO sensor or a thick rGO electrode. For the sensing application, OFETs results proved that we can control the GO deposition down to one to three layers by the differentiation of semiconducting and semi-metallic transfer characteristics. The thinnest, fully covered surface by self-assembly of GO flakes was demonstrated. In addition, this is the first time that n-doping from APTES was presented in transfer characteristics. For the organic electrode application, we found that a 10-minute rest prior to spin-coating can effectively increase the GO thickness. We also showed that a 35 nm rGO film deposited by single spin can function well in an organic semiconductor measurement. The combination of the vapor-silanization and GO self-assembly techniques improves the performances in rGO sensing applications and simplifies the process in rGO electrodes fabrication.

For the project of selective self-assembly of AuNPs, the use of patterned SAMs to guide the assembly of gold nanoparticles has been successfully achieved. This approach provides a high throughput, low cost, and high resolution lithographic method in the applications of metal patterning or catalyst nanoparticles positioning.

7.2 Recommendations for Future Works

For the exfoliation of graphene sheets by electron donor surfactant (chapter two), our powerful macromolecular surfactant, ChDTT, shows superior capability in exfoliating graphene sheets up to tens of microns in size. In addition, the great dispersion ability can stabilize the solution for months, but the intrinsic problem for the pristine graphene flakes dispersion is that the concentration is still too low for further application. In addition, without the aid of a surface charge, there is no controllable deposition method for the flakes. Conversely, GO flakes have a good filming capability, either by self-assembly through charge attraction or by spin-coating through concentrated solution. However, it is well known that GO can never regain its electronic properties back to the level of pristine graphene. Therefore, it will be a great breakthrough if the pristine graphene flakes can be charged without interfering with its SP2 structure. Differing from the typical graphene modification methods in the literature, which attach side chains on the basel plane or the edge of the flake through covalent bonding, ChDTT molecules serve as an electron donor and are adsorbed on the graphene surface through $\pi-\pi$ stacking. In this way, no defect sites, which are opened by SP2 interruption, will be generated. If the two cholesteryl groups can be modified by some functional moieties which are negatively charged in the solution, such as the carboxylic group, the pristine graphene flakes will tend to be dispersed and stabilized like graphene oxide. The beauty is that they will not lose their electronic performances. More synthetic and chemical efforts should be addressed concerning the ChDTT compound. Afterwards, a series of work involving expandable graphite exfoliation, graphene flakes dispersion, graphene thin film deposition, and OFETs measurement can be done, and each of these is a valuable research topic.

Actually, the work of graphene nanoribbon synthesis (chapter three) is still in progress. We saw very promising results in polyanthracene graphitization, which proved our low energy barrier theory, and the next step is to pursue cyclodehydrogenation inside

the polymer chain, which can further lower the pyrolysis temperature needed. There are two possible routes for this aim. First, controlling and limiting the electro polymerization of anthrcene to a surface reaction level will be a good approach. It has been proven by Mullen's work that the gold surface guides the orientation of anthracene units and assists in the consolidation. So, a subtle and precise control of electro polymerization should be studied, and we should replace the thick bulky film. Second, more interestingly, an alternative energy source should be able to oxidize the polyanthracene and process the dehydrogenation. Figure 7-1 shows the electron injection mass spec (EI MS) of bianthracene taken by Dr. Janusz Kowalik. Before electron bombardment, only pure bianthracene (MW=354.14) can be observed. While the electrons increase, a dehydrogenated product appears, including bianthrcene (MW=350.11). This is solid evidence for the electron oxidation of polyanthracene. The energy level should be studied first, and the identification in the Raman spectrum for verifying graphene nanoribbon should be clarified as well. By this approach, polyanthracene could be consolidated and patterned concurrently by e-beam lithography.

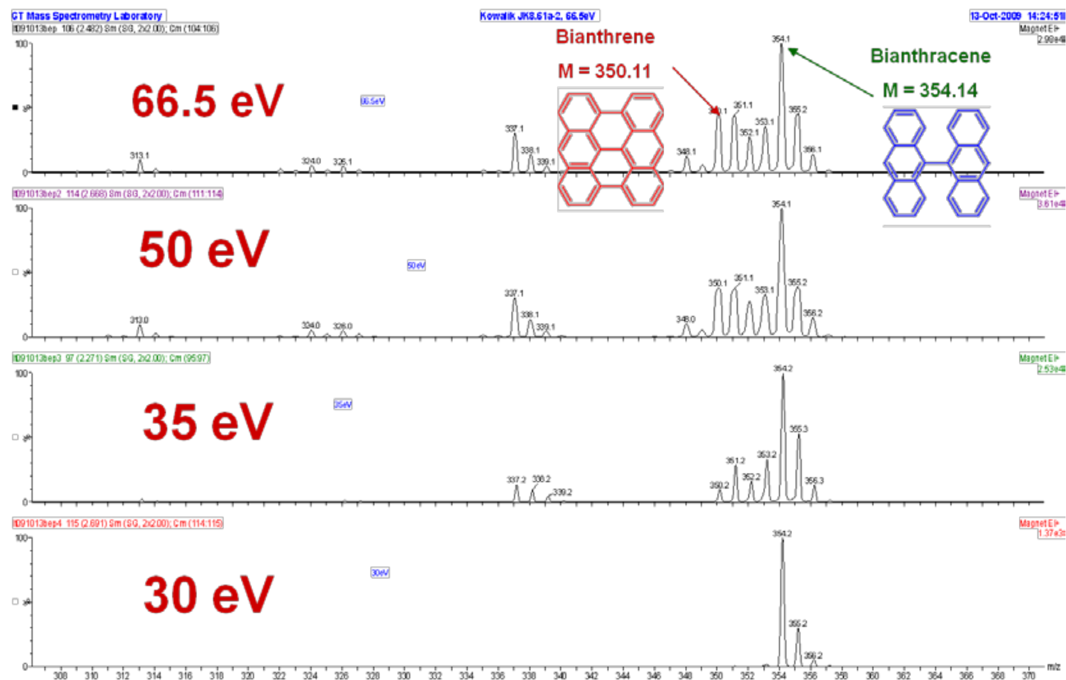

Figure 7-1: Electron injection mass spec (EI MS) of bianthracene.

For the APTES vapor-silanization (chapter four), future work should address the studies of the silanization mechanism. It is well known that both the reduction of the surface water and the promotion of the silanization rate contribute to the improvement of aminosilane quality in high temperature vapor-silanization. However, which item has a great effect is always a debate. Using our hot stage type vacuum reactor, a simple control experiment can be conducted to thoroughly exclude the surface water. The sample could be heated at a higher temperature, e.g. 300° C, under the vacuum to thoroughly eliminate the surface water before passing the silane vapor. Due to the fast cooling rate of the hot stage sample holder, the sample can be cooled under the high vacuum to the desired silanization temperature quickly and then the reaction can be started. In this way, the factor of the surface water can be totally removed and the sole temperature effect can be verified.

For the reduced graphene oxide device, there are two interesting topics worthy to study. First, conducting thermal reduction in a carbon-rich environment might help to further fix the defect sites in the GO flakes. It's known that the electronic performance of GO is restricted to its SP2 vacancy no matter how many oxygen atoms are removed. The CVD type reaction might help to fill the carbon vacancy from the reaction with gas-phase carbon source, e.g. methane, to recover more electronic properties. Second, the n-doping effect in our device was first found to be generated by underlayer aminosilane. Future work should be focused on the influence of the n-doping level caused by the amine content. On the other hand, silanes with various electron donating or accepting functional groups, e.g. fluorinated silane, could be used to control the n-doping or p-doping of the rGO ultra-thin film.